Polarization-diverse absorption enhancement in thin-film organic photovoltaic devices using long-pitch plasmonic gratings

by

Yifen Liu

A dissertation submitted to the graduate faculty

in partial fulfillment of the requirements for the degree of

DOCTOR OF PHILOSOPHY

Major: Electrical Engineering

Program of Study Committee:
Jaeyoun Kim, Major Professor
Rana Biswas
Sumit Chaudhary
Vikram Dalal
Jiming Song

Iowa State University

Ames, Iowa

2012

To my parents

Huiping Liu and *Ying Zhang*

ACKNOWLEDGEMENTS

The completion of this thesis would not have been possible without the help from a number of people. First of all, I would like to thank my advisor Professor Jaeyoun Kim for his insightful suggestions and guidance through my research. The journey toward the completion of the Ph. D. program would have been a lot more difficult without the encouragement from Professor Jaeyoun Kim and Professor Vikram Dalal. Professor Ruth Shinar's support and help on the organic solar cell device fabrication are appreciated. I want to thank my committee members Professor Rana Biswas, Professor Sumit Chaudhary, Professor Vikram Dalal and Professor Jiming Song, for always taking the time to have discussion with me to clear up my confusions. Discussions with Dr. Joseph Shinar were of great help for me as well.

I am sincerely grateful for all the trainings and help from Max Noack, Wai Leung, Robert Mayer, Teng Xiao, Weipan Cui and Joong-Mok Park. Wai Leung's training on electron beam lithography led me into the fascinating world of nanofabrication. Max Noack's serious attitude toward experimental research and equipment maintenance has been inspiring. I appreciate that Max helps to keep essential experimental equipment running in good condition. I learned a lot from Robert Mayer who is always willing to help. His knowledge and skills have been great resources for me. The research on organic photovoltaic devices will be much more time consuming without the valuable training from Teng Xiao and Weipan Cui and my discussions with them. I want to thank Dr. Joong-Mok Park for his help on laser interference lithography and Dr. James Anderegg for his time and kind help with XPS measurements.

The Ph. D. program is more of a self-recognition journey for me rather than purely scientific research. I thank all the tough times I had in these years, which made me a stronger and better person, and more importantly, made me willing to surpass self-imposed limits. Professor Jaeyoun Kim's persistence will encourage me even after my graduation. Professor Vikram Dalal's passion for research has enlightened me to pursue for passion and joy in work and life. I appreciate Professor Mark Gleason's time and suggestions on the mentorship relationship and public speaking. Professor Ruth Shinar and Keqin Han have been very nice sharing their experience with me and giving me suggestions on life.

A friendly and productive working environment is vital for any research program. Jiwon Lee is such a good friend and group mate. Teng Xiao, Weipan Cui, Randy Gebhardt, Mehran Samiee Esfahani, Nayan Chakravarty, Sambit Pattnaik, Shantan Kajjam, and many other students at the Microelectronic Research Center are good friends and coworkers of mine. I thank all my friends for making my life more interesting.

Last but not least, I want to thank my parents Huiping Liu and Ying Zhang for always taking my happiness as the single most important thing. Words cannot express my gratitude for their unconditional love and support. I am grateful for meeting my husband Yu Liu in Iowa State University, who is always capable of cheering me up.

Yifen Liu

Mar 2012

Ames, IA

TABLE OF CONTENTS

LIST OF FIGURES viii

LIST OF TABLES xiii

ABSTRACT xiv

CHAPTER 1. Introduction 1

- 1.1 Solar energy 1
- 1.2 Organization of this thesis 4

CHAPTER 2. Research background 7

- 2.1 Surface plasmon resonances 7
    - 2.1.1 Plasmas and Plasmons 7
    - 2.1.2 Localized SPR 10
    - 2.1.3 Propagating SPR 12
- 2.2 Application of surface plasmons 16
    - 2.2.1 Waveguide-based plasmonic biosensors 16
    - 2.2.2 Nanoscale plasmonic Bragg reflectors 20
- 2.3 Organic solar cells 23
    - 2.3.1 Fundaments of solar cells 23
    - 2.3.2 Organic solar cells 27
- 2.4 Application of SPRs in OPVs 32

2.4.1 L-SPRs in OPVs 33
2.4.2 SPPs in OPVs 35
CHAPTER 3. Numerical simulations of OPVs with metallic gratings 38
3. 1 OPVs with silver gratings 38
3.2 Simulation setup and method 40
3.3 Effect of the grating height on the absorption enhancement 44
3.4 Enhancement of TM absorption 46
3.5 Enhancement of TE absorption 52
3.6 Combining TM and TE absorption enhancements 56
Chapter 4. Experimental methodology 60
4.1 Grating Fabrication 60
4.1.1 Grating Fabrication with EBL 62
4.1.2 Grating Fabrication with laser interference lithography 68
4.2 Reflection measurement with microspectrometer 73
4.2.1 Microspectrometer setup and working principle 74
4.2.2 Reflection measurement 77
Chapter 5. Absorption enhancement in OPVs 82
5.1 Comparisons between simulation and experimental results 82
5.1.1 Characterization of gratings and OPVs 82

        - 5.1.2 Bare grating results comparisons 86
        - 5.1.3 OPV results comparisons 92
    - 5.2 Effect of the grating geometry on the absorption enhancement 95
        - 5.2.1 Effect of the grating height 96
        - 5.2.2 Effect of the grating duty cycle 97
        - 5.2.3 Effect of the grating pitch 104
    - 5.3 Polarization diverse absorption enhancement 107
- Chapter 6. OPV devices 111
    - 6.1 Superstrate type OPVs 113
        - 6.1.1 Superstrate type traditional OPVs 113
        - 6.1.2 Superstrate type inverted OPVs 116
    - 6.2 Substrate type inverted OPVs 118
    - 6.3 Ag nanoparticles in superstrate-type inverted OPVs 124
- Chapter 7. Conclusions and future perspectives 134
- Appendix A. Simulation-predicted absorption increase in OPVs 138
- Appendix B. Comparisons between OPVs with Al and Ag gratings 141
- Bibliography 143

LIST OF FIGURES

Fig. 1.1 Annual installed PV capacity 2

Fig. 2.1 The Lycurgus Cup 8

Fig. 2.2 The origin of localized surface plasmon resonance (L-SPR) 10

Fig. 2.3 The effect of sizes and shapes of nanoparticles on their plasmonic resonance wavlength 11

Fig. 2.4 The bound (SPP), radiative plasmon polariton and quasibound surface plasmon dispersion relations for SiO2/Ag interface.. 13

Fig. 2.5 Common methods to couple light waves to SPPs 15

Fig. 2.6 Waveguide-based excitation of SPPs by f-MIM structure and the dispersion relation of the SPP in f-MIM 18

Fig. 2.7 Sensitivity of f-MIM based biosensors. 19

Fig. 2.8. PBRs with a step profile and a sawtooth pofile 21

Fig. 2.9. Transmission spectra for the step and sawtooth PBRs 23

Fig. 2.10 Schematic of a solar cell 24

Fig. 2.11 The equivalent circuit and a typical IV curve of a solar cell 25

Fig. 2.12 Best research solar cells of different types 27

Fig. 2.13 The structure and absorption coefficients of P3HT and PCBM 29

Fig. 2.14 The schematic view of OPV 30

Fig. 2.15 Phase separation of donor and acceptor in a bulk heterojunction OPV 31

Fig. 2.16 Schematic structure of the PV device with Au nanoparticle and the external quantum efficiency curves 34

Fig. 2.17 Utilization of plasmonic nanostructures in PVs 36

Fig. 3.1 Schematic diagrams of the model OPV device structures. 38

Fig. 3.2 Major structural parameters in the OPV design. 39

Fig. 3.3 COMSOL simulation setup for OPVs. 41

Fig. 3.4 Light absorption enhancement schemes from (a) SPP excitation for TM and (b) waveguide mode coupling for TE 43

Fig. 3.5 Effect of the grating height on EF in Jsc 45

Fig. 3.6 EFTM as a function of the grating duty-cycle D and the grating pitch Λ. 47

Fig. 3.7 Comparisons between absorption spectra of different OPVs 48

Fig. 3.8 Normalized field patterns at different plasmonic absorption peaks...................... 49

Fig. 3.9 The absorption spectrum for Λ = 1040 nm as a function of D.. 50

Fig. 3.10 EFTE as a function of D and Λ 53

Fig. 3.11 Schematic diagram for the grating-based guided mode excitation. 55

Fig. 3.12 Absorption enhancement regions for TM, TE and unpolarized light................. 57

Fig. 4.1 Different pattern definitions in (a) a positive and (b) a negative photoresist 61

Fig. 4.2 A picture of the EBL system (eLiNE from Raith GmbH)................................... 62

Fig. 4.3 Plasmonic Ag structures fabricated by e-beam lithography. 63

Fig. 4.4 SEM images of Ag gratings with the same pitch size of 1040 nm and different duty cycles. 67

Fig. 4.5 The Lloyd mirror setup for interference lithography 69

Fig. 4.6 SEM images of 1D and 2D gratings. 72

Fig. 4.7 Cross section SEM images 1D gratings. 72

Fig. 4.8 Schematic diagrams of the micro-spectrometer... 74

Fig. 4.9 Working principle of micro-spectromter... 76

Fig. 4.10 Reflection measurement from microspectrometer 78

Fig. 4.11 Microspectrometer test - effect of the objective lens. 79

Fig. 4.12 Microspectrometer test – effect of the sample position 81

Fig. 4.13 Increase of absorption in OPVs measured from different ROI sizes 81

Fig. 5.1 Cross section SEM images of a bare Ag grating and a OPV showing the conformal OPV structure on the grating 83

Fig. 5.2 Cross section SEM images of a bare Ag grating and a OPV on the Ag grating to show the Ag grains and thickness ratios. 84

Fig. 5.3 AFM images and depth profiles of a bare Ag grating and a OPV 86

Fig. 5.4 Comparisongs between experimental and simulations results – increase in absrotpion in bare Ag gratings with different duty cycles 88

Fig. 5.5 Comparisongs between experimental and simulations results – TM waves, increase in absrotpion in Ag gratings of different pitches 90

Fig. 5.6 Comparisongs between experimental and simulations results – TE waves, increase in absrotpion in Ag gratings of diffeerent pitches................................ 91

Fig. 5.7 Comparisons between experimental and simulation results – increase in asbsorption in OPVs with grating of different duty cycles 93

Fig. 5.8 Comparisons between experimental and simulation results – increase in asbsorption in OPVs with grating of different pitches....................................... 95

Fig. 5.9 Effect of the grating height on the absorption enhancement. 96

Fig. 5.10 Effect of the grating duty cycle on the absorption enhancement when the grating height is 25 nm 97

Fig. 5.11 The effect of the grating duty cycle on the light absorption enhancement – Substrate #1 98

Fig. 5.12 The effect of the grating duty cycle on the light absorption enhancement Substrate #2 100

Fig. 5.13 SEM images Substrate #1 and #2 showing fifferent Ag grains sizes 102

Fig. 5.14 The absorption enhancement's tolerance for the grating duty cycle 103

Fig. 5.15 The effect of the grating pitch on light absorption enhancment when the grating duty cycle is fixed at 36% 105

Fig. 5.16 The effect of the grating pitch on light absorption enhancment when the grating duty cycle is fixed at 45% 106

Fig. 5.17 The effect of the polarization angle on the absorption enhancement for the grating design of pitch 1040 nm, duty cycle 36% 108

Fig. 5.18 The effect of the polarization angle on the absorption enhancement for the grating design of pitch 1040 nm, duty cycle 45% 109

Fig. 6.1 Schematically illustration of the substrate and superstrate type, traditional and ivnerted solar cells 112

Fig. 6.2 Superstrate type traditional OPV and its band diagram 113

Fig. 6.3 Comparisons of $J\ V$ curves of traditional OPVs 115

Fig. 6.4 Superstrate type inverted OPV and its band diagram 116

Fig. 6.5 Schematic view of the substrate type inverted OPV with a Ag grating as the back reflector and light trapping scheme, together with the band diagram 119

Fig. 6.6 Best substrate type inverted OPV on a planar Ag coated glass substrate 119

Fig. 6.7 EQE curves of both superstrate and substrate type inverted OPVs. 121

Fig. 6.8 Two types of devices for testing the problems of the substrate type device 122

Fig. 6.9 The OPV characteristics of three devices with different concentration of Ag particles on the ITO/glass surface.. 125

Fig. 6.10 JV curves of devices with and without Ag particles under different times of light illumination 127

Fig. 6.11 OPV with Ag particles on ITO showed higher carrier extraction 129

Fig. 6.12 Higher EQE and EQE ratios when Ag particles are added into inverted OPVs, indicate better carrier collection efficiency 130

Fig. 6.13 SEM images of Cs_2CO_3 and P3HT:PCBM films, the morphologies are different for samples with and without Ag particles underneath 132

Fig. A.1 For TM waves (a) the absorption increase in the whole OPV structure and the P3HT:PCBM polymer film; (b) the effectiveness ratio of the increase in absorption 1329

Fig. A.2 For TE waves (a) the absorption increase in the whole OPV structure and the P3HT:PCBM polymer film; (b) the effectiveness ratio 140

Fig. B.1 Absorption in the whole OPV structure and in the P3HT:PCBM film only for OPVs with Ag and Al gratings, respectively. 141

LIST OF TABLES

Table 3.1 The changes in EF due to ±5% deviations in the OPV layer thickness and the real part of its refractive index. 58

Table 4.1 Comparisons between EBL and inteferometric lithography 62

Table 4.2 The effect of electron dose on the grating geometries....................................... 66

Table 4.3 The accuracy of duty cycles for different grating geometries 68

Table 4.4 Dependence of the grating pitch on the mirror angle 71

Table 4.5 Selective grating geometries made from laser interference lithography 73

Table 6.1 Device characteristics of traditional OPVs with different annealing conditions 115

Table 6.2 Device characteristics of several superstrate-type inverted OPVs 117

Table 6.3 Substrate-type inverted OPVs 121

Table 6.4 Semitransparent OPVs for testing the sputtered ITO electrode 123

Table 6.5. OPVs for testing the Ag electrode 123

Table 6.6 OPVs with a thick P3HT:PCBM layer, the effect of Ag particles on ITO coated glass 128

Table 6.7 OPVs with a thin P3HT:PCBM layer, the effect of Ag particles on JV characteristics and carrier collection... 129

ABSTRACT

Organic photovoltaic (OPV) devices, which convert solar energy into electricity using organic semi-conductive polymers or small molecules, have shown great promise in renewable and green energy applications. Despite their flexibility, lightweight and low-cost, OPVs suffer from low power conversion efficiency (PCE). Recent progresses in the synthesis of new polymers and tandem solar cells promoted the PCE to 10.6%, as reported in Feb 2012, which is a great leap from the 2.5% reported in Feb 2001. In thin film solar cells including OPVs, however, the light absorption is intrinsically limited by the thinness of the photoactive layer, especially at wavelengths near the edge of their absorption band. Surface plasmon polaritons (SPPs), a hybrid of electron density oscillations and optical waves at dielectric/metal interfaces, have great potential in overcoming the limit in light absorption for three reasons. (1) SPPs are highly evanescent. When generated at the photoactive layer/metal electrode interface, SPPs benefit the optical absorption in thin-film solar cells by concentrating optical waves and their electromagnetic energy near the photoactive layer. (2) SPPs propagate along the supporting interface, which can be utilized to change the light path. As the light propagates sideways along the photoactive layer, the light path and thus the absorption are effectively increased. (3) SPPs have unique and tunable dispersion relations, *i.e.* their propagating speed and effective index can be controlled. This can be useful in engineering and combining the SPPs with other photonic phenomena for the absorption enhancement.

In this thesis, I proposed to use silver (Ag) gratings to enhance the light absorption in P3HT:PCBM-based OPVs. To implement the Ag gratings in OPVs, I designed an substrate type inverted OPV architecture with light impinging on the device directly from the air side, in contrast to the traditional superstrate type OPVs with light impinging on the transparent substrate first and then the device.

I showed, through finite element method (FEM) simulations, that with proper design of the grating geometry, we can achieve light absorption enhancement for linearly polarized light with all polarization angles, despite the fact that the Ag gratings are periodic only in one direction. The generation of propagating SPPs and the waveguide modes in the photoactive layer, are revealed as the two absorption enhancement mechanisms. Ag gratings are fabricated with electron beam lithography (EBL) combined with a lift-off process. The gratings and the OPVs with grating substrates were characterized with a micro-spectrometer, which showed more than 200% enhanced absorption at ~ 690 nm with the optimized grating design. The impacts of the grating pitch size, duty cycle and the height on the absorption enhancement were also studied with numerical analysis and experimental confirmation.

In addition, this thesis also discusses the OPV device performance and the future prospective of plasmonics-assisted thin film solar cells.

CHAPTER 1. Introduction

1.1 Solar energy

Fossil fuels, such as coal, oil and natural gas, are the main energy sources from the start of human civilization. It takes millions of years for the remains of plants or animals to turn into fossil fuels, which makes fossil energy sources non-renewable. For example, the current estimations of the worldwide peak production of oil are around or before the middle of the 21st century. After the peak production, it will be more difficult to extract the oil and its price will be accordingly higher. As a result, renewable energy resources have gained great interest and increasing application over the past years. The limited supply of fossil energy sources and the increasing demand impose the need for renewable energy sources. Solar cells, or photovoltaics (PVs), which convert sun light into electricity, have attracted much attention as a promising candidate for environmentally clean and renewable energy source. From the enormous energy supply of the Sun, Earth's surface receives about 1.2×10^5 TW of solar power on average, while the annual world energy consumption is less than 20 TW [1]. The annual installed PV capacity in the top eight countries in Fig. 1.1 [2, 3] clearly shows the rapidly increasing utilization of solar energy.

However, for wider application of solar cells, several technical problems need to be solved. One problem is the intermittent nature of the solar radiation, available only during the day and strongly reduced in overcast skies [4]. Cheap energy storage or better developed and managed electric grids are necessary to allow a higher percentage of the total electric production to be intermittent. Another issue is that photovoltaics must produce much more energy than was required to produce the PV system [4]. The years that the PV system must operate to produce the same amount of energy required for its production is called the "energy payback". The energy produced is new energy only after the payback time.

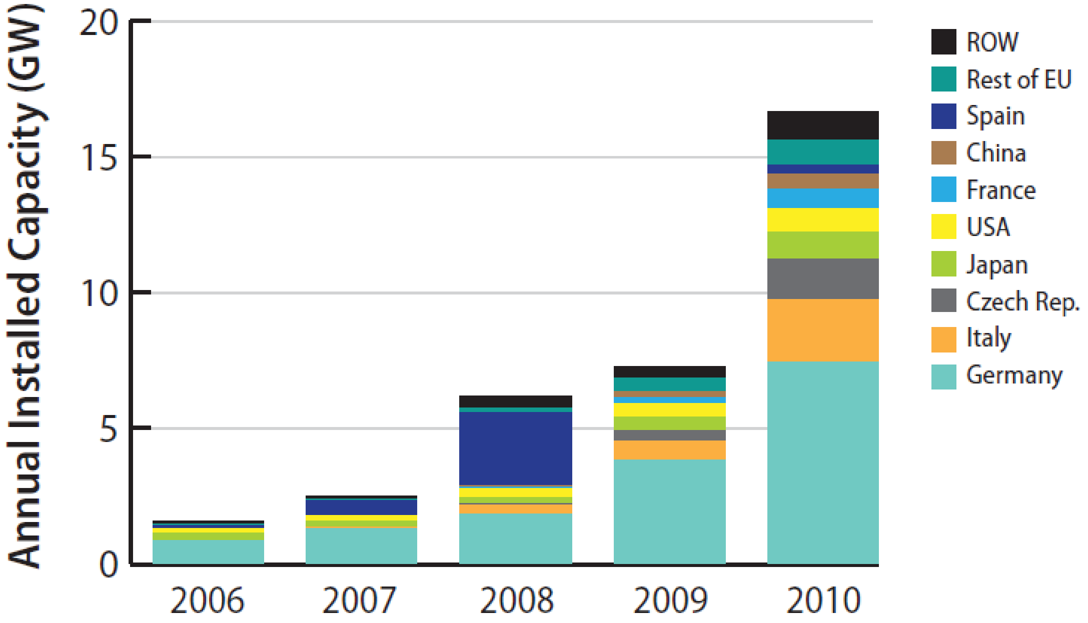

Fig. 1.1 Annual installed PV capacity in the top eight countries. (from [3], whose data is from [2])

To achieve shorter energy payback time, lower material and fabrication cost, higher power conversion efficiency (PCE) and longer lifetime are the keys.

The present cost of photovoltaic panels, which is around \$0.16–\$0.38 per kWh, is affordable for certain markets but it is still too high to actually compete with conventional electricity with a typical average price of only \$0.05 per kWh [2-4]. Most of the solar cell market at present is based on crystalline silicon wafers with thickness between 180 ~ 300 μm, with 65% of the cost is for the Si wafers [4, 5]. Thin-film PVs based on amorphous or organic materials attract an increasing level of interest as a low-cost alternative to crystalline Si devices. For example, with polycrystalline Si, the active layer thickness can be in the range of 1 ~ 2 μm; for thin-film solar cells based on organic materials, the active layer thickness can be as thin as ~ 100 nm. The fabrication cost will be greatly reduced with mass production. Public subsidy to photovoltaic R&D and to installation will be necessary to stimulate production and thereby reduce costs [4].

In thin film PVs, there is an intrinsic conflict in choosing the thickness of the photoactive layer. The thin PV layer limits PCE by providing insufficient absorption length, especially for wavelengths near the edges of the absorption band, it is not advised to make the layer thicker due to the accompanying degradation in the carrier collection efficiency [5]. As a solution, the use of the in-plane waves, which propagate in the horizontal direction while being confined within the PV layer, was proposed to enhance the absorption without increasing the PV layer thickness [5-10].

Surface plasmon polaritons (SPPs) are surface waves propagating along metal/dielectric interfaces and can be used as in-plane waves to effectively increase the light path and thus the absorption. SPPs are generated due to the plasmonic resonant interaction between light waves and the free electrons in metal. Plasmonics has attracted much research interest in the study of nanoscale light-matter interaction, such as subwavelength scale light confinement and manipulation [11, 12], surface enhanced Raman scattering (SERS) [13, 14]. Surface plasmon resonanc (SPR) modes are highly confined near the metal/dielectric interface with penetration depth of hundreds of nanometers inside the dielectric layer, which is well-matched to the active layer thicknesses in thin-film solar cells. The study of plasmonic effects in thin film PVs has gained much interest recently [5, 6, 8, 15, 16].

1.2 Organization of this thesis

In this thesis, I proposed to use silver gratings to enhance the optical absorption of P3HT:PCBM (poly(3-hexylthiophene):[6,6]-phenyl-C_{60}-butyric acid methyl ester)-based organic photovoltaic (OPV) devices. The grating is implemented on the back of the device, which acts as a reflector and electrode. The main part of this thesis is the numerical design and experimental verification of plasmonic grating on the back of the OPV for polarization diverse light absorption enhancement near the edge of P3HT:PCBM absorption band.

Chapter 2 provides the background of solar cells and SPR. Firstly, two types of SPR modes and their unique properties are discussed: the localized SPR and the propagating SPR (*i.e.* the SPP). To demonstrate the applications of SPPs, I briefly present my previous works based on my two papers on waveguide-based plasmonic sensors and nanoscale plasmonic Bragg reflector, respectively. Then the working principle of solar cells, OPVs and the characteristic parameters for solar cell performance evaluation are discussed. This chapter also covers the literature study on two common approaches to utilize plasmonic effects in OPVs with metallic nanoparticles and periodic nanostructures as the SPR launching schemes, respectively.

In Chapter 3, I numerically investigated the impact of long-pitch (> 800 nm) metallic gratings on the absorption enhancement in OPVs. The impact of the grating's geometric parameters on the absorption enhancement is studied, including the grating height, pitch and duty cycle. I found that gratings with such a long pitch can simultaneously enhance the absorption of TM (with the electric field perpendicular to the grating ridges) and TE (with the electric field parallel to the grating ridges) waves by inducing lateral Fabry-Perot resonances of surface plasmon-polaritons and waveguide modes at the same time. The grating duty-cycle turned out to be the most important factor in realizing the two enhancement effects in the same spectral regime.

Chapter 4 covers the methodology of grating fabrication, including electron beam lithography (EBL) or UV laser inteferometric lithography combined with a lift-off process. Different gratings with an area of 800 μm × 800 μm are made and OPVs are made on them. A micro-spectromter is used to measure the reflection from gratings as well as OPVs. The working principle of the micro-scale optical measurement and the data processing are discussed in this chapter. Furthermore, I measured the same sample with different settings of the microspectrometer. The great agreement between the results confirmed the sanity of the reflection measurement.

In Chapter 5, the reflection is measured for OPVs with different gratings on the back and the absorption enhancement is deduced from the decrease in reflection. The experimental and simulation results are in good agreement for both the bare gratings and the OPVs with gratings. Again, the effect of grating height, pitch and duty cycle are studied and the optimized grating design showed 200% enhanced absorption at ~ 690 nm. It is verified that the light absorption enhancement is not dependent on the polarization of the incident light. I also showed that the absorption enhancement in TM modes is more tolerant to the non-perfect grating geometries while the excitation of waveguide modes in TE modes is very sensitive to them.

Chapter 6 discusses the OPV fabrication and the device performance. The traditional and (electrodes) inverted superstrate type OPVs are investigated. For the proposed substrate type inverted OPVs with silver grating back reflectors, I described the effort to make OPVs with the plasmonic effects incorporated and the performance and technical issues of the devices. Potential performance enhancement of inverted OPVs with silver particles is also discussed even without any light absorption enhancement.

Chapter 7 concludes this thesis and covers the future perspectives of plasmonics-assisted thin film solar cells.

CHAPTER 2. Research background

2.1 Surface plasmon resonances

2.1.1 Plasmas and Plasmons

Plasmons are the resonant interaction between light waves and plasma consisting of free electrons. Plasmonics has attracted much research interest because it offers the possibility to control light and matter interaction on the subwavelength scale, which overcomes the diffraction limit in traditional optics and enables nanophotonic technologies in diverse application areas.

One of the most famous and ancient example of plasmonic effect is the Lycurgus Cup shown in Fig. 2.1, which was made in the 4th century AD in late Roman Empire period and now in British Museum in London. While depicting the triumph of Dionysos over Lycurgus, the dichroic glass cup appears opaque green when viewed with light reflected from the surface of the cup (Fig. 2.1(a)). When light shines through the cup, it turns a translucent red. This unusual optical property is due to the tiny amount of gold and silver colloids in the cup with sizes of about 70 nm in diameter [17]. These particles interact with incident light waves in a resonant way, *i.e.* plasmonic resonance, resulting in strong reflection of the green portion of the visible light while the transmission of the red portion is not affected.

Research on plasmons started at the turn of the 20th century with Gustav Mie's study in 1908 on light scattering from metal spheres as the pioneering work [18]. It also explained the dichroic properties of the Lycurgus Cup. After Ritchie's work [19] on electrons at the surface of metallic films, Otto [20] as well as Kretschmann and Raether

[21] demonstrated methods to couple free space light into surface plasmons on metallic films. These surface plasmon generation schemes, named after Otto, Kretschmann and Raether, are still widely used. Since then, unique properties of surface plasmons have been studied, leading to the emerging of the field of plasmonics [12, 17, 22, 23]. The research has found applications in various areas such as plasmon-assisted sensors [24], solar cells [5, 6, 25] and the subwavelength-scale control over light with plasmonics, overcoming the diffraction limit [11, 12].

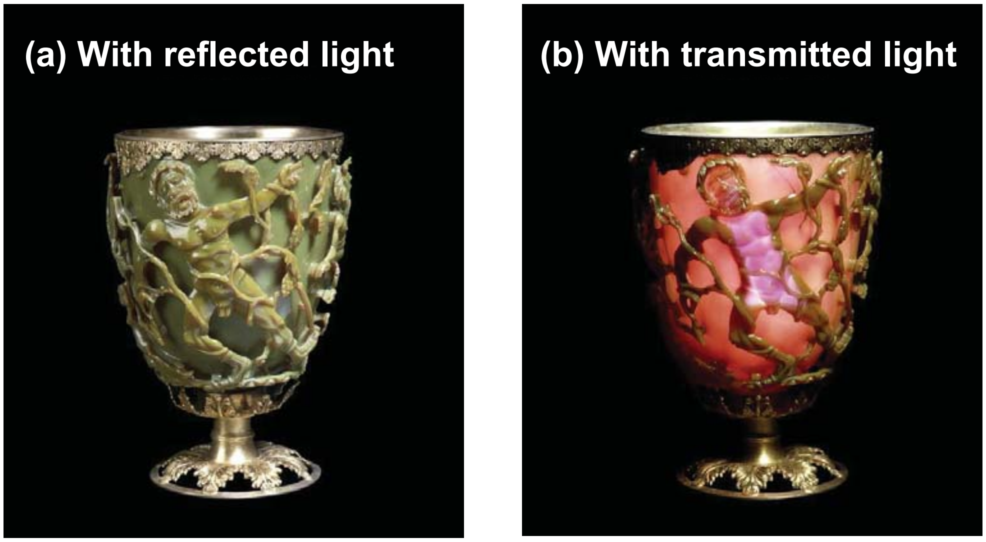

Fig. 2.1 The Lycurgus Cup showing (a) opaque green viewed with reflected light and (b) glowing translucent red viewed with transmitted light. (Pictures from online resources of the British Muesum)

For bulk plasmas, the plasma frequency ω_p is given by [23, 26]

$$\omega_p = \sqrt{ne^2/(\varepsilon_0 m)} \tag{2.1}$$

where ε_0 is the permittivity of free space, n is the density of the free charges, e and m the charge and mass of an electron. For example, the plasma frequency for silver (Ag) is 9.1 eV [22], which corresponds to 136 nm.

If the energy dissipation during light-plasma interaction is taken into consideration, the complex relative permittivity can be described by Drude model [27]:

$$\varepsilon(\omega) = 1 - \frac{\omega_p^2}{\omega(\omega + i/\tau)} \tag{2.2}$$

where $\varepsilon(\omega)$ is the frequency dependent relative permittivity, τ is the relaxation time, *i.e.* the mean free interval between ionic collisions.

Bulk plasmons cannot be excited by light because of the longitudinal nature of the oscillating charges about positive ion cores within the bulk of the plasmon and the transverse nature of the electric field of light [23]. However, structuring the metal changes the nature of the plasmonic response of the metal and can allow light to couple to the associated plasmon modes [23], *i.e.* surface plasmon resonances.

Surface plasmon resonance (SPR) is a resonantly coupled state of electron density oscillations and optical waves. Depending on the metallic structure supporting the SPR, it can take two different forms: the delocalized or propagating SPRs (P-SPRs) which are more commonly known as surface plasmon-polaritons (SPPs) and the localized SPRs (L-SPRs). SPPs or P-SPRs are supported by metal films as surface waves propagating along its interface with a dielectric material. The L-SPRs occur on nanoparticles with dimensions much less than the light wavelength and can be supported by a wide variety of particle geometries [23]. Gold (Au) and silver (Ag) particles are good examples of L-SPRs as illustrated in Fig. 2.1. Metallic particles of different shapes such as prisms, rods and ellipsoids showed very different SPR properties [22, 28]. The interaction between different particles or particle-pairs has great impact on the generation and characteristics of L-SPRs too [22, 28].

2.1.2 Localized SPR

The origin of the L-SPR generation is illustrated in Fig. 2.2. When light waves incident on metallic particles with sizes much smaller than the wavelength of the incident light, the oscillating electric filed causes the free electron clouds to oscillate, forming the SPR modes. The associated electromagnetic fields near the nanoparticles are confined to volumes much smaller than a cubic wavelength [23] and can be much stronger than the fields of the incident light. This light wave confinement and energy concentration is the key motivation for research on particle-based plasmonic resonances. An example of its successful application is the surface enhanced Raman scattering (SERS) for chemical and biomedical spectroscopy [13, 14].

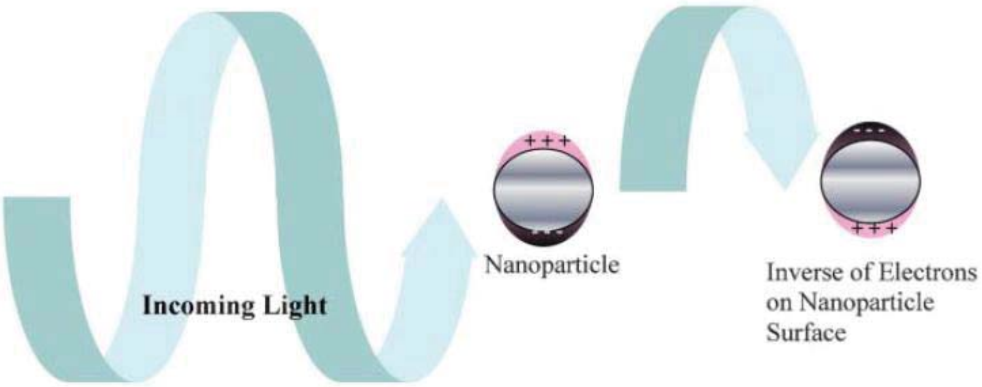

Fig. 2.2 The origin of localized surface plasmon resonance (L-SPR) due to the interaction between the electric fields of the incident light and the free moving electrons in metallic particles. (from Ref. [28])

The localized SPR is very dependent on the material, size and shape of the particles. Commercially available gold and silver nanospheres in aqueous suspension exhibit different colors in the visible spectral region depending on the material and the shape. Furthermore, by adjusting the particle shape, the localized surface plasmon resonant frequency can be tuned from the ultraviolet, throughout the visible, and into the infrared regions of the electromagnetic spectrum [23].

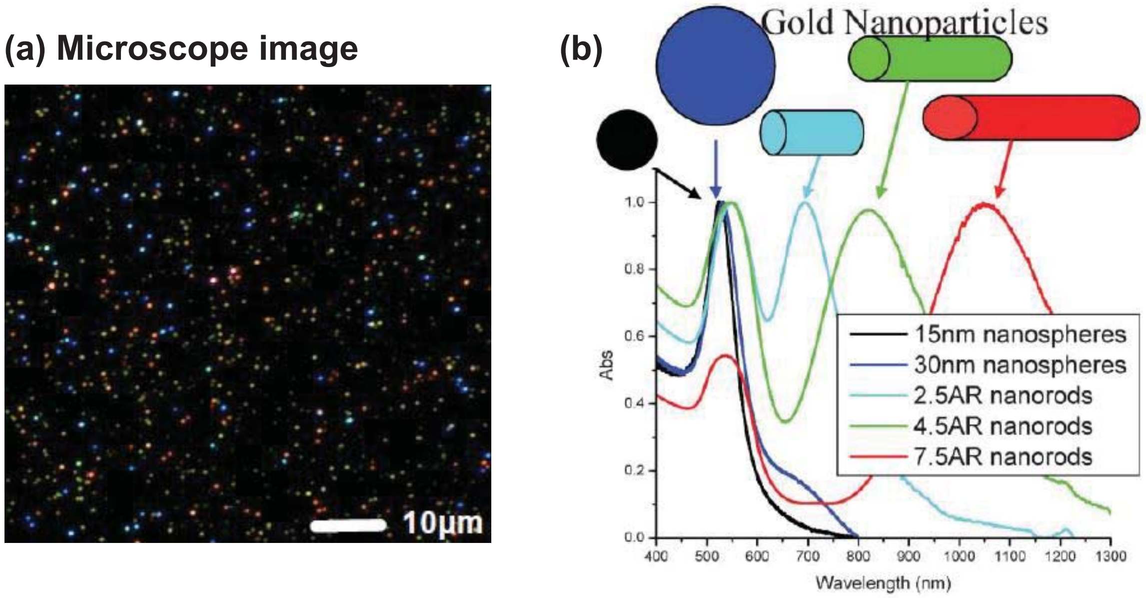

Fig. 2.3 (a) A true color, dark-field photograph of silver and gold nanoparticles of different sizes and shapes. Different colors suggest different resonance frequencies of the nanoparticles (from Ref. [22]). (b) When anisotropy is added to the gold nanoparticle, the growth of nanorods with higher aspect ratio (AR) in this case, the optical properties of the nanoparticles change more dramatically than those from the size change of the nanoparticles (from Ref. [28]).

Figure 2.3(a) exhibits the light scattering effects from gold and silver nanoparticles. With the incident light illumination blocked through dark-field microscopy, the true color photograph collects only the light scattering information at the plasmon resonance. With every dot representing one nanoparticle, the color under microscope strongly depends on the shape (nanospheres or nanorods) and composition (silver or gold) of the particles. The corresponding colors are blue for silver nanospheres, green and yellow for gold nanospheres, orange and red for gold nanorods [22]. Fig. 2.3(b) further demonstrates that the anisotropy in gold nanoparticles is more influential in tuning the resonance frequency when compared with the change in the nanoparticle sizes [28]. By changing the aspect ratio (AR) of the naonorods from 2.5 to 7.5, one plasmonic resonance mode changes from 700 nm to 1050 nm, while the plasmonic mode near 550 nm is not affected much.

2.1.3 Propagating SPR

The propagating SPRs (P-SPRs) are known as surface plasmon-polaritons (SPPs), which are surface waves propagating along the interface between a dielectric material and a metal layer. SPPs are electromagnetic fields bound to the metal/dielectric interfaces due to the interaction between the electric fields and the electrons near the surface of the metal, which is shown in the inset of Fig. 2.4. The SPPs have evanescent field in both the dielectric and the metal layers, which means the field intensity decreases exponentially along the direction normal to the interface. The penetration depths along the normal direction, taken as $1/e$ of the power at the surface, are about 100 ~ 400nm depending on the dielectric index and ~ 20 nm inside the metal layer [5, 12, 24]. As a result, surface plasmon polaritons propagate longitudinally along the interface with both electromagnetic fields and charge oscillations highly localized near the interface [12, 22].

The wavevector of the SPP ($k_{SPP} = 2\pi/\lambda_{SPP}$) is given by [26]:

$$k_{SPP} = k_0\sqrt{\frac{\varepsilon_d \cdot \varepsilon_m}{\varepsilon_d + \varepsilon_m}} \tag{2.3}$$

where k_0 is the free-space wavevector ($k_0 = 2\pi/\lambda_0$) with λ_0 being the free space wavelength of the incident light, ε_d and ε_m being the relative permittivity of the dielectric and metallic materials, respectively.

The dispersion relation is plotted in Fig. 2.4 for the SPPs along a SiO_2 and Ag interface with both the SiO_2 and Ag being semi-infinite in thickness [29], calculated from the optical constants in Johnson and Christy's work [27].

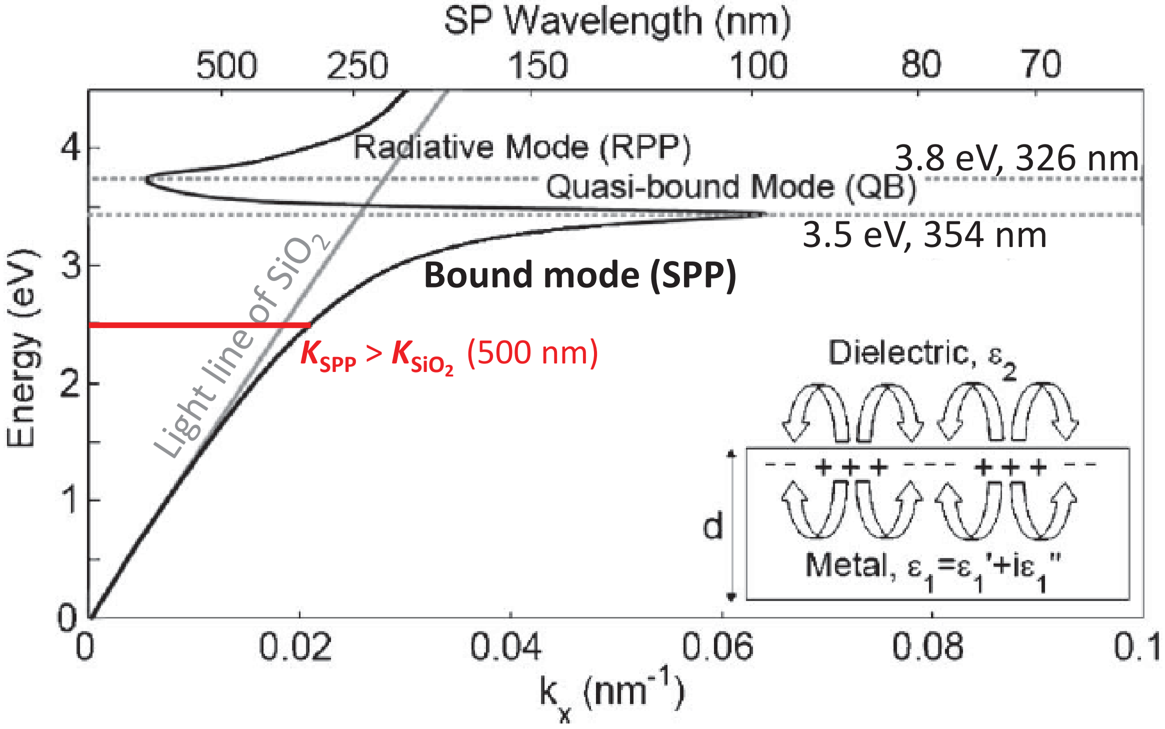

Fig. 2.4 The dispersion of bound (SPP), radiative plasmon polariton and quasi-bound surface plasmon dispersion relations for SiO_2/Ag interface. The light line of SiO_2 is also shown as a reference. The inset shows the resonant interaction between the electric fields and the electrons in the metal. (from Ref. [29]).

In Fig. 2.4, the bound modes with energy below 3.5 eV are surface waves, *i.e.* SPPs; the radiative modes with energy higher than 3.8 eV will propagate into the bulk

[29]. The radiative modes won't be considered further because Ag is not metal-like at these high frequencies [22].

The SPPs have large wavevectors near the resonance energy of 3.5 eV and the SPP dispersion line approaches the light line at short wavelengths. Yet, the wavevector of the SPP is larger than that of light in SiO_2 for all the wavelengths; $k_{SPP} > k_{SiO_2}$ as marked at 500 nm in Fig. 2.4 for example. Therefore, the SPPs cannot be excited directly from light impinging onto a smooth metal surface due to the momentum/wavevector mismatch.

A light wave can be couple to surface plasmons only if the wavevector component along the metal/dielectric interface (longitudinal direction) matches that of the surface plasmon. Couplers are used to generate evanescent waves with larger wavevectors or to increase the longitudinal momentum of the incident light for SPP excitation. Commonly used SPP excitation methods are shown in Fig. 2.5 [24].

Schemes in Fig. 2.5 (a) and (b) utilize the prism as a coupler (the Kretschmann and Raether [21] and Otto [20] setup, respectively). Evanescent waves are generated from the total internal reflection at the prism base, which will penetrate the thin metal or air film and propagate along the metal/dielectric or metal/air interface. By adjusting the light incident angle in Fig. 2.5 (a) and (b), the propagating constant of the evanescent wave can be adjusted to match that of the SPPs for effective SPP excitation [24]. The waveguide coupler in Fig. 2.5 (c) also utilizes the evanescent portion of the waveguide mode. The key point in achieving SPP excitation is matching the wavevector of the waveguide modes and the SPP modes. Common solutions include design of waveguides with high refractive indices, using buffer layers between the waveguide and the SPP supporting structures for enhanced coupling efficiency, etc. Gratings are great tools to adjust the longitudinal momentum of the incident light, thus can be used to excite SPPs. The diffraction is described by the grating equation: $\Lambda \cdot \left(sin(\beta) - sin(\theta)\right) = m\lambda$, where Λ is the grating pitch, m the diffraction order, λ the incident wavelength, θ and β the absolute values of the incident and diffraction angles, respectively. Large longitudinal momentum is achieved with large diffraction angle β.

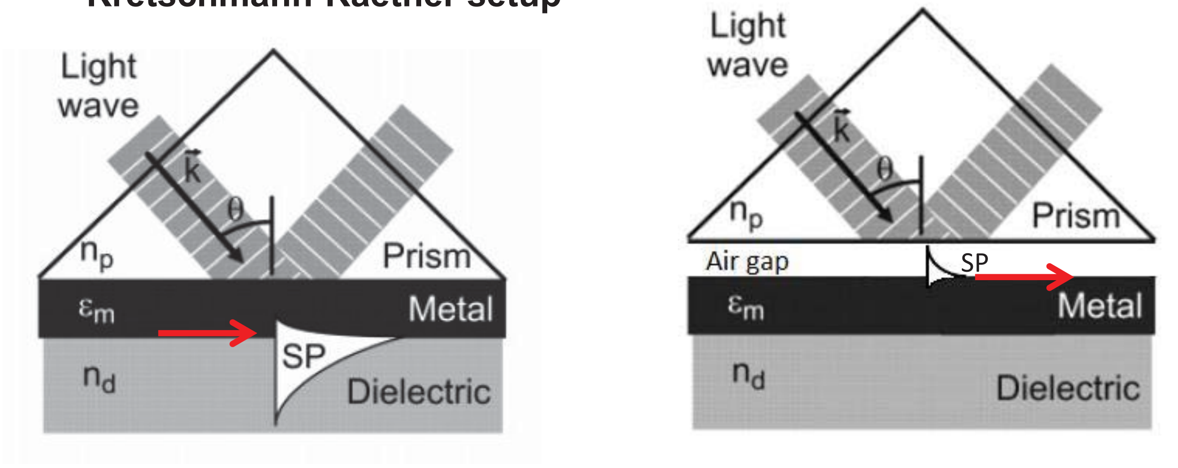

(a) Prism coupler, Kretschmann-Raether setup

(b) Prism coupler, Otto setup

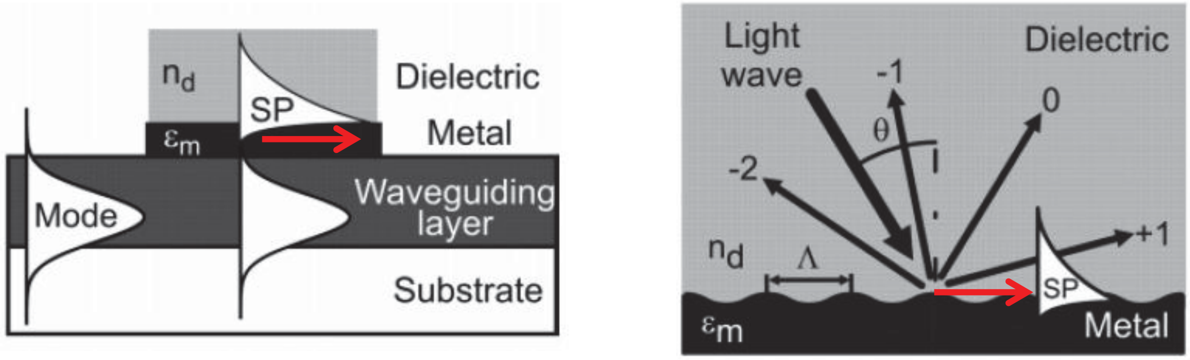

(c) Waveguide coupler

(d) Grating coupler

Fig. 2.5 Common methods to couple light waves to SPPs, via a prism (a) the Kretschmann-Raether setup and (b) the Otto setup; via (c) a waveguide and (d) a grating (figures (a), (c) and (d) from Ref. [24], (b) modified from (a)).

2.2 Application of surface plasmons

My research mainly involves the SPPs or the propagating SPRs. The localized SPR won't be investigated in further details. In this section, the applications of SPPs in my previous works will be presented. This section is based on two papers I've published, please refer to the two papers for detailed discussions:

(1) Yifen Liu, Yu Liu and Jaeyoun Kim, "Characteristics of Plasmonic Bragg Reflectors with insulator width modulated in sawtooth profiles", Optics Express, v.18, pp.11589-11598, 2010.

(2) Yifen Liu and Jaeyoun Kim, "Numerical Investigation of Finite Thickness Metal-Insulator-Metal Structure for Waveguide-based Surface Plasmon Resonance Biosensing", Sensors and Actuators B: Chemical, v. 148, pp. 23-28, 2010.

2.2.1 Waveguide-based plasmonic biosensors

The high localization of electromagnetic fields near the SPP supporting interface makes the SPPs very sensitive to changes near the interface [24], such as the changes of refractive index of the dielectric materials, adhesions of biochemical materials onto the surface, changes of surface roughness, etc. This enables sensors to be developed with compact sizes and high sensitivities.

As demonstrated in Fig. 2.5 (a) and (b), the excitation of SPPs with prism couplers normally requires stringently aligned, complex optical setups. Waveguide based SPP excitation allows the realization of compact and rugged SPR sensors. Typical waveguide-based SPR configurations comprise polymer or glass waveguides with a single-layer metallic thin film to support the SPP, as shown in Fig. 2.5 (c). The SPPs are excited by the evanescent portion of the waveguide mode through mode coupling process.

Our new design of finite metal-insulator-metal (f-MIM) SPPs as shown in Fig. 2.6 (b) allows better match between the propagation constants of the waveguide modes (β_{gw}) and the SPP (β_{SPP}) around 780 nm, which is the desired wavelength for biosensing. As a result, more energy from the waveguide mode is coupled into the surface plasmon sensing areas, achieving higher sensitivity. Moreover, the SPP does not interrupt the waveguide mode, allowing easy integration of SPR sensors with waveguide arrays.

Fig. 2.6 (a) shows the sensing unit with the SPPs excited by a polymer-based waveguide with core index of 1.54 and cladding index of 1.48. The design of the SPP supporting f-MIM is shown in Fig. 2.6 (b) in more details, with the superstrate the sensing volume (water in this case) and the substrate the upper cladding of the waveguide. Ta_2O_5 was chosen as the insulator material (n_i = 2.22) and gold is used as the metal which is modeled using Ref. [27].

For a wide range of wavelength, the effective index of the waveguide mode n_{gw} ($n_{gw} = \lambda_0/(2\pi) \cdot \beta_{gw}$) of the waveguide's fundamental mode is approximately 1.52. So, for efficient coupling to the SPP, we need to match the effective index of the SPP ($n_{SPP} = \lambda_0/(2\pi) \cdot \beta_{SPP}$) to n_{gw}. The dispersion of the SPP supported by the 5-layer f-MIM structure with ($d_{m2}/d_i/d_{m1}$) = (50/75/15) nm is plotted in Fig. 2.6 (c) (red line with triangular markers). Clearly, the β_{SPP} matches β_{gw} (the circled area), which is between the two light lines of 1.54 and 1.48, when the incident light is around 780 nm. For comparisons, the dispersion of SPPs supported by a 50 nm single Au layer is added (black line with circular markers) which showed that n_{SPP} approaches n_{gw} in waveguiding regime (1.48~1.54) only in short wavelength regime ($\lambda_o \sim 540$ nm), where the absorption due to metal and water increases and limits the sensing area.

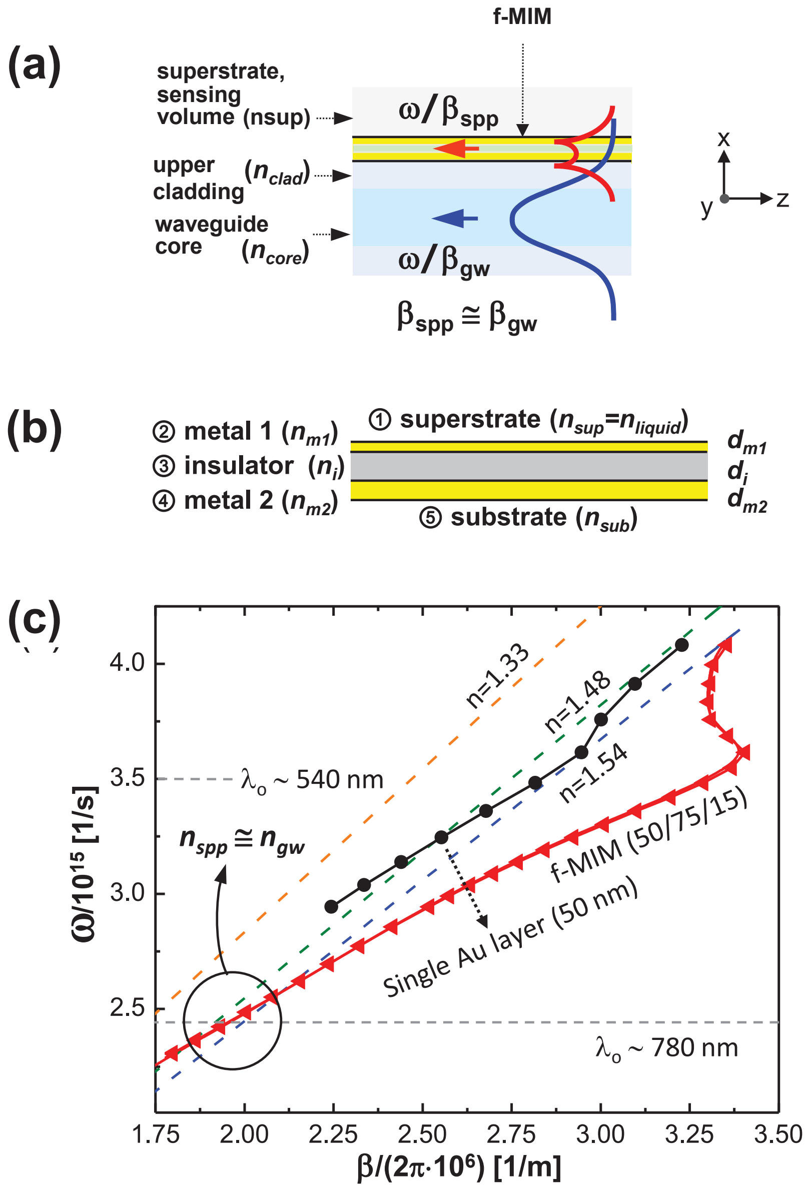

Fig. 2.6 (a) Waveguide-based excitation of SPPs supported by the finite thickness metal-insulator-metal (f-MIM) structure; (b) Schematic structure of f-MIM; (c) The dispersion diagram of SPP modes supported by a f-MIM with $(d_{m2}/d_i/d_{m1})$ = (50/75/15) nm, respectively. The dispersion of SPP modes supported by a 50 nm Au layer is also added for comparisons.

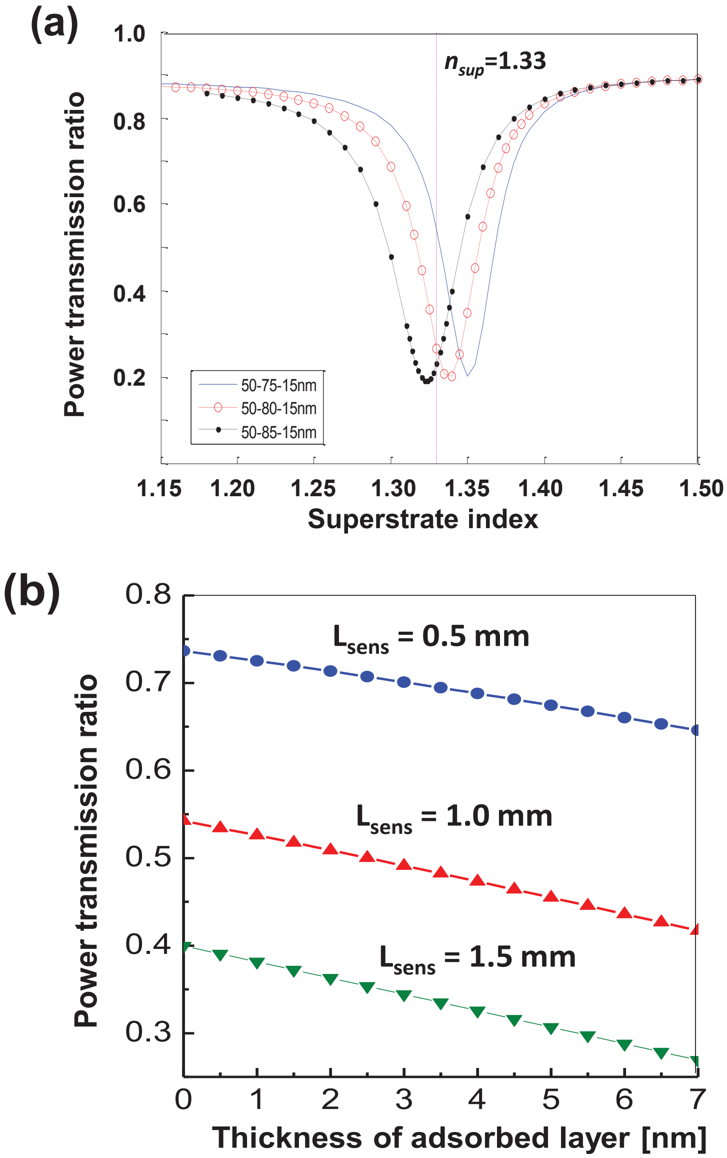

Fig. 2.7 The power transmission ratio of the f-MIM/WG mode for (a) the refractometric sensing mode, as a function of n_{sup} for three different values of insulator layer thickness. The blue curve for ($d_{m2}/d_i /d_{m1}$) = (50/75/15) nm is optimized for sensing with n_{sup} = 1.33. (b) the affinity sensing, different sensing section lengths (L_{sens}) have similar sensitivities.

With high coupling efficiency (η_{coup}), changes near the SPP modes can be detected through the changes in the output power level of the waveguide. Two different sensing types were simulated. In refractometry mode, n_{sup} was varied as a whole. In affinity sensing mode, a thin layer of index higher than n_{sup}, $n_{ads} = 1.42$ which is a typical value for proteins, was assumed to be adsorbed on the f-MIM surface. The length of the sensing section (L_{sens}) is set at 1 mm, the width of a typical microfluidic channel. The sensing results of the two modes are shown in Fig. 2.7.

In the refractometric sensing mode, when $(d_{m2}/d_i/d_{m1})$ = (50/75/15) nm (blue curve in Fig. 2.7 (a)), the f-MIM-based matching of propagation constants set the transmission dip at n_{sup}= 1.35, rendering the rate of change in the waveguide output power maximized at n_{sup}= 1.33. Assuming the ability to detect 0.03% change in intensity, the sensing resolution of refractometry mode was 1.53×10^{-5} RIU. The operation point in n_{sup} can be easily tuned to higher values by decreasing d_i. In the affinity sensing mode, the changes in power transmission ratio are shown in Fig. 2.7 (b) as a function of the adsorption layer thickness and the sensor length (L_{sens}). Assuming the ability to detect 0.03% change in intensity again, the sensing resolution in thickness was 0.016 nm.

2.2.2 Nanoscale plasmonic Bragg reflectors

On the SPP supporting surface, the strong localization of electromagnetic fields can be used to guide light in subwavelength structures. This allows the realization of sub-wavelength scale device [11, 12, 30]. With metal insulator metal (MIM) as the fundamental SPP guiding unit [30], I designed Bragg reflectors with swatooth profiles (Fig. 2.8 (b) and (d)). The effective index of SPPs supported by MIM structures is strongly dependent on the thickness of the insulator layer [30]. By concatenating MIM units with different insulator thicknesses, the alternating effective indices act as a plasmonic Bragg reflector (PBR), with strong reflection inside the bandgap near the Bragg wavelength λ_B. Compared with the step profiles (Fig. 2.8 (a) and (c)), the smoother transition between the widest and narrowest parts of the PBR renders lower insertion loss, narrower bandgap, and reduced rippling in the transmission spectrum.

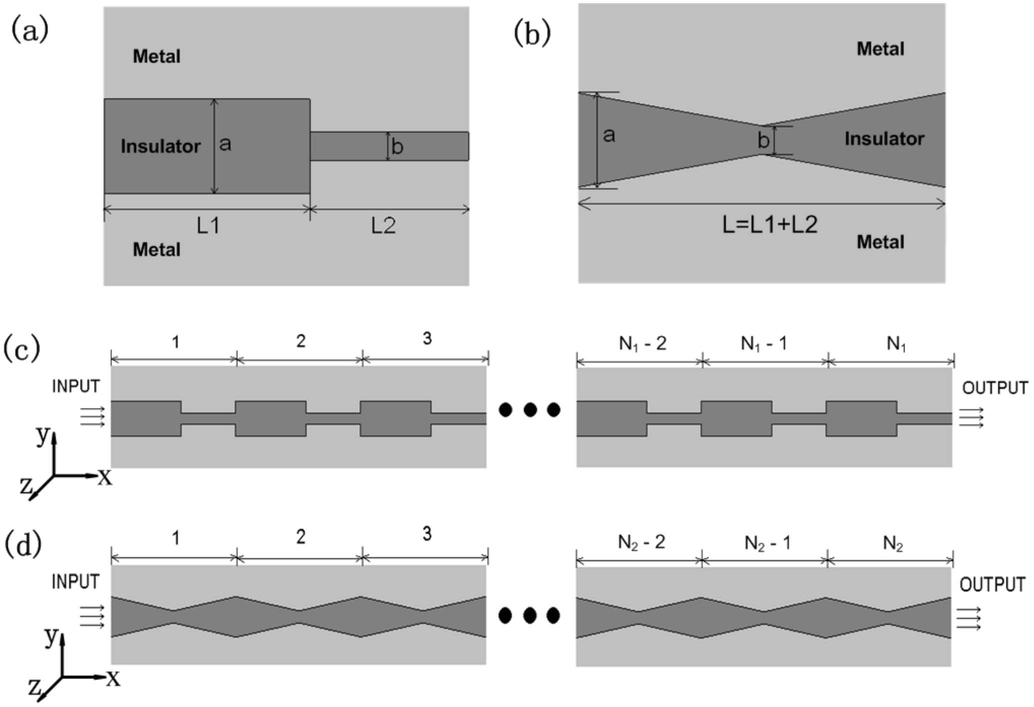

Fig. 2.8. The unit cells of (a) a step PBR and (b) a sawtooth PBR. (c) and (d) show the corresponding PBRs realized by concatenating the unit cells.

The Bragg wavelength λ_B was set to the telecom wavelength 1.55 μm. SiO_2 (n = 1.46) was used as the insulator material and Ag as the metal for its low loss and high plasmonic activity. We fixed a = 100 nm and used two different values of b to study the impact of having a strong (b = 30 nm) or a weak (b = 70 nm) width modulation. The geometries in Fig. 2.8 (a) and (b) are designed following the Bragg condition: $\lambda_B = 4\cdot L_1\cdot n_a = 4\cdot L_2\cdot n_b$ where n_a, n_b, and λ_B are the effective indices of SPP modes. For a = 100 nm and b = 30 nm, L_1 and L_2 were 220 nm and 170 nm, respectively. For b = 70 nm, L_2 became 208 nm.

We set the N_1 and N_2 values for step and sawtooth PBR different to bring the two PBRs' transmission levels at λ_B as close to each other as possible so that the comparisons on the transmission characteristics *outside* the bandgap would be fair and meaningful.

For PBRs with a = 100 nm and b = 30 nm, with N_1 = 6 and N_2 = 8, the difference in their transmission levels at λ_B falls within 4 dB (-40.7 dB for step and -37.0 dB for sawtooth PBRs). Figure 2.9 (a) shows the two PBRs' transmission spectra. The 3 dB bandwidth of the sawtooth PBR bandgap was 694 nm which was 43.8% narrower than the 1234 nm bandwidth of the step PBR. In the case of the sawtooth PBR, the modulation depth of the ripples beyond the band edges was < 40% of that of the step PBR, except for the one closes to the band edge. Figure 2.9 (a) shows that the reduction in rippling in the transmission spectrum led to highly enhanced transmission levels outside the bandgap. For PBRs with smoother transition profiles a = 100 nm and b = 70 nm, setting N_1 = 12 and N_2 = 18 resulted in transmission levels of -25.2 dB and -25.5 dB for the step and sawtooth PBR, respectively. The transmission spectra in Fig. 2.9 (b) showed that the width of the sawtooth PBR bandgap was 282 nm which was 39.7% narrower than the 468 nm observed from the step PBR. The level of rippling in the transmission spectrum and the level of transmission outside the bandgaps were also more favorable in the case of the sawtooth PBR. In fact, the narrower bandgap, higher transmission levels and lower spectral rippling outside the bandgap, are consistently maintained for all values of b between 30 and 70 nm (a = 100 nm) as well.

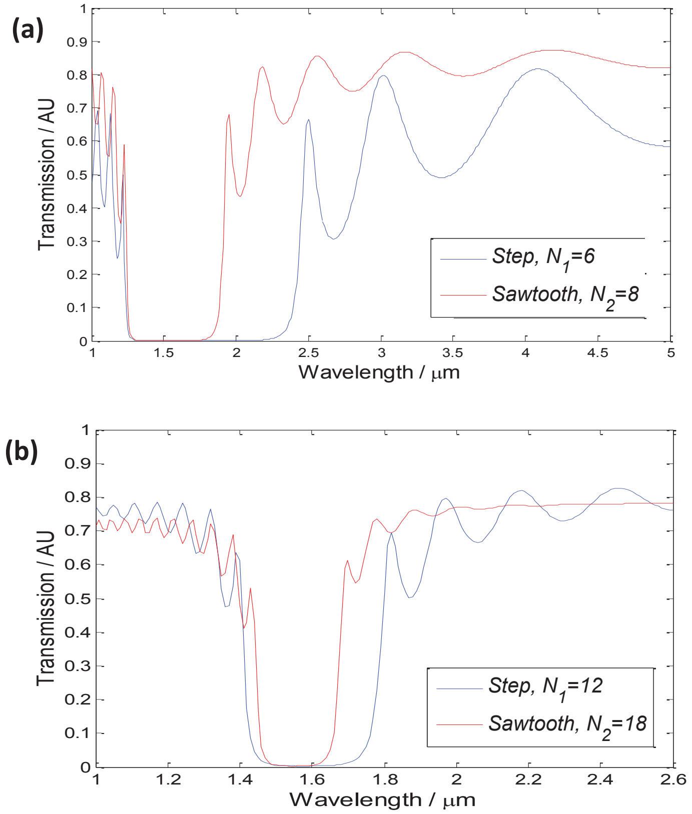

Fig. 2.9. Transmission spectra for the step and sawtooth PBRs with (a) a = 100 nm, b = 30 nm and (b) a = 100 nm, b = 70 nm. The bandgap for sawtooth PBR is 43.8% narrower than the step PBR in (a) and 39.7% narrower in (b).

2.3 Organic solar cells

2.3.1 Fundaments of solar cells

Figure 2.10 shows the idealized relation between energy levels (vertical axis) and the spatial positions (horizontal axis) in solar cells [4]. Ground state electrons are those in the valence band (VB) in inorganic semiconductors or the highest occupied molecular orbital (HOMO) in organic semiconductors. Upon sunlight exposure of solar cells, photons hit ground state electrons and pump them to excited states (the conduction band (CB) in inorganic semiconductors or the lowest unoccupied molecular orbital (LUMO) in organic semiconductors). A cathode selectively collets these high energy excited electrons and drives them to the external circuit. The electrons lose their energy while driving the external load and returned to the solar cell through the anode, back to the ground states with the same energy that they started with.

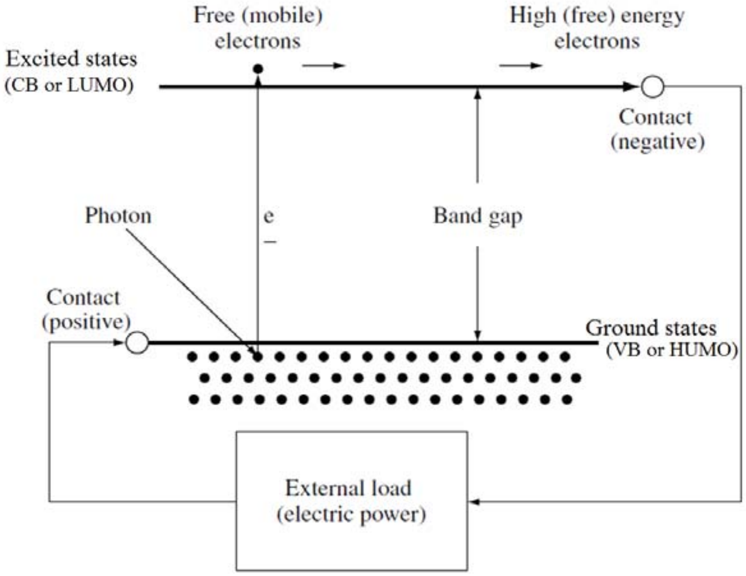

Fig. 2.10 Schematic of a solar cell. Electrons are pumped by photons from ground states to excited states. There they are extracted at a higher (free) energy and delivered to the external load for useful works, then are returned to the ground state.(modified from Ref. [4])

The equivalent circuit of solar cells is shown in Fig. 2.11 (a). With no light applied, the current-voltage (IV) characteristics of most solar cells resemble an diode which is represented by I_d . The solar cell IV response under illumination is the superposition of photocurrent I_L and I_d with the non-ideality factor taken into account through the shunt resistance R_{SH} and the series resistance R_S. The IV characteristic is then described by [4]:

$$I = I_L - I_0\left(exp\left(\frac{q(V+IR_S)}{nkT}\right) - 1\right) - \frac{V+IR_S}{R_{SH}} \tag{2.4}$$

where I and V are the current and voltage over the external load, q is the electron charge, k the Boltzmann constant and T the temperature, n is the ideality factor.

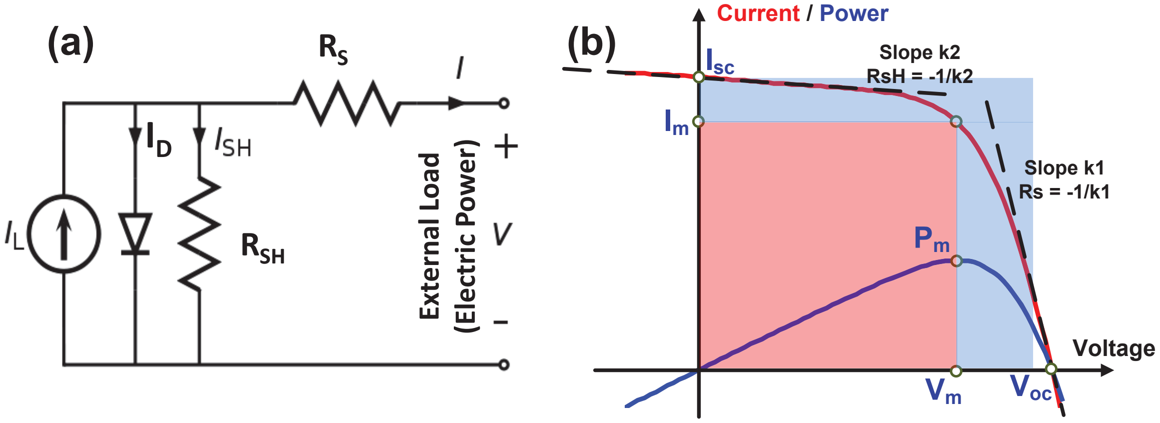

Fig. 2.11 (a) The equivalent circuit of a solar cell, with I_L and I_d as the photocurrent and diode current, respectively. (b) A typical IV curve (red) and the corresponding generated power (blue) of a solar cell, the optimized operation point is marked (I_m, V_m)

Figure 2.11 (b) shows a typical IV curve (red line), which is normally plotted in the first quadrant even though it falls in the fourth quadrant with the signs of I and V reversed. The important parameters of the IV curve include the open-circuit voltage V_{OC} and the short circuit current I_{SC}. As shown in Fig. 2.11 (b), the R_{SH} and R_S can be calculated from the slopes of the IV curves near the I_{SC} $(V = 0)$ and V_{OC} $(I = 0)$ points, respectively.

The solar cell generated power is also shown in Fig. 2.11 (b) with the blue curve. Clearly, the optimized operation point is where the output power is maximized. The maximum power P_m and the corresponding operation current I_m and voltage V_m are also marked in the IV plot. One important solar cell figure of merit is the fill factor (FF), which shows the squareness of the IV characteristic [4] using the ratio between the areas of the pink rectangle and the blue one in Fig. 2.11 (b).

$$FF = \frac{V_m \cdot I_m}{V_{OC} \cdot I_{SC}} \tag{2.5}$$

The overall performance of the solar cell is represented by the power conversion efficiency (PCE, η), which is defined as the percent ratio of the input light power and the converted electric power.

$$\eta = \frac{P_{out}}{P_{light}} = \frac{V_{OC} \cdot J_{SC} \cdot FF}{P_{light}} \tag{2.6}$$

Where J_{SC} is the current density in mA/cm^2, which is defined as $J_{SC} = I_{SC}/A$ with A the area of the solar cell device. The JV curve is sometimes used rather than IV to evaluate the solar cell efficiency.

For solar cell performance evaluation, the solar spectrum AM1.5G (Air mass 1.5 global) with $P_{light} = 100mW/cm^2$ is used as the standard spectrum. According to American Society for Testing and Materials (ASTM), AM1.5G is considered a reasonable average for the 48 contiguous states of the USA over a period of one year [31].

Prominent research solar cells with National Renewable Energy Laboratory (NREL) certified efficiencies for various PV conversion technologies are shown in Fig. 2.12 [32], with the data updated in Feb 2012.

Despite the 43.5% efficiency achieved by Solar Junction with tandem cells of three junctions and with light concentrators, its mass production and application are likely to be hindered by the high cost. A large percentage of the cost of crystalline silicon based solar panels, which are the dominant type in the current solar market, is for the silicon wafers. Thin-film PVs based on amorphous or organic materials attract an increasing level of interest as low-cost alternatives to crystalline Si devices. For example, the active layer thickness can be as thin as ~ 100 nm in thin-film organic solar cells.

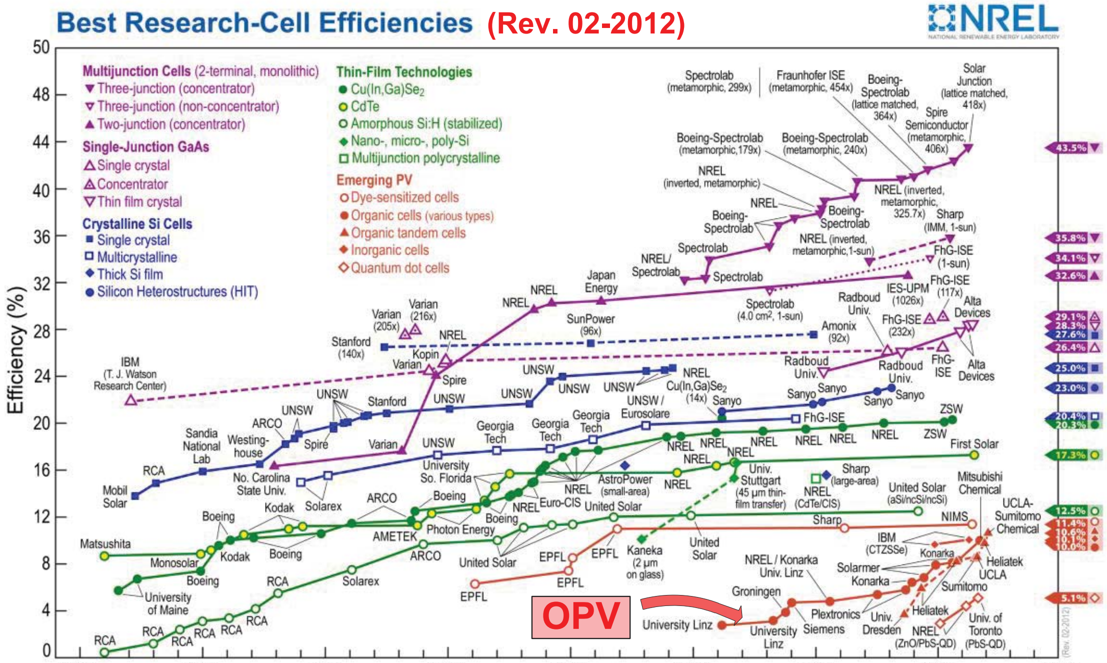

Fig. 2.12 Best NREL-certified efficiencies of various types of research solar cells till Feb 2012. (from Ref. [32])

2.3.2 Organic solar cells

Organic solar cells use polymers and small molecules as the photoactive materials. Macromolecules with a molecular weight larger than 10000 are called polymers, whereas lighter molecules are referred to as "oligomers" or "small molecules" [33]. Tang and Albrecht [34] demonstrated photovoltaic effect with organic materials with PCE of 0.001% in 1975. Tang [35] brought the efficiency to 1% in 1986 with two layers of different small molecule materials, which is referred to a planar bilayer heterojunction device architecture. In 1990, Hiramoto *et al.* first demonstrated, with a 0.7% small molecule OPV, the idea of mixing the donor and acceptor materials in one layer, which is later referred as the bulk heterojunction device architecture. The discovery of photoinduced charge transfer from a conjugated polymer to C_{60} in 1992 set the foundation for polymer based OPVs [36]. However, the bilayer junction approach suffered low PCE (<0.1%) due to insufficient interfacial contact area between the donor and acceptor layers [37, 38]. Again, forming a bulk heterojunction helped improve the PCE [38-40]. Yu and Heeger achieved 0.9% in 1995 [40] while 2.5% was achieved by Shaheen *et al.* in 2001 [38]. As OPV keeps attracting more research interest, there has been a continuous progress in the synthesis of new semiconducting organic materials, the development of different device architectures and the incorporation of light trapping schemes [5, 33, 41, 42]. Therefore, the OPV efficiency has been increased rapidly as shown in Fig. 2.12 between 2001 ~ 2012. For small molecule OPVs, with fullerene C_{60} as the new acceptor and copper phthalocyanine (CuPc) as the donor, the PCE is improved to 4.2% [43]; recently, Sun *et al.* further enhanced the efficiency to 6.7% [44]. For polymer-based OPVs, the highest efficiency for single junction solar cell has reached 10% [32]. With two polymers in a tandem OPV absorbing complementary portions of the solar spectrum, Dou *et al.* achieved the new world record with a OPV efficiency of 10.6% [32, 41].

OPVs have gained a broad interest due to the rapidly increasing efficiency and their potential in achieving the high throughput fabrication of large area, flexible and low cost devices [33]. The work in this thesis only involves polymer-based OPVs. Small molecules are not discussed. One major advantage of conjugated semiconducting polymers over inorganic semiconductors is the enormous possibilities to make change to the polymer’s chemical structure and thus tailor their properties [7]. Adding side chains to the polymer backbone or changing the position of the side chains are common approaches, while making copolymers makes the combinatorial library rapidly grow in size [7]. The structural changes in polymers influence numerous optical, chemical and electrical properties, such as the color and solubility of the polymer, the energy levels and bandgap, the morphology, charge transport characteristics and the conductivity [7, 33, 42]. As a result, the chemical structure of polymers and the corresponding processing methods impose huge impacts on the PCE of the devices. This is also the reason that recent advances in high efficiency OPVs generally involve new polymers and that great effort has been investigated on developing new polymers for improved light absorption and charge transport [33, 41, 42].

One of the most researched OPV materials to date is the mixture of Poly(3-hexylthiophene-2,5-diyl) (P3HT) as the donor and <6,6>-phenyl-C61 butyric acid methyl ester (PCBM) [33, 42, 45-49] as the acceptor. Efficiency of 4.4% was reported by Li *et al.* [50], ~5% were reported by Reyes-Reyes *et al.* [51] and Ma *et al.* [52].

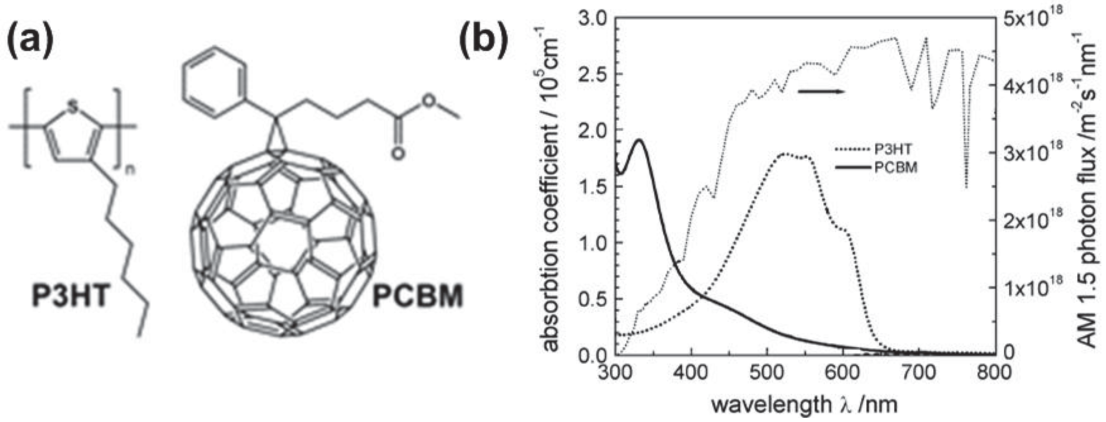

Fig. 2.13 (a) The structure and (b) the absorption coefficients of P3HT and PCBM ((a) from Ref. [33] and (b) from Ref. [47])

The chemical structures in Fig. 2.13 (a) [33] schematically shows the repeating structural unit of P3HT and the fullerene derivative PCBM. The absorption coefficients of

P3HT and PCBM are shown in Fig. 2.13 (b) [47], together with the AM1.5G solar spectrum. Compared with Si based solar cells which response to wavelengths as long as 1100 nm, P3HT:PCBM absorbs light within a narrower spectrum. This is because of the narrower bands for electrons in both the ground states and excited states [53]. However, P3HT has high absorption coefficient which is near $1.8 \times 10^5\ cm^{-1}$ at 550 nm [47], while it is less than $10^4\ cm^{-1}$ for Si [4].

A schematic view of the OPV's working principle is given in Fig. 2.14, with the markers ① ~ ④ showing the photovoltaic effect [48]. Though this schematic figure applies to various OPVs with different materials, in the following discussion, the donor and acceptor are assumed to be P3HT and PCBM, respectively.

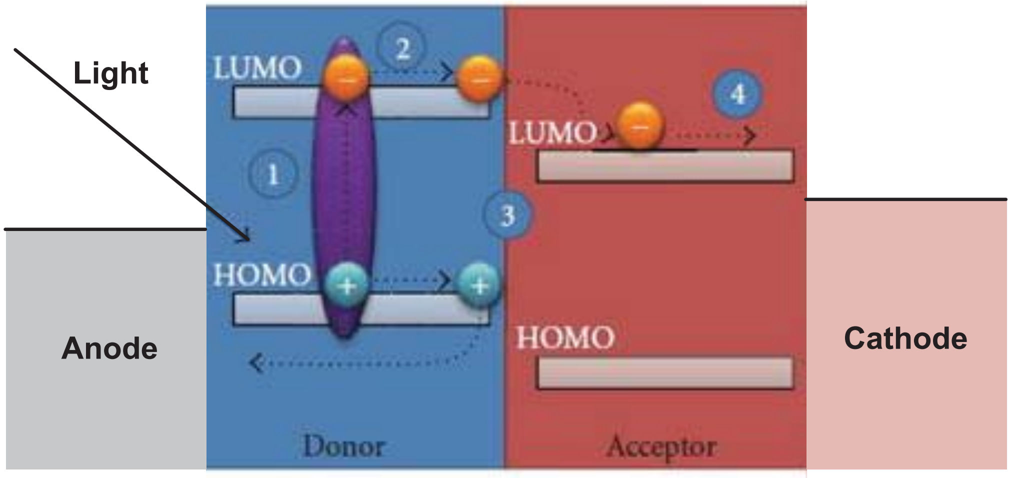

Fig. 2.14 The schematic view of OPV with markers ① ~ ④ showing the steps of the current generating process. (modified from Ref. [48])

Since most of the light absorption happens inside the P3HT (donor), as suggested by Fig. 2.13 (b), photo-generated excitons (bound electron-hole pairs) will be formed inside the P3HT (step ① in Fig. 2.14). Due to the differences in the HOMO and LUMO levels of P3HT (LUMO: 3.0 eV and HOMO: 5.0 eV) and PCBM (LUMO: 3.7 eV and

HOMO: 6.1 eV) [45], a heterojunction is form at the interface between P3HT and PCBM. As the excitons diffuse to the P3HT/PCBM interface (step ②), the electron and hole pairs can be efficiently dissociated into free carriers and the electrons can jump to the LUMO of the acceptor (step ③) [33]. Due to the lower HOMO of the acceptor than that of the donor, the hole will stay at the HOMO of the donor. By using an anode to collect holes from the donor side and a cathode for electron at the acceptor side, electricity can be generated along the external load.

The most straight-forward approach to realize the heterojunction between P3HT and PCBM is to form a bi-layer structure [33]. However, the exciton diffusion length in step ② in Fig. 2.14 is typically a few tens of nanometers [33]. As a result, the donor and acceptor layers much be very thin for efficient collection of charge carriers, which restricts the use of a thicker film for higher light absorption.

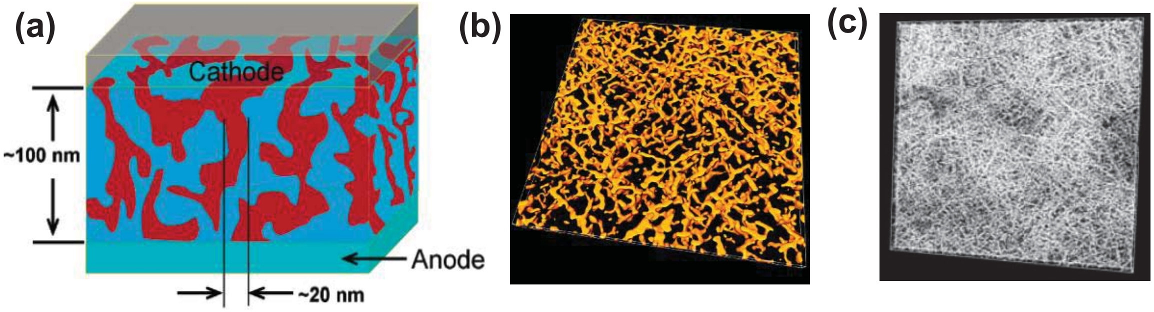

Fig. 2.15 (a) A schematic view of the phase separation of donor and acceptor in a bulk heterojunction OPV; (b) Artwork shows in detail the phase separation network forming paths for charge carriers to move freely in the photoactive layer; and (c) Electron tomography images of P3HT:PCBM blend, the dimensions are 1700×1700×100 nm^3. ((a) from Ref. [54]; (b) and (c) from Ref. [49])

The bulk heterojuction approach solves this conflict in choosing the active layer thickness and helpes to improve the PCE. For a bulk heterujunction OPV, the photoactive layer consists of the donor and acceptor phases in a mixture, which offers higher interfacial areas and thus improved exciton dissociation efficiency. A schematic view of phase separation in a bulk heterojunction OPV is shown in Fig. 2.15 (a) with Fig. 2.15 (b) shows the network paths for the charge carriers to move freely in the photoactive layer. This phase separation between P3HT and PCBM was experimentally proven, as shown in Fig. 2.15 (c) [49] for an area of 2.89 μm^2, by the electron tomography method which reconstructs the three-dimensional structure of the mixture from a series of two-dimensional (2D) projections.

2.4 Application of SPRs in OPVs

For a wide application of the OPVs, further improvements in the PCE are required. The bulk heterojunction approach solves the problem of short excitons diffusion length, but it could not overcome the problem of free carrier recombining within the active layer as it gets thicker for enhanced photon absorption. As a result, though the thin PV layer certainly limits PCE by providing insufficient absorption length, especially for long wavelengths near the edge of the absorption band, it is not advised to make the layer thicker due to the accompanying degradation in the carrier collection efficiency [5].

As a solution to the conflicting length-scales for photon absorption and carrier collection, the utilization of SPR has been proposed and demonstrated for improving the solar cell efficiency [5, 25, 55, 56]. As discussed in Section 2.1, both L-SPR and propagating SPPs are highly evanescent and hence can amplify their electric field components far beyond that of the excitation waves. As a result, they can benefit the optical absorption in thin-film solar cells by concentrating the electromagnetic energy near the interface between the photoactive layer and the metal electrode. Besides, SPPs can further benefit the light absorption by redirecting the light to propagate along the active layer, efficiently increasing the light path without physically increasing the thickness of the active layer.

There are two common approaches to add plasmonic structures into thin film solar cells: (1) using metallic particles which will help L-SPR excitation and scatter more light into the active layer; (2) using plasmonic structures such as nano-hole/bump arrays or gratings, which support propagating SPPs and localized SPR modes as well.

2.4.1 L-SPRs in OPVs

To incorporate plasmonic particles into thin film PVs, Au or Ag nanoparticles are commonly added at the surface of solar cells at the light incident side so that they are in front of the active photovoltaic layer [16, 56-58]. The nanoparticles not only act as efficient scatterers to get more light into the active layer, but also as strong field amplifiers based on L-SPRs, leading to enhanced light absorption and photocurrent. Fig. 2.16 (a) shows an example of mixing Au nanoparticles with a buffer layer which was originally part of the device [16]. Au particle colloid and poly(3,4-ethylenedioxythiophene): poly(styrene sulfonate) (PEDOT:PSS) solution are mixed and then spin-coated as a single layer. The superstrate-type solar cell configuration in Fig. 2.16 (a) with light entering from the glass side allows the light to interact with the particles before reaching the photoactive layer. The diameters of the particles are around 30 ~ 40 nm, whose resonance peak matches the absorption band of P3HT:PCBM [16].

The external quantum efficiency (EQE) curves in Fig. 2.16 (b) suggest that 10% ~ 30% Au particle colloid in PEDOT:PSS solution help improve the light absorption while

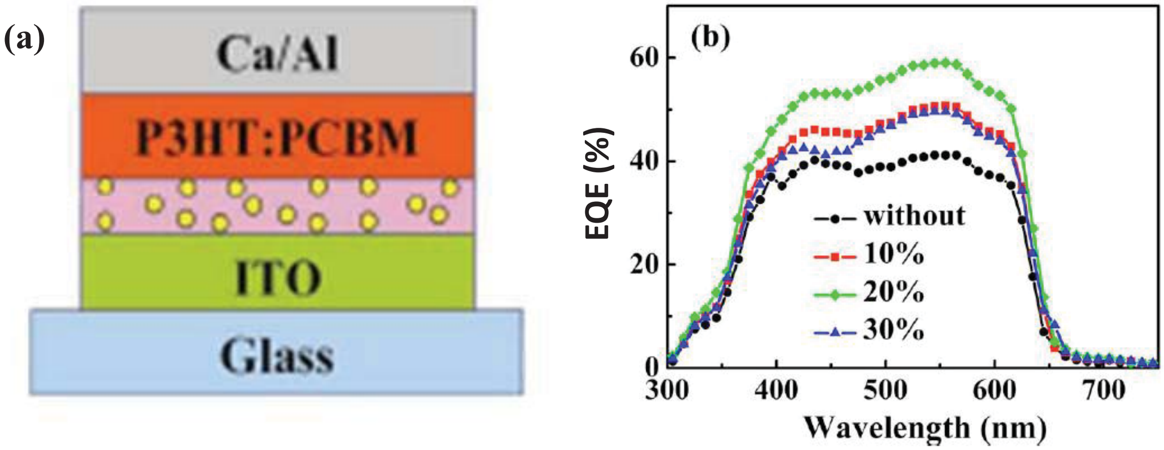

Fig. 2.16 (a) Schematic representation of the PV device with PEDOT:PSS doped with Au nanoparticle colloids of various concentrations. (b) The external quantum efficiency curves of OPV devices. (from Ref. [16])

20% offers the highest improvement. A clear feature of the particle based EQE enhancement is that the EQE of the original device was low and the particles helped improve the device performance over the entire absorption band, 375 ~ 625 nm in this case. An immediately following question is whether or not plasmonics can help the OPV performance when the OPV already absorbs most of the incident light in the absorption band. It has been pointed out by Wu *et al.* [15] that the interplay between L-SPR and excitons increased the probability of exciton dissociation and facilitated the charge transfer process due to the local enhancement of the electromagnetic field near the Au particles [15]. In this thesis, I also investigate the effect of Ag particles on the performance of OPVs with a different architecture, especially in the case that the light absorption is not much affected.

Metallic gratings or nano-cavity arrays have also been reported theoretically and experimentally in thin-film solar cells for the excitation of L-SPR near the metallic wires to benefit the light absorption with the local enhancement of electromagnetic fields [25, 59].

2.4.2 SPPs in OPVs

The use of the in-plane waves, which propagate in the horizontal direction while being confined within the PV layer, was proposed to enhance the absorption without increasing the PV layer thickness [5-10]. The SPPs generated by grating couplers (Fig. 2.5 (d)) is a good example of in-plane waves. Dielectric gratings have been widely used as light trapping schemes for their ability of efficiently scattering light into the active layer [10, 60, 61]. The utilization of plasmonic gratings in front of the PVs has been reported [9, 62]. Approaches to add plasmonic nano-hole arrays as light trapping schemes at the back of the solar cells have been taken [6, 63] to avoid the shadowing effect when putting metallic structures in front of the solar cells.

Figure 2.17 (a) shows the SEM image of a-Si:H (hydrogenated amorphous silicon) solar cell with plasmonic back reflectors [6]. Instead of increase the EQE over the whole absorption band as shown in Fig. 2.16 (b), the nano-hole array targets at the absorption enhancement near the edge of the a-Si:H absorption band for improved red-response (600 ~ 800 nm) [6].

One challenge in using plasmonic gratings as back reflectors in OPVs lies in the differences between the fabrication processes of inorganic and organic solar cells. The active layer of inorganic thin film PVs are normally fabricated with sputtering or chemical vapor deposition (CVD), for which the coating conformity is not of big concern as seen in Fig. 2.17 (a). However, the polymer layers in OPVs are normally deposited by spin coating of solutions and the film quality can be greatly affected by the substrate roughness.

K. Tvingstedt *et al.* experimentally showed an increase in light absorption and thus the photocurrent in OPVs with two kinds of polymer blends (APFO3/PCBM and APFO Green5/PCBM) [8] using Al grating. The OPV structure is shown in Fig. 2.17 (b) with the polymer thickness of 150 nm, the grating has sinusoidal profile with grating height of 50 nm and pitch 277 nm. However, due to the geometry of the grating, the light absorption enhancement was only prominent for TM waves and the increase in the photocurrent was not significant.

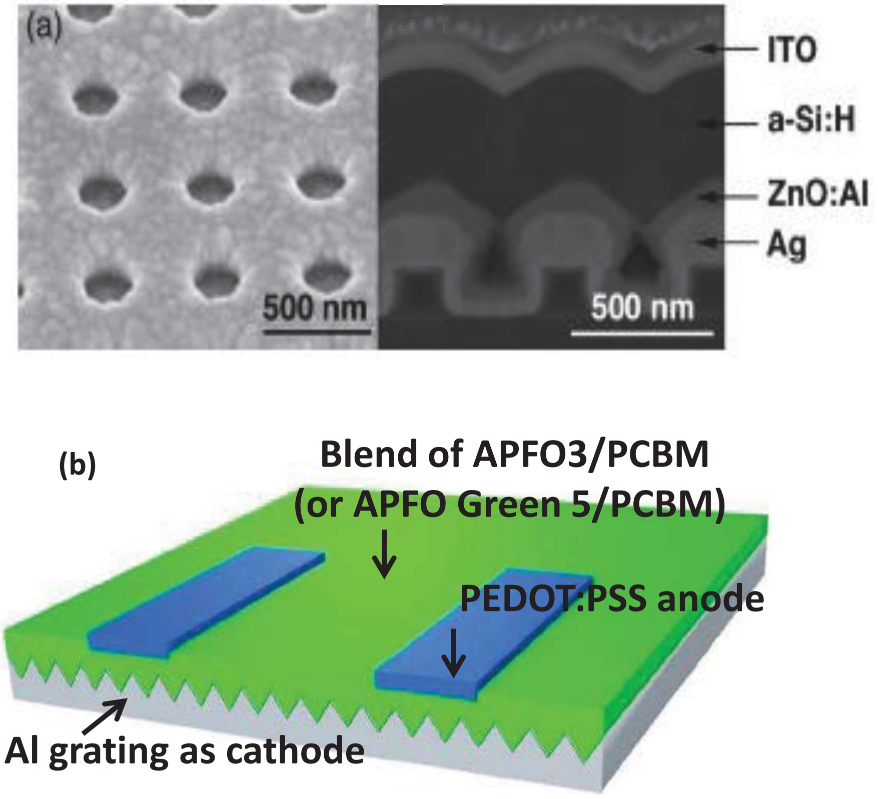

Fig. 2.17 (a) a-Si thin-film solar cell with plasmonic back reflectors and (b) OPV with Al grating as the substrate. ((a) from Ref. [6] and (b) from Ref. [8])

Si based PVs with the active layer less than 300 nm and gratings on the back have been theoretically studied [55, 64-66]. Plasmonic gratings have been used in PVs for absorption enhancement, and their pitch sizes are within 200~400 nm range to match the SPP wavelengths. As a result, the gratings only benefit the absorption of TM waves [8, 62]. The proposed Ag gratings for the absorption enhancement in OPVs in this thesis differ from other similar approaches mainly on two points. (1) Light absorption enhancement for linearly polarized light of all polarization angles is achieved, despite the fact that the Ag gratings are periodic only in one direction. (2) No paper has pointed out that the duty cycle of the grating is even more critical than the pitch of the grating for efficient excitation of SPPs, as demonstrated in this thesis. I also identified two types of in-plane waves propagating laterally along the photoactive layer as the absorption enhancement schemes: SPPs for TM waves and the waveguide modes confined within the PV layer for TE waves.

CHAPTER 3. Numerical simulations of OPVs with metallic gratings

3. 1 OPVs with silver gratings

The proposed OPV structure with a Ag grating back reflector for polarization diverse light absorption enhancement is shown in Fig. 3.1 (b) with the reference structure shown in Fig. 3.1 (a). We chose to implement the grating directly over the glass substrate (n = 1.46) so that it can function dually as the bottom electrode. A ITO (indium tin oxide) layer act as the top transparent electrode. We also added thin layers of Cs_2CO_3 and MoO_3 to improve the collection of electrons [67, 68] and holes [69], respectively. The Cs_2CO_3 layer is ultrathin [67, 68] and thus won't block the SPP modes from reaching into the P3HT:PCBM layer.

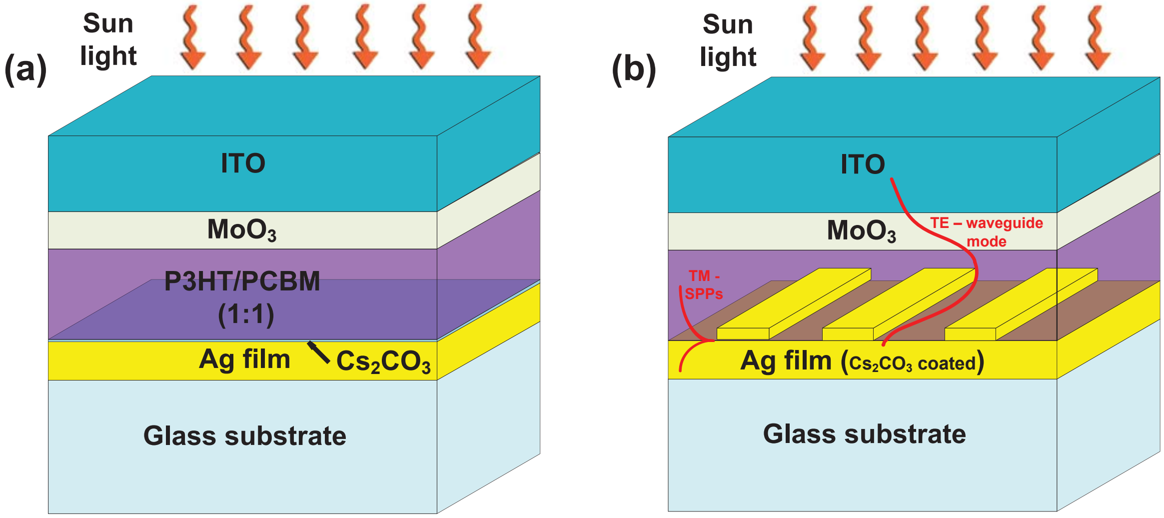

Fig. 3.1 Schematic diagrams of the model OPV device structures (a) without and (b) with Ag gratings. With proper design of the grating geometry in (b), SPPs and waveguide mode can be generated for enhancing the light absorption in TM and TE waves, respectively.

With proper design of the grating geometry, SPPs can be generated along the Ag/P3HT:PCBM interface for TM waves (with the electric field perpendicular to the grating ridges). For TE waves (with the electric field parallel to the grating ridges), the plasmonic grating help generate waveguide mode with most of its energy inside the photoactive layer. Mode profiles of the SPP and waveguide modes are also sketched in Fig. 3.1 (b).

Instead of a planar Ag film in the reference structure in Fig. 3.1 (a), Ag wires are added onto a planar film of the same thickness in Fig. 3.1 (b). The Ag films are set to 100 nm for efficient optical reflection and electrical conduction. The important geometric parameters of the grating in the numerical simulation setup are shown in Fig. 3.2, including the height ***h***, the ridge width ***w***, pitch ***Λ***, and the duty circle of the grating ***D***, defined as the ratio between the ridge width and the pitch (***W***/ **Λ**).

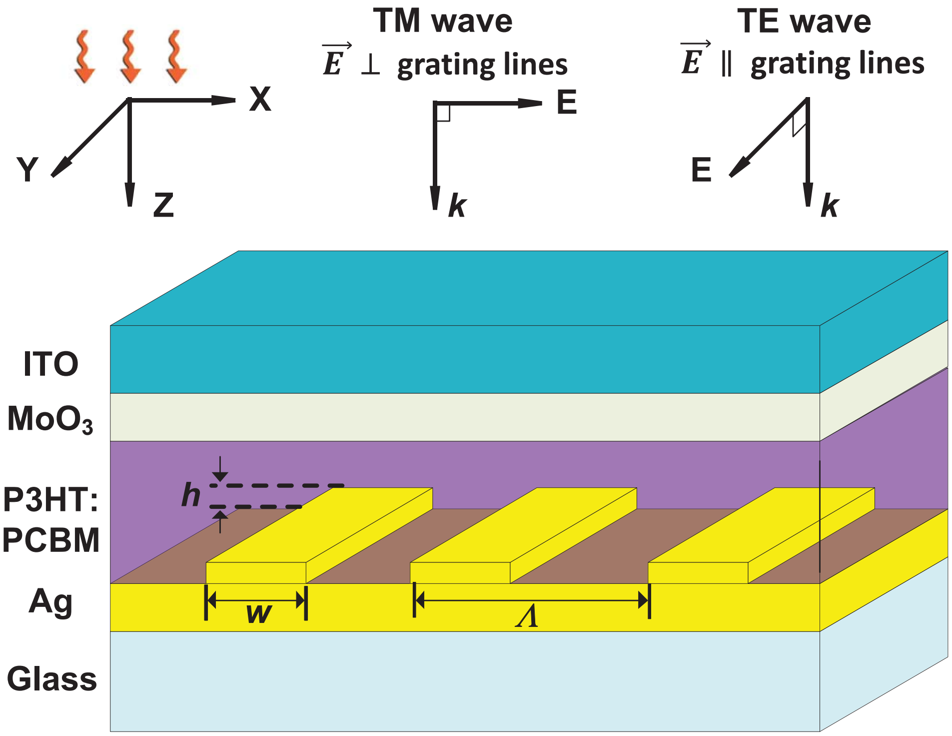

Fig. 3.2 Major structural parameters in the OPV design. The directions of electric field oscillation in TM and TE incoming waves are also specified.

Due to the fact that the Cs_2CO_3 layer can be as thin as 1 nm while maintaining its functionality [45, 68], it is not included in the numerical study in this thesis. For both structures in Fig. 3.1, the polymer, MoO_3 and ITO layers are kept at the same thicknesses. A 200 nm P3HT:PCBM (1:1 in weight) film constitutes the OPV layer. The MoO_3 layer is 15 nm which offers enough protection for the polymer layer during the ITO sputtering [69]. The thickness of the ITO layer is determined through numerical simulations which will be discussed in Section 3.3.

3.2 Simulation setup and method

Finite Element Method (FEM), also known as Finite Element Analysis (FEA), is used for the numerical study of the proposed OPV structures. FEM has been widely adapted in various areas of engineering due to its capability of solving large, complex problems with various geometries, loadings (heat flux, pressure, electric force etc.), and boundary conditions. By breaking a complex structure down into smaller, simpler pieces (finite elements), complex partial differential equations representing the physical problems can be simplified in each element. Then matrices are formed by combing all the simplified equations in the elements. Finally, physical solutions can be obtained by numerically solving the matrices. For the study in this thesis, a commercial software COMSOL Multiphysics 3.5a is used. More specifically, its RF module is used to solve the electromagnetic problems.

Periodic boundary conditions allow me to simulate the periodic gratings using its unit cell. The unit cell of the proposed OPV structure with a Ag grating back reflector is shown in Fig. 3.3 (a), which is discretized into small elements depicted by the fine mesh of the drawing. We took advantage of the software package’s adaptive meshing capability to make the simulation more efficient. Within the MoO_3 layer, which is only 15 nm thick, we set the maximum mesh size to 4 nm. Within larger structures, such as the grating ridge, it was set to 9 nm. To ensure that the meshes were sufficiently fine, we scaled down the overall mesh size (< 5 nm) and the change in the results were below 1%. This suggests that the meshing used is fine enough to generate accurate results.

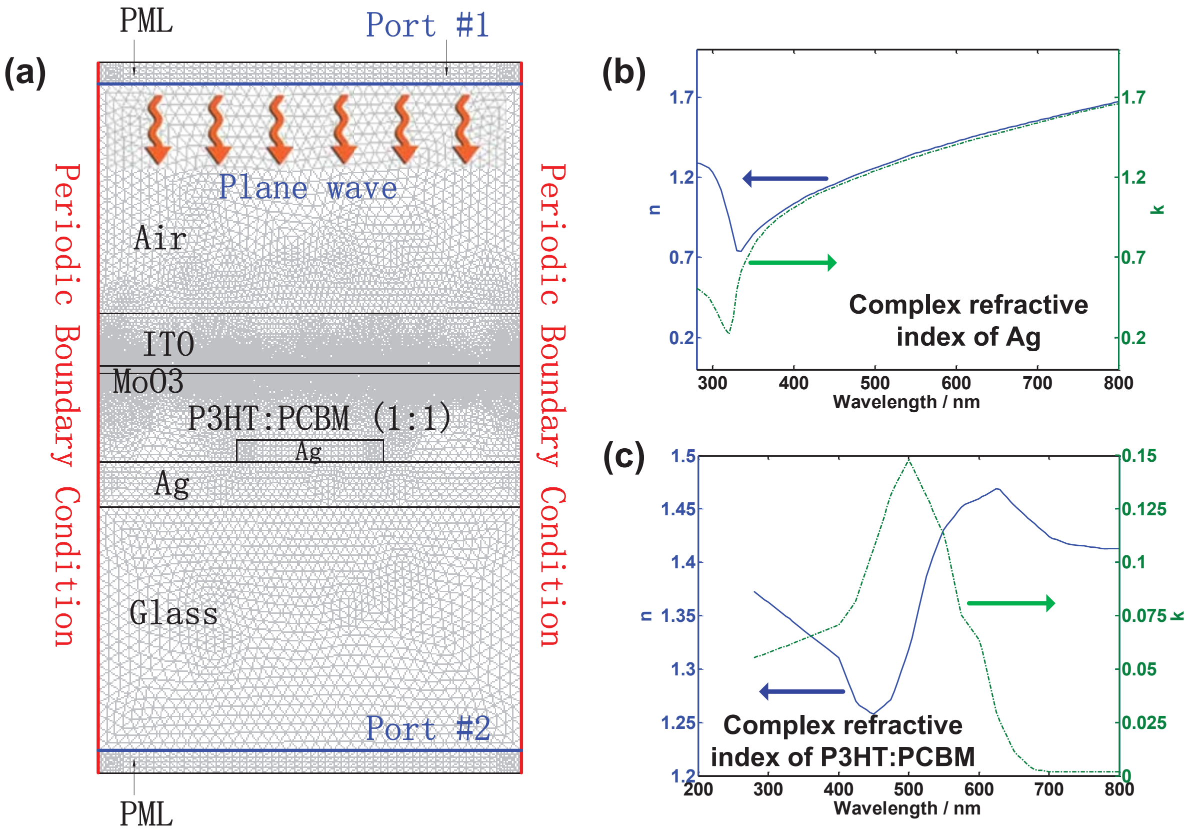

Fig. 3.3 (a) The unit cell of the OPV on Ag grating in COMSOL simulations, showing the meshed-elements, boundary conditions and subdomain conditions. (b) and (c) show the complex refractive indeices of Ag [27] and P3HT: PCBM [70], respectively.

To set up the physical model, the subdomain (material properties) and boundary conditions need to be set. Two perfect matching layers (PMLs) are used on the top and bottom sides of the unit cell to represent the much thicker air superstrate and glass substrate. Two ports are used for calculating the scattering coefficients of the structure, with Port #1 act as the light source by generating plane waves as well.

The refractive indices of the corresponding materials are taken as the subdomain conditions. For all the OPV designs, complex refractive indices ($n - i \cdot k$) are used in the FEM simulations for Ag and P3HT:PCBM (1:1), as shown in Fig. 3.3 (b) and (c), respectively. The refractive indices of P3HT:PCBM are taken from Ref. [70]. Refractive indices of Ag are taken from Ref. [27]. All the other materials used are treated as lossless dielectric materials. Glass with refractive index of 1.46 is used as the substrate. The refractive index of MoO_3 and ITO are taken from Ref. [71]and [72], respectively. Even though there will be certain absorption losses in the ITO/MoO_3 electrode at the light incident side in the real OPV devices, treating ITO and MoO_3 as lossless will not affect the relative comparisons between the OPV designs in Fig. 3.1. This is because the structures in Fig. 3.1 (a) and (b) have the same ITO and MoO_3 thicknesses and thus similar absorption loss in the anode. Besides, MoO_3 with a bandgap of 2.9 eV only absorbs light with wavelengths shorter than 428 nm, which only possess a small portion of the solar power covered by the absorbing wavelength spectrum of the P3HT:PCBM blend.

A normal incident plane wave propagating in the (+) z-direction is assumed to be the light source. Two types of plane waves were simulated: TM waves with E_x perpendicular to the grating lines and TE waves with E_y parallel to the grating lines, as shown in Fig. 3.4. As discussed in Section 2.1 that both the momentum match and the presence of longitudinal (x direction in Fig. 3.4) electric field are required for the excitation of surface plasmon resonances. The grating will be able to change the x-

direction momentum component. As a result, TM waves with strong E_x will generate SPPs along the P3HT:PCBM/Ag grating interface. For TE waves, the grating will still change the momentum of the incident light though SPPs along x direction cannot be efficiently excited. I found that with proper design of the grating geometry, diffracted TE waves can be coupled to waveguide modes inside the OPV. Both SPP and waveguide mode excitation will benefit the light absorption due to the increased light path along the x direction.

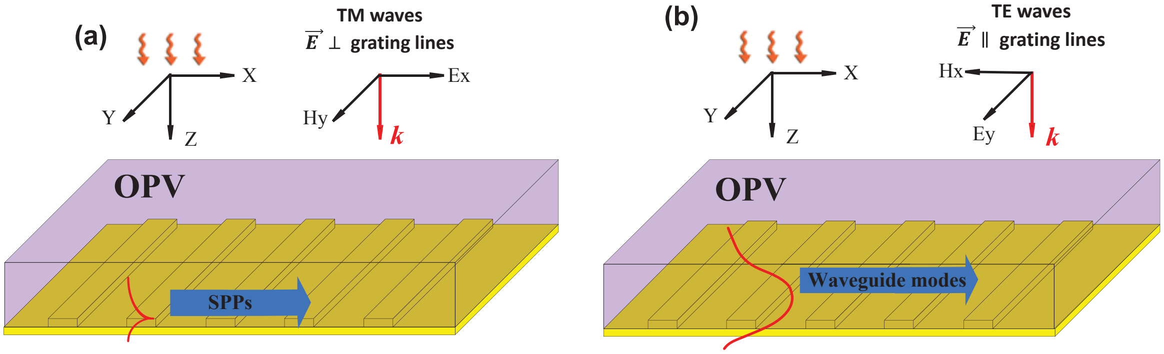

Fig. 3.4 Illustration of incident TM and TE waves and the corresponding light absorption enhancement schemes from (a) SPP excitation for TM and (b) waveguide mode coupling for TE, respectively. The light path for both TM and TE waves are greatly enhanced.

Then, the electromagnetic fields within the OPV were numerically calculated. The absorption spectrum can be obtained by calculating the scattering coefficients of the solar cell using Port #1 and #2, *i.e.* reflection and transmission coefficients, while varying the wavelength of the incident light. By calculating the resistive heating in all the absorbing materials (Ag and P3HT:PCBM), we can evaluate how much light is absorbed in the P3HT:PCBM active layer. Only this part of light absorption contributes to the current generation of the solar cell. The short-circuit current density J_{SC} (mA/cm^2) was calculated by first estimating the absorption by the P3HT:PCBM layer $A(\lambda_0)$ which exclusively contributes to the photocurrent generation and then performing the integration.

$$J_{SC} = q \cdot \int A(\lambda_0) \cdot \Phi(\lambda_0) d\lambda_0 \tag{3.1}$$

where q is the unit charge and $\Phi(\lambda_o)$ is the AM 1.5G solar flux ($s^{-1}cm^{-2}$). The integration was done for the wavelength range of 280 ~ 800 nm which is enough to cover the absorbing wavelengths of the P3HT:PCBM (1:1 weight ratio).

We also obtained J_{sco} from a control PV structure as shown in Fig. 3.1 (a) and defined the enhancement factor EF as J_{SC} / J_{SCO}. Considering the unpolarized nature of sunlight, we set $EF = (EF_{TM} + EF_{TE})/2$. With the photocurrent J_{sc} as a performance indicator, I optimized the grating design through rigorous parametric study for higher optical absorption, including the grating height h, pitch Λ, and the duty circle D, which is defined as the ratio between the ridge width and the pitch (W/Λ).

3.3 Effect of the grating height on the absorption enhancement

First of all, the ITO thickness in the reference structure in Fig. 3.1 (a) is optimized in the range of 80 ~ 250 nm for best anti-reflection performance to achieve the highest J_{sc}. The polymer layer thickness is assumed to be d_p = 200 nm. The optimized ITO thicknesses is 120 nm, leading to a current density of J_{sc} = 14.49 mA/cm^2 for both TE and TM waves. The ITO thickness in the OPV with the grating back reflector in Fig. 3.1 (b) is also set at 120 nm.

Preliminary simulations were performed to set the grating height h. Several combinations of grating pitches and duty cycles are used. For each data set, the grating height h is varied between 10% ~ 60% of the polymer thickness (d_p = 200 nm), while the top surface of the polymer layer is assumed to be flat for simplification of the simulations. To take into account the decrease of the actual volume of the P3HT:PCBM film when the grating height is increased, the *EF* is normalized by the P3HT:PCBM volume with the P3HT:PCBM volume in Fig. 3.1 (a) as the unit volume. The *EF* results for TM waves are plotted in Fig. 3.5 with respect to the relative height of the grating defined as h/d_p.

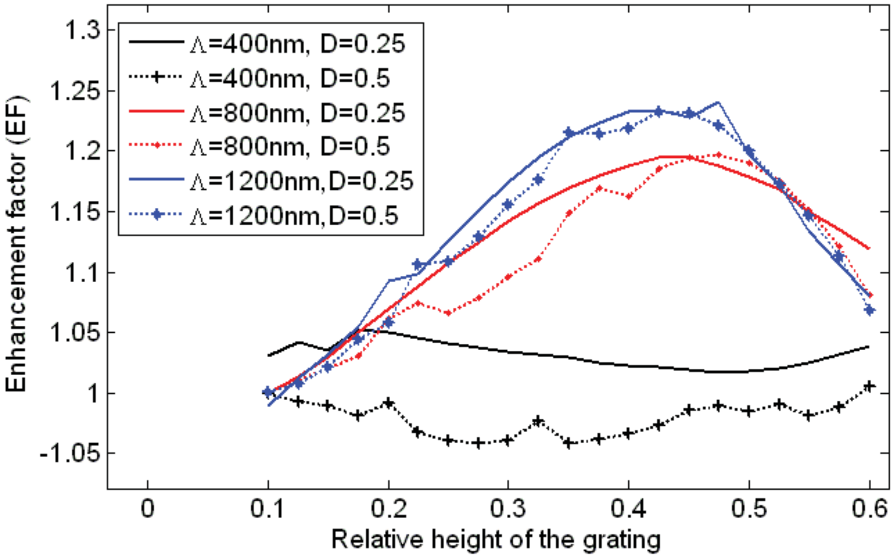

Fig. 3.5 Effect of the grating height on EF in $\boldsymbol{J_{sc}}$ for different combinations of **Λ** and ***D***, which shows increase EF for larger grating height until it reaches the maxima and starts to decrease due to the reduced active layer.

For four grating designs out of six in Fig. 3.5, there is a common trend that with larger *h*, the *EF* becomes higher. As *h* increases beyond a certain point, J_{sc} starts to decrease. Though when Λ = 400 nm, no obvious enhancement in J_{sc} was seen for both *D* = 0.25 or 0.5. Similar results were obtained from TE modes, *i.e.* higher enhancements were obtained with larger *h* for both TE and TM modes. However, making conformal spin-coated polymer layers is difficult on surfaces with deep features. As a compromise between ease of subsequent OPV layer deposition and *EF*, I chose the grating height to be

50 nm, 25% of the polymer layer thickness, which is still able to induce more than 10% of enhancement in J_{sc}.

3.4 Enhancement of TM absorption

The impacts of Λ and the duty-cycle D on EF_{TM} are investigated for Λ from 600 to 1300 nm and D from 0.2 to 0.7, respectively. The result is plotted in Fig. 3.6 (a). The peak EF_{TM} value of 1.22 was obtained at $\Lambda = 1040$ nm and $D = 0.36$. In fact, for $\Lambda > 700$ nm, there is a narrow range of D (0.35~0.45) in which the EF_{TM} values are abruptly raised from the surrounding level. This indicates that EF_{TM} has stronger dependence on the duty cycle than on the grating pitch. Figure 3.6 (b) shows a 3D-rendered plot of EF_{TM} within the dotted box of Fig. 3.6 (a), confirming the existence of high EF_{TM} band.

The origin of this high *EF* band was revealed by plotting the absorption spectrum (red curve) and comparing it to that from the reference device, as shown in Fig. 3.7 (a). The structural parameters of the grating were set to induce maximum EF_{TM} ($D = 0.36$, $\Lambda =$ 1040 nm). For comparison, the absorption spectrum from the reference device without gratings is also added (green curve). The absorption spectrum of OPVs with the optimized grating design exhibits multiple peaks within the long-λ_o regime ($\lambda_o > 650$ nm), which is rich in solar energy but poorly absorbed by many OPV materials [70, 73], while the reference spectrum (green curve) is devoid of such peaks within the regime. The appearance of those absorption peaks is common within the high EF_{TM} band. The absorption spectrum of OPVs with the grating structural parameters outside of the high EF_{TM} band ($D = 0.5$ for instance) were also superimposed in Fig. 3.7 (a) in black dashed line. Outside the band, the plasmonic absorption peaks become much lower.

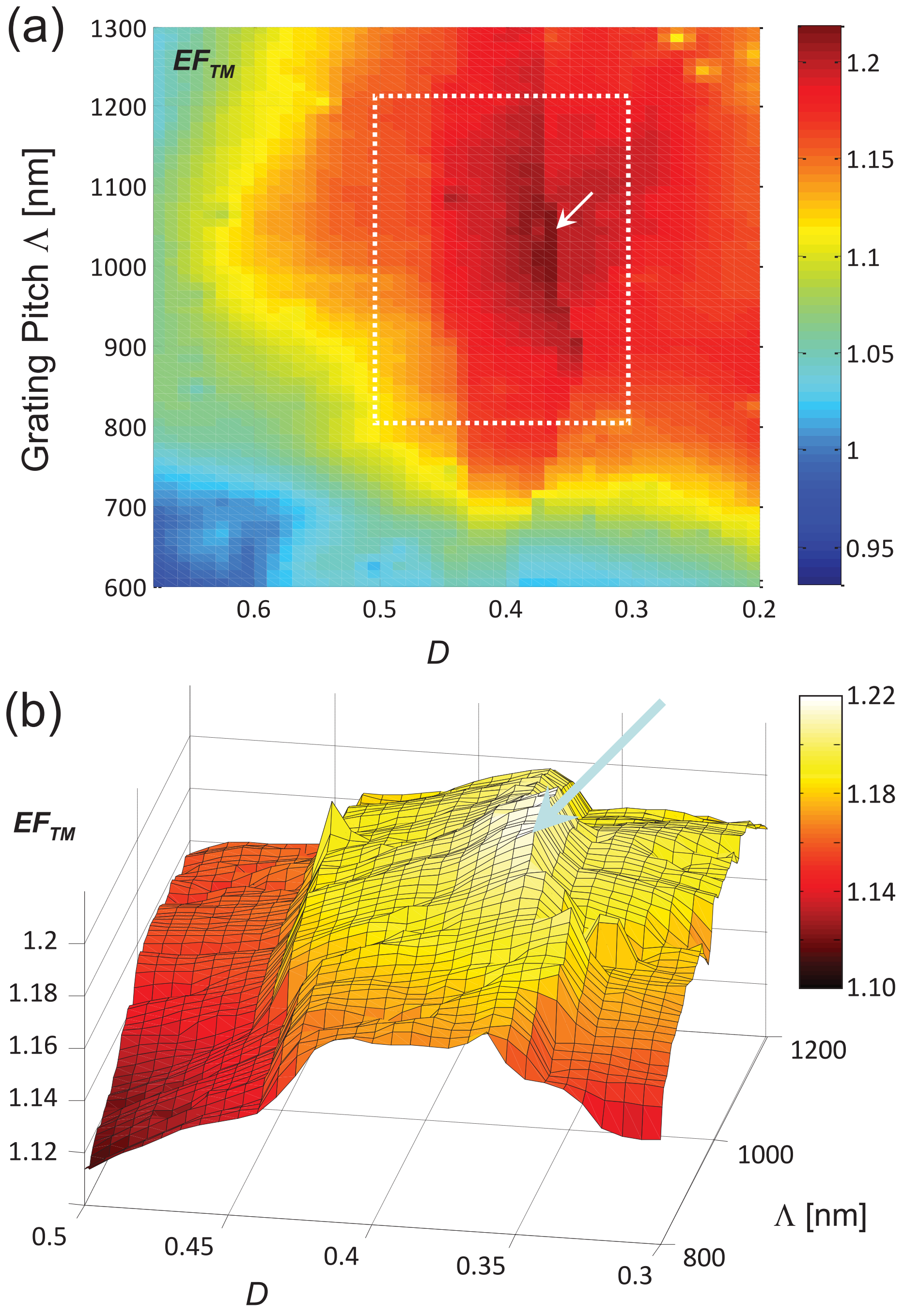

Fig. 3.6 (a) A 2D plot of EF_{TM} as a function of the grating duty-cycle D and the grating pitch Λ. EF_{TM} exhibits a stronger dependence on D. (b) EF_{TM} corresponding to the region within the dotted box of (a) is plotted in 3D for a clearer view of the high EF_{TM} band within $0.35 < D < 0.45$. The arrows indicate the maximum EF_{TM} point in both plots.

The absorption spectra in Fig. 3.7 (b), obtained near the edge of the high EF_{TM} band (Λ = 950 nm, D = 0.35) also exhibit a similar trend. When D = 0.35, the overall absorption is greatly enhanced due to the formation of the three peaks. The peaks become much lower for D = 0.5, which is outside the high EF_{TM} band.

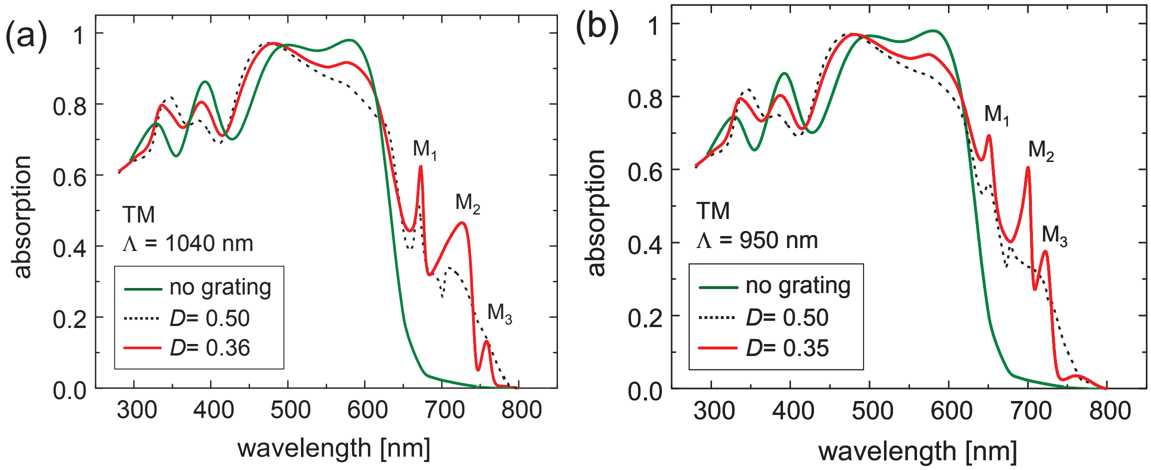

Fig. 3.7 (a) Comparisons between absorption spectra of different OPVs: with the optimized grating design (red curve), without grating (green curve) and with a grating whose structural parameters are outside the high EF_{TM} band (black dashed curve). (b) Another set of absorption spectra exhibit the same trend. In both plots, the absorption enhancement comes from the formation of three absorption peaks for $\lambda_o > 650$ nm near D = 0.35

The electric field patterns obtained at absorption peaks M_1, M_2, and M_3 of Fig. 3.7 (a) (λ_o = 672, 730, and 760 nm, respectively) and plotted in Fig. 3.8 (a), (b), and (c), respectively, clearly reveal their electromagnetic origins. M_1 represents the FP resonance of the in-plane SPPs on the top surface of the grating ridge aided by the reflections at the edges of the ridge. On the other hand, M_3 is from the FP resonance of the in-plane SPPs confined within the grooves between the ridges due to reflections at the ridge walls. It is worth noting that M_2 actually represents a combination of two FP resonances formed simultaneously on the ridge and groove surfaces. The strong fields at the ridge corners indicate that the sharp corners of the grating function as the launching pad to convert the incoming light into the in-plane SPPs in all three cases.

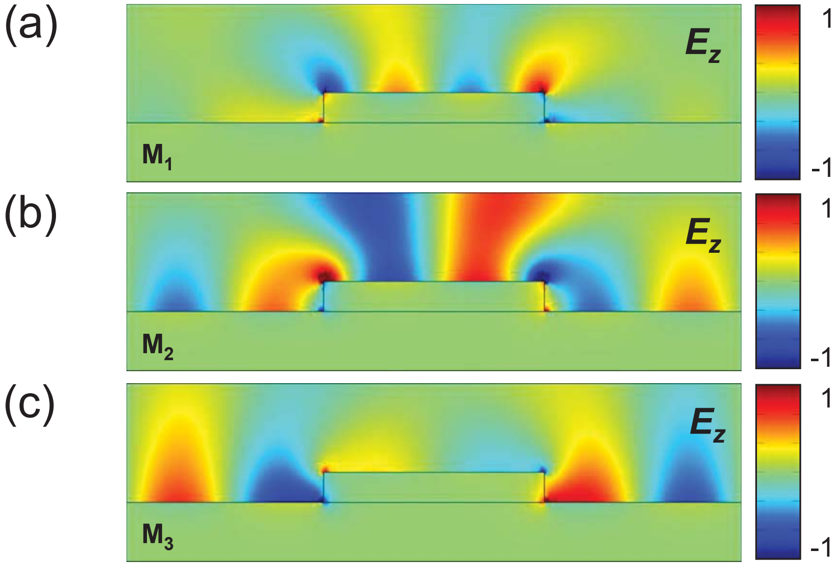

Fig. 3.8 Normalized field patterns of E_z obtained at the absorption peaks of M_1, M_2, and M_3 in Fig. 3.7 (a). At M_1, the main lateral plasmonic FP resonance occurs only on the top surface of the grating ridge. On the other hand, it occurs only within the groove surrounded by the ridge walls at M_3. At the intermediate point of M_2, the plasmonic resonance covers both the ridge and groove surfaces.

From Figs. 3.7 (a) and (b), it is clear that EF_{TM} is maximized when all three of these FP resonances are induced within the long-λ_o regime. Since the importance of D in maximizing EF_{TM} was already shown in Figs. 3.6 (a) and (b), I try to quantify its impact by plotting the absorption spectrum in the long-λ_o regime as a function of D. Figure 3.9 (a) shows the absorption spectrum when the grating pitch is fixed at $\Lambda = 1040$ nm and the duty cycle D is varied between 0.2 ~ 0.7, to show the changes in the absorption peaks M_1,

M_2, and M_3 around the optimum D value of 0.36. All three absorption peaks depend strongly on D which, in turn, determines the FP cavity length L between the reflecting structures.

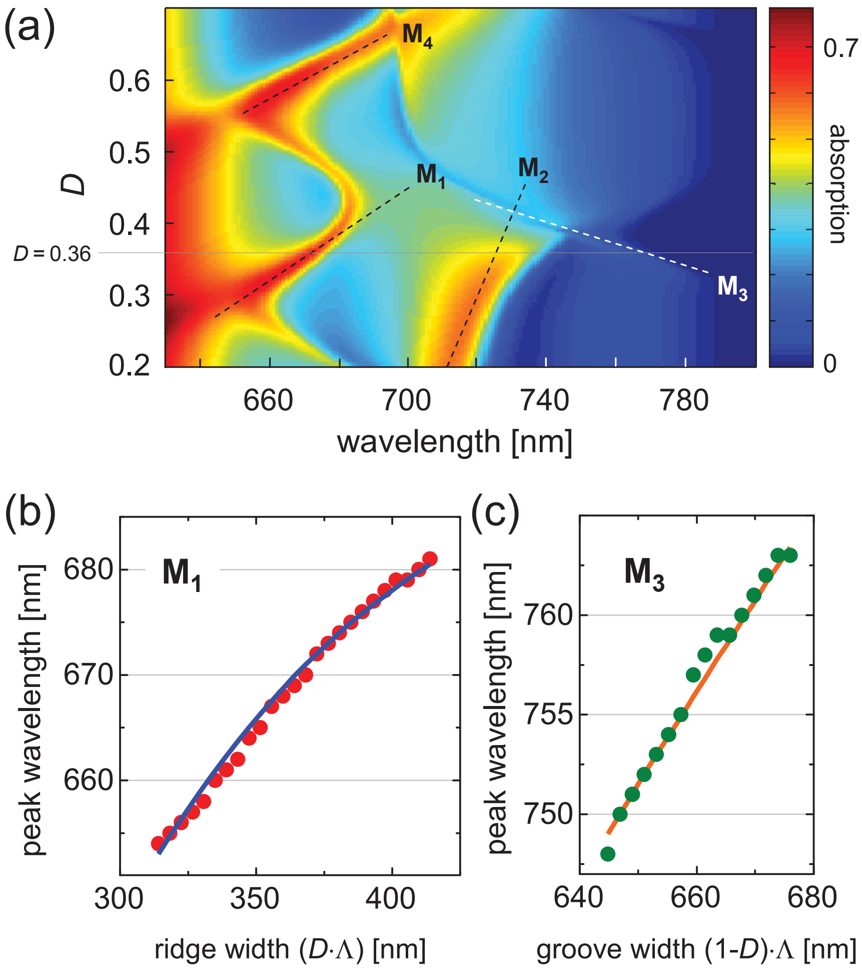

Fig. 3.9 (a) The absorption spectrum for Λ = 1040 nm as a function of D. The absorption peaks M_1, M_2, and M_3 depend strongly on D. The maximum EF_{TM} was achieved at D = 0.36 when three of the absorption peaks are at their greatest widths. The dots in (b) and (c) show the changes in the peak wavelength of the plasmonic FP resonance as a function of the width of the resonators, *i.e.*, the ridge and the groove, respectively. The curve-fit results based on Eq. (3.2) (solid lines) agree well with the simulation results (dots).

Fig. 3.9 (a) also clearly indicates that the high EF_{TM} band at $0.35 < D < 0.45$ indeed corresponds to the range supporting all three of them simultaneously. The maximum EF_{TM} was achieved at a D value along which all three of the absorption peaks are included at their greatest widths. Beyond the point, the combined FP resonance of M2 disappears and M1 and M3 become weaker. Even though a higher order FP resonance, *i.e.*, M4, appears on the top of the ridge as it becomes wider ($D > 0.55$), it is not accompanied by other FP resonances and results in low EF_{TM}.

For further optimization of EF_{TM}, it is necessary to establish a model to predict λ_{FP}, the wavelength of lateral FP resonance. Previous studies showed that it can be accomplished using the FP resonance condition

$$2\pi \cdot n_{SPP} \cdot L / \lambda_{\mathrm{FP}} = m \cdot \pi + \varphi, \tag{3.2}$$

where n_{SPP} is the effective index of the SPP, L the resonator length, and φ the phase change due to the SPP reflection at the resonator edge [74-76]. Since a theoretical framework for calculating φ in a variety of SPP resonator geometries has not been established yet, it must be retrieved by curve-fitting simulation or experimental observations to Eq. (3.2). For example, Ref. [75] shows that φ changes linearly with λ_o in the case of nanostrip resonators.

Since this φ–λ_o relation is important in finding the optimal D value which enables FP resonances on the top and groove surfaces simultaneously, I tried to find it from the simulation results. In the OPV configuration, $n_{SPP} = (\varepsilon_{\mathrm{Ag}} \cdot \varepsilon_{\mathrm{OPV}} / (\varepsilon_{\mathrm{Ag}} + \varepsilon_{\mathrm{OPV}}))^{1/2}$ and the resonator lengths are $L = D \cdot \Lambda$ for M_1 and $(1\text{-}D) \cdot \Lambda$ for M_3, respectively. For M_1, φ is calculated for λ_o increases from 655 nm to 685 nm, which corresponds to the change in the duty cycle from 28.9% to 43.3%. For M_3, the calculation is done for λ_o increases from 750 nm to 765 nm, which corresponds to the change in the duty cycle from 38.5% to 34.6%. The best curve-fitting results for M_1 and M_3 were obtained by assuming that the values of φ vary linearly from -53.1° to -142.2° as λ_o increases from 655 nm to 685 nm for M_1 and from -148.5° to -133.4° as λ_o increases from 750 nm to 765 nm for M_3. The fitting results are shown in Figs. 5(b) and (c), respectively. This indicates that the SPP mode reflected from the walls and edges of the grating ridge also undergoes phase changes with linear λ_o-dependence. Note that the values of φ due to the reflection from the ridge walls exhibits much lower λ_o-dependence than the one due to the edge reflection.

3.5 Enhancement of TE absorption

The metallic grating can also enhance the absorption of TE-polarized light, which induces little plasmonic activity, by coupling it into the guided modes propagating along the thin PV layer [9, 61, 77, 78]. We find that in the case of the long-pitch grating, the ranges of Λ and D for high-level EF_{TE} overlaps the high EF_{TM} band, enabling polarization-diverse absorption enhancement. D again plays an important role in obtaining a high EF_{TE}.

Figure 3.10 (a) shows EF_{TE} as a function of Λ and D. Like the TM result in Fig. 3.6 (a), the high EF_{TE} region forms a band delineated by $0.43 < D < 0.53$ and $\Lambda > 800$ nm. It is worth noting that EF_{TE} maximizes at D slightly lower than 0.5, a frequent choice in literature, due largely to the competition between the grating's diffraction efficiency, which increases as D approaches 0.5, and the OPV layer volume, which decreases with increasing D. Regardless of the origin, the feasibility of obtaining high EF_{TE} levels at $D <$

0.5 helps achieving polarization-diverse enhancement since the high EF_{TM} band was formed in that regime.

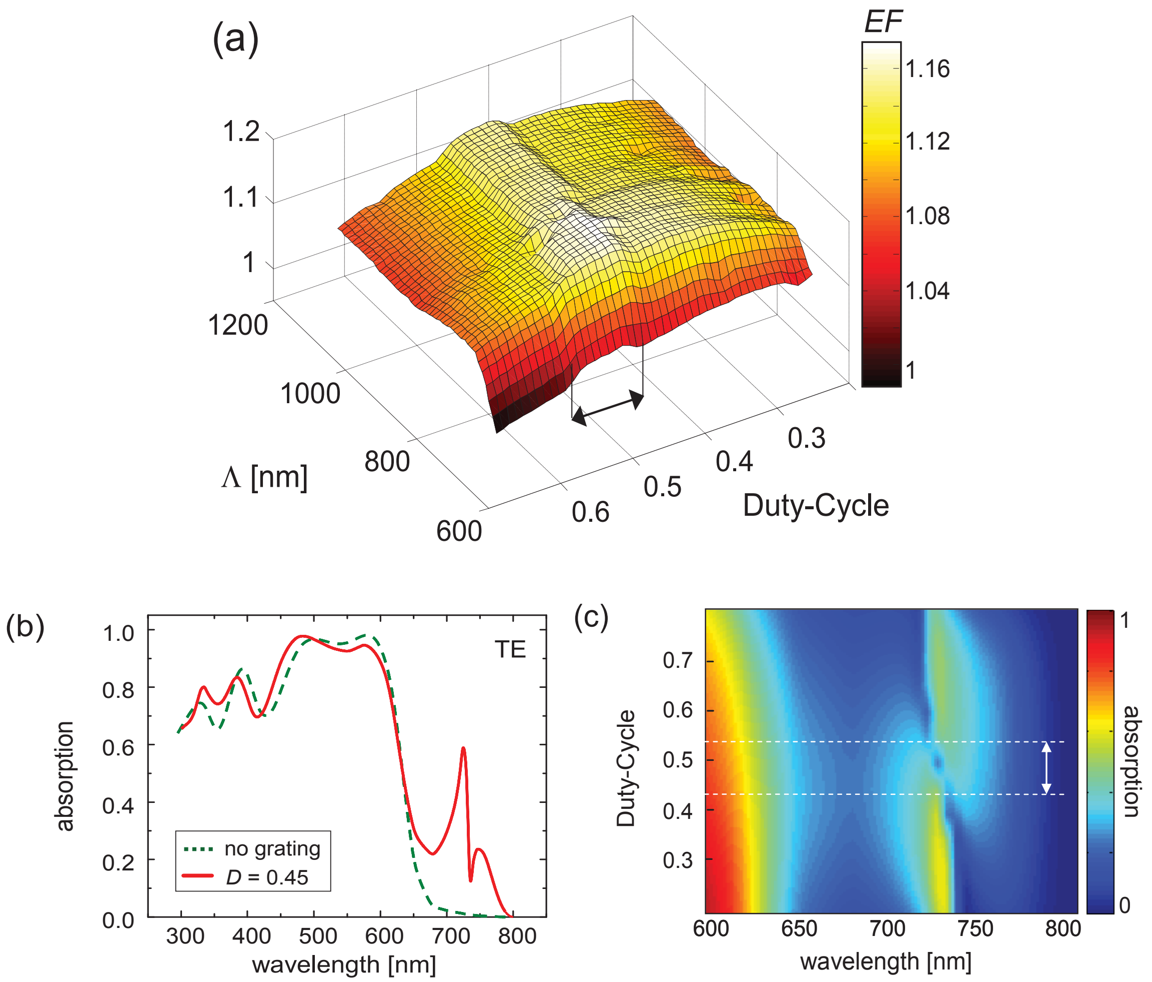

Fig. 3.10 (a) A 3D plot of EF_{TE} as a function of D and Λ. For $\Lambda > 800$ nm, EF_{TE} also forms a narrow band within $0.43 < D < 0.53$. (b) The absorption spectrum obtained at the maximum EF_{TE} point ($D = 0.45$, $\Lambda = 850$ nm), showing a absorption peak between 700 ~ 800 nm. (c) A 2D plot of the absorption as a function of D and Λ. The two dotted lines indicate the high EF_{TE} band of (a) within which the absorption peak near $\lambda_o = 725$ nm becomes widest.

EF_{TE} maximizes to ~1.17 near D = 0.45 with Λ = 850 nm. The corresponding absorption spectrum is shown in Fig. 3.10 (b). Similarly to Fig. 3.7, the formation of an absorption peak is responsible for the overall improvement in the TE absorption. We attributed the narrow dip in the absorption peak to the guided mode resonance (GMR) which occurs when the grating begins to function as a distributed Bragg reflector to the guided mode, forcing it to escape the grating-waveguide composite structure [79, 80]. On the other hand, the guided modes at wavelengths close to this GMR dip are highly enhanced through the lateral FP resonance [81].

The absorption spectrum as a function of D is shown in Fig. 3.10 (c). It shows that the absorption peak near λ_o = 725 nm becomes widest within the high EF_{TE} band. This indicates that EF_{TE} can be maximized by placing the absorption peak within the long-λ_o regime and fine-tuning its width through D while ensuring the formation of GMR.

The spectral position and span of the TE absorption peak can be estimated using the guided mode excitation condition. Figure 3.11 (a) shows that the grating redirects the normally incident light into the waveguide core, which includes the OPV, MoO_3, and ITO layers as shown in the inset, either through a single diffraction (order m_1 and diffraction angle θ_1) or by involving a subsequent diffraction (m_2 and θ_2). In any case, the final incidence angle at the air-ITO interface θ_2 must be greater than $\theta_C = \mathrm{asin}(n_{air} / n_{ITO})$ to form a guided mode. It is straightforward to show that

$$\theta_2 = \mathrm{asin}((m_1 + m_2) \cdot \lambda_o / (n_{WG} \Lambda)) \tag{3.3}$$

where n_{WG} is the refractive index experienced by the light to be diffracted. Since the waveguide core thickness is a fraction of λ_o, we set the average value of n_{OPV}, n_{MoO3}, and n_{ITO} as n_{WG}. The plot of θ_2 in Fig. 3.11 (b) shows that $\theta_2 > \theta_C$ for $\lambda_o < 800$ nm when $m_1 + m_2 = 2$, which agrees well with the upper limit of the absorption peak's spectral span in Fig. 3.10 (b) and (c). The use of long-pitch gratings, whose diffraction orders are formed over a wide range of diffraction angles with a smaller angle increment than those of short-pitch gratings, turns out to be beneficial in exciting guided modes and exploiting the GMR. Neither the guided mode excitation condition nor Fig. 3.11(b), however, gives explicit information on the lower limit or the GMR wavelength. Their estimations rely on numerical simulations.

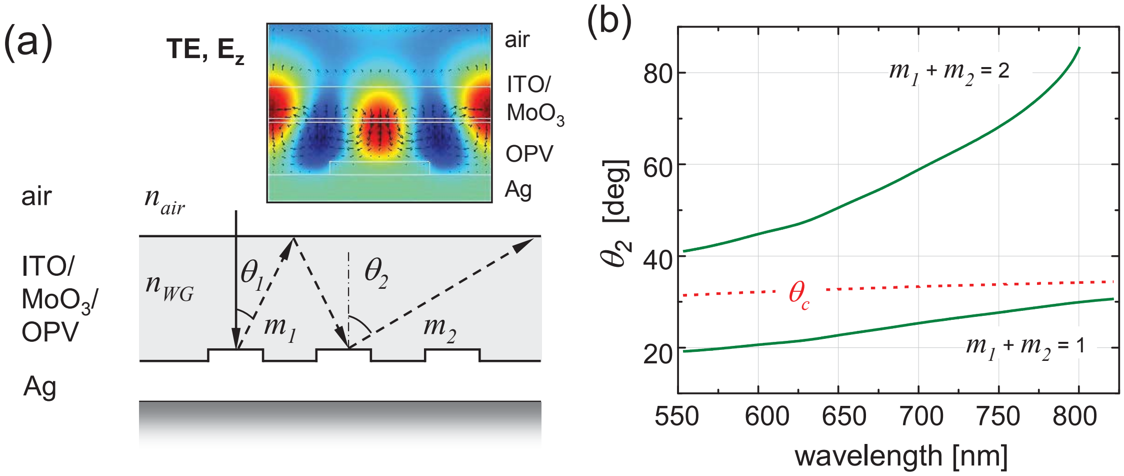

Fig. 3.11 (a) A schematic diagram for the grating-based guided mode excitation scheme. The inset shows the E_z field pattern of one guided mode, confirming that the ITO/MoO$_3$/OPV layers functions as the waveguide in combination. (b) The final diffraction angle θ_2 is plotted as a function of wavelength based on Eq. (3.3). θ_c indicates the critical angle at the waveguide/air interface which must be exceeded for waveguiding.

3.6 Combining TM and TE absorption enhancements

Since sunlight is unpolarized, the practical level of enhancement is determined by $EF = (EF_{TM} + EF_{TE})/2$. The overall enhancement factor EF is plotted in Fig. 3.12 (a) as a function of Λ and D. For comparison, EF_{TM} and EF_{TE} are also plotted in Fig. 3.12 (b) and (c), respectively. The coloring scale is chosen to emphasize the existence of high EF_{TM} and EF_{TE} bands identified previously. Figure 3.12 (a) clearly shows that EF retains the salient features of EF_{TM} and EF_{TE}. There are two narrow regions of strong EF improvement for $\Lambda > 900$ nm: one along the $D = 0.43$ horizontal line which corresponds to the overlap between high EF_{TM} and EF_{TE} bands and the other along the lower edge of the high EF_{TM} band ($D = 0.36$) which includes the highest points of the band as shown in Fig. 3.6 (b). Between the two narrow high EF bands, the EF value is mainly determined by EF_{TM}, indicating that the plasmonic scheme leads to a higher absorption enhancement than the one based on guided mode excitation.

EF values between 1.17 ~ 1.18 are obtained for $900 < \Lambda < 1150$ nm in Fig. 3.12 (a). This indicates that a polarization-diverse absorption enhancement can be achieved over a wide range of Λ in the long-pitch regime, also suggesting a high degree of freedom in grating design and tolerance to imperfections in grating fabrication.

We also performed parameter tolerance studies on the structure optimized above ($\Lambda = 1100$ nm, $D = 0.36$). We focused mainly on the thickness and the real part of the refractive index of the OPV layer which directly affect the resonance conditions in both TM and TE cases. In this study, we assumed ±5% maximum deviations from the original design values. The resulting changes in EF are summarized in Table 3.1. The results indicate that the maximum change due to a ±5% deviation is less than 4.5%, which can be attributed to shifts of the resonance peaks and is well within the allowable range in practice.

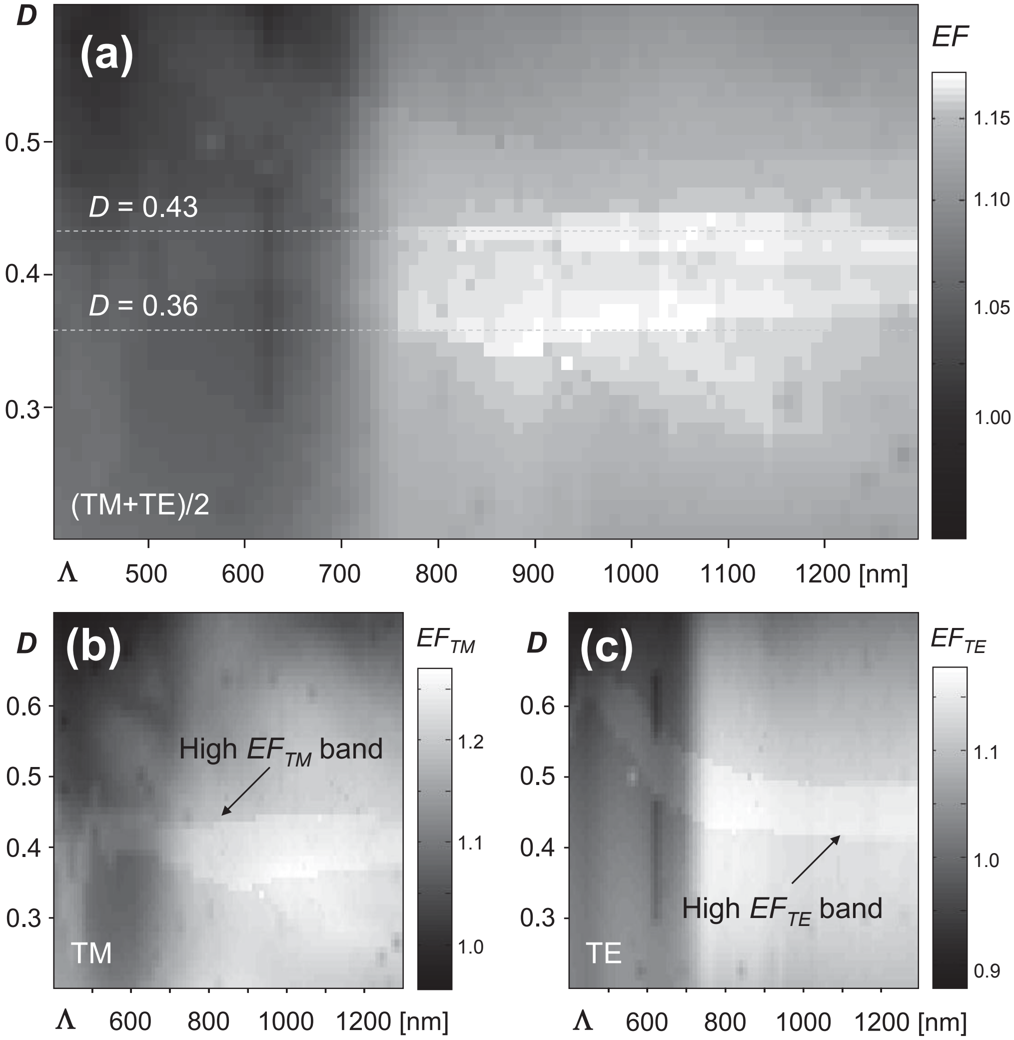

Fig. 3.12 (a) For unpolarized light, *EF* retains all the salient features of EF_{TM} and EF_{TE} shown in (b) and (c), respectively. There are two major regions of high *EF*: one near the overlap of high EF_{TM} and EF_{TE} bands ($D \sim 0.43$), the other near the lower edge of the high EF_{TM} band ($D \sim 0.36$).

Table 3.1 The changes in EF due to ±5% deviations in the OPV layer thickness and the real part of its refractive index.

Tolerance study on	Scale Factor	EF_{TM}	EF_{TE}
OPV thickness	0.95	1.24	1.18
	1.0	1.22	1.13
	1.05	1.19	1.13
Real part of P3HT:PCBM refractive index	0.95	1.23	1.14
	1.0	1.22	1.13
	1.05	1.19	1.14

In conclusion, the absorption enhancement effect in P3HT:PCBM OPVs is investigated on metallic gratings whose pitch Λ is 800~1200 nm. I found that the long pitch grating helped enabling simultaneous enhance absorption for both TM and TE waves, in the long-wavelength regime ($\lambda_o > 650$ nm). EF_{TM}, the enhancement factor for the TM portion of the incoming light, can be as high as 1.22 through the excitation of laterally propagating in-plane SPP modes and their lateral Fabry-Perot resonances. The grating's duty cycle D turned out to play an important role in maximizing EF_{TM}. A judicious choice of D could enable simultaneous formations of the lateral FP resonances on both the ridge and groove surfaces, leading to a substantial increase in EF_{TM}. The long-pitch grating also enhanced the absorption of the TE portion of sunlight, which induces little plasmonic effect, through the excitation of guided modes along the OPV/MoO_3/ITO composite waveguiding layer. D again played an important role in this process as the dominant factor for determining the diffraction efficiency. We could make a substantial overlap between the ranges of D and Λ for these two enhancement effects, leading to a polarization-diverse absorption enhancement. For unpolarized sunlight, our estimated overall *EF* is 1.17 ~ 1.18 obtained with $900 < \Lambda < 1150$ nm and $0.36 < D < 0.43$.

Chapter 4. Experimental methodology

4.1 Grating Fabrication

To incorporate the plasmonic effect into the OPV as shown in Fig. 3.2, one needs to make nanostructures on the planar Ag layer first. The grating fabrication was done with electron beam lithography (EBL) from Raith in Microelectronic Research Center or a laser interference lithography system setup with a HeCd laser (325 nm) in Microphotonics/Biophotonics Laboratory, together with a lift-off process to transfer the photoresist patterns to Ag patterns.

For both EBL and laser interference lithography, different photoresists are used. The principal components of photoresists are the base resin, sensitizer and solvent. The solvent is used to allow spin coating of the photoresist in solution form and the formation of thin photoresist layers on the substrates. Upon the exposure to radiation (X-ray, electron beam, UV light, etc.), the polymer changes its structure, and the sensitizer controls the chemical reactions in the polymeric phase [82]. Depending on the changes in the polymer structure, photoresists are categorized into positive and negative ones. A positive photoresist is weakened upon exposure due to the rupture of its main and side chains and it becomes more soluble in the developing solution. Exposure of a negative photoresist strengthens it by cross-linking its main chains or side chains, resulting in lower solubility than usual in the developing solution [82]. As a result, for a positive photoresist, the exposed region is washed away by the developer; while for a negative photoresist, the exposed region is resistant to the developing solution and the unexposed region is washed away, as shown in Fig. 4.1 [83].

The photoresists and the comparisons between EBL and interference lithography for the application of plasmonic gratings in OPVs are summarized in Table 4.1.

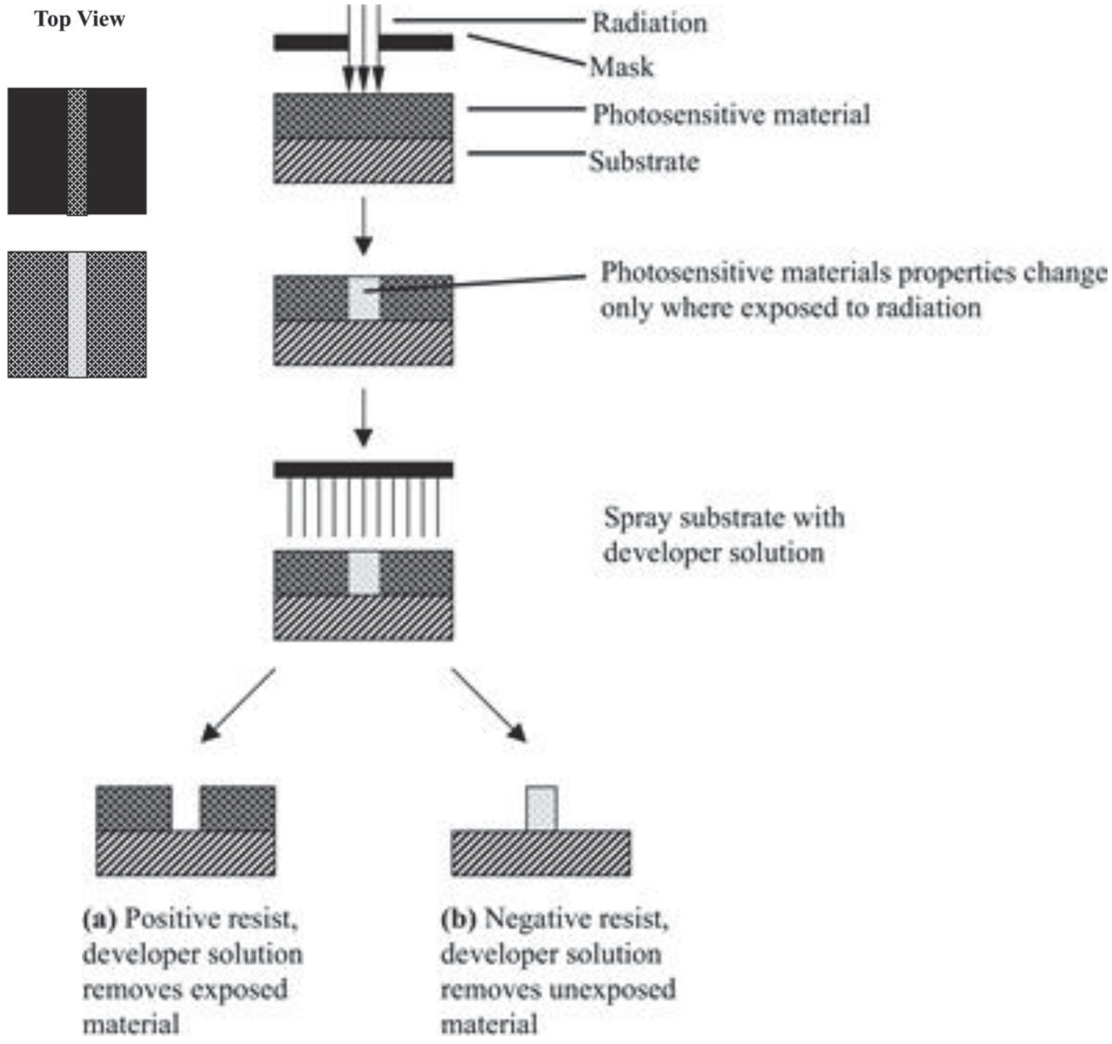

Fig. 4.1 Different pattern definitions in (a) a positive photoresist and (b) a negative photoresist transferred from the same original pattern, which is a shadow mask in this example. (from Ref. [83])

Table 4.1 Comparisons between EBL and inteferometric lithography

	e-beam lithography	Laser interference lithography
Resolution	less than 20 nm	half the laser wavelength
Photoresist	Positive photoresist PMMA (~ 100 nm)	Negative photoresist SU-8, ma-N405 (0.5 ~ 2 um)
Process time	~ 40 min for (800 um)^2	~ 30 sec for 1 inch square
Advantage	Gratings of different geometries can be made on the same substrate for better comparisons.	Fast and large area exposures, suitable for preparing nanostructures for solar cell integration.

4.1.1 Grating Fabrication with EBL

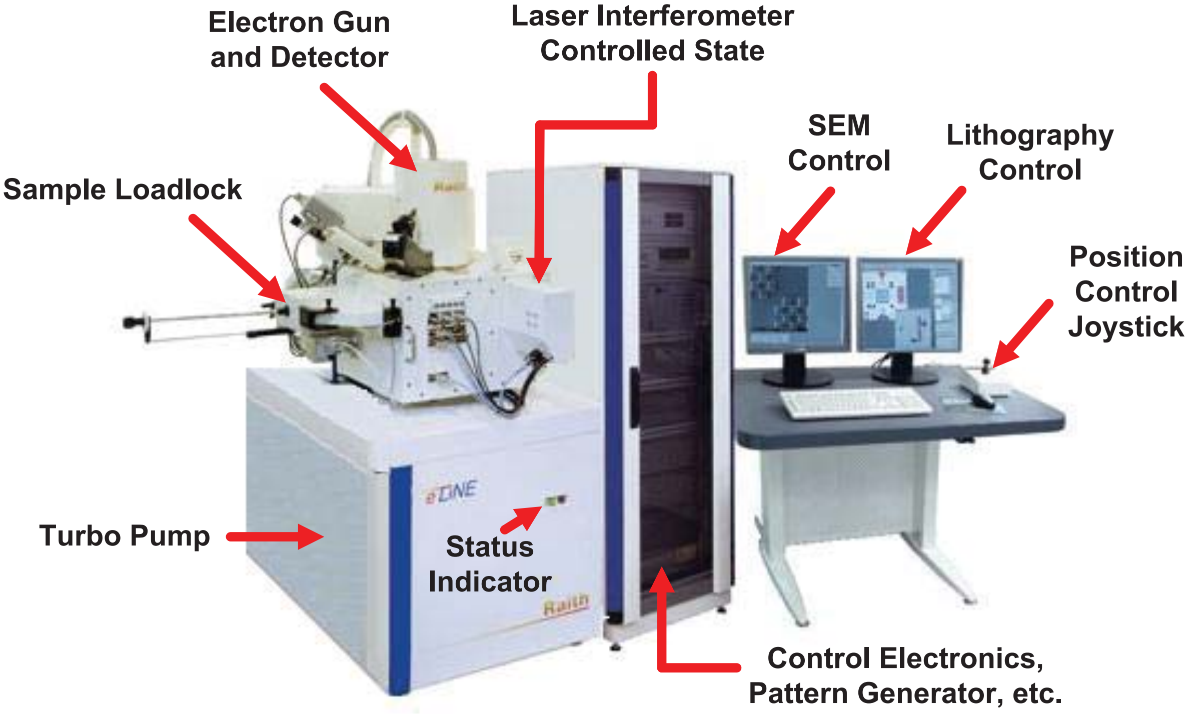

Fig. 4.2 A picture of the EBL system (eLiNE from Raith GmbH) with major components marked.

The EBL system is shown in Fig. 4.2, with the major components marked. As a mask-less lithography technique, the exposure of desired patterns/areas is achieved by using an electron beam with a small spot size (< 20 nm) and moving the sample stage with an electronic controller as well as deflecting the electron beam with electromagnetic lens. The pattern design is done with GDSII editor and the stage control and electron beam exposure are done with e-LiNE, a software developed by Raith.

The fabrication of photoresist gratings and the lift-off process as the pattern transferring scheme from photoresist to metallic structures are shown in Fig. 4.3 (a).

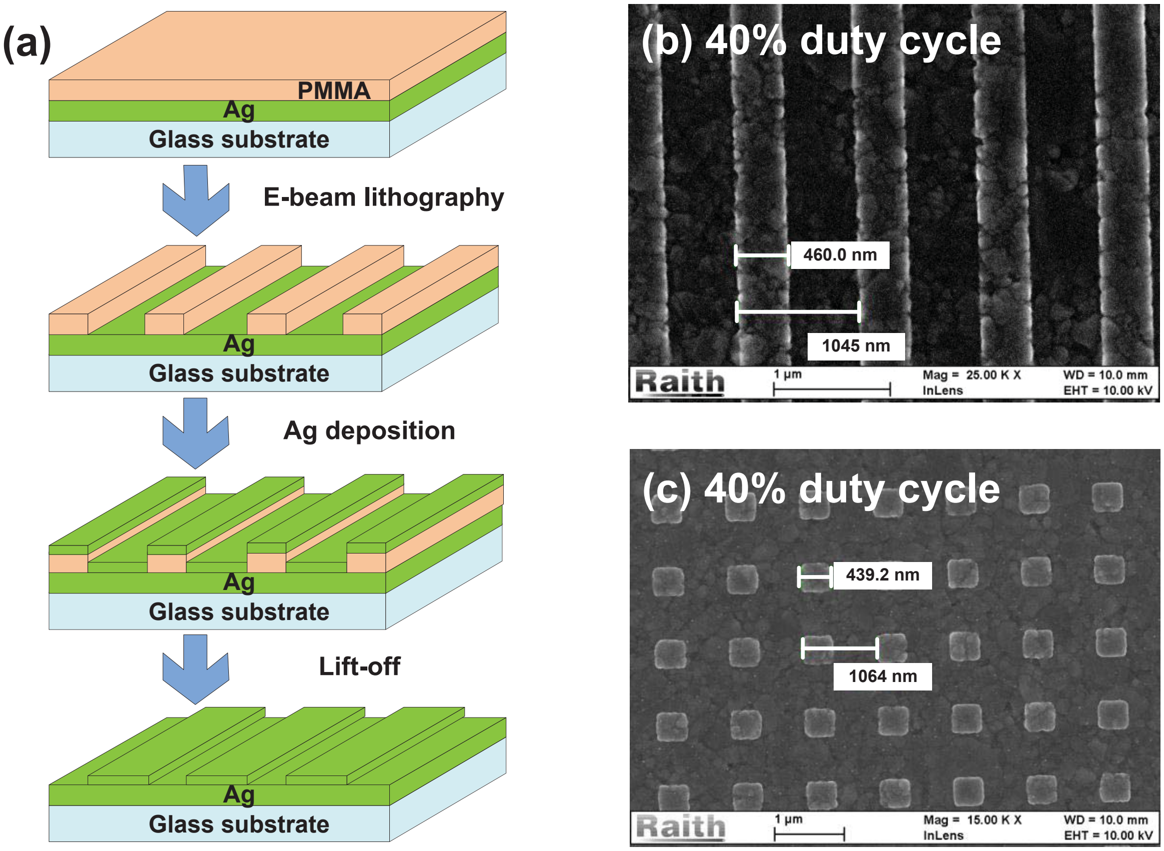

Fig. 4.3 Plasmonic Ag structures fabricated by e-beam lithography: (a) - (b) are 1D metallic gratings and (c) - (d) are 2D structures with different duty cycles. Major steps of the fabrication are also shown on the left.

The EBL process starts with a uniform PMMA photoresist layer on a Ag coated glass substrate. A glass slide is firstly cleaned in ultrasonic baths of surfactants for 15min, water for 4 times and each 5min, followed by iso-propanol (IPA), acetone and another IPA baths each 5min. Then a 100 nm Ag layer is thermally evaporated on to the substrate with a evaporation rate of less than 3 Å/sec. 2% 950 PMMA in anisole solution from MicroChem is used as the electron beam photoresist. The PMMA is first spin coated on the substrate at 1500 rpm for 45 sec and then annealed at 180°C for 2 min in the ambient, which leads to a ~ 100 nm uniform layer.

Photoresist gratings are formed by first selectively expose the PMMA layer to a controlled amount of electron beam (electron dose) and then develop the exposed area with a suitable developer, which was 1:3 MIBK (Methyl isobutyl ketone):IPA from MicroChem. A second Ag evaporation is done on top of the patterned PMMA layer and the final Ag plasmonic structure can be formed by lifting-off the PMMA together with the Ag on top of it. The lift-off process was done with in baths of Remover PG, which was from MicroChem with the main content of N-Methyl Pyrrolidinone (>99%). All the Remover PG baths are done at 80°C, which is below its boiling point of 202°C, with a hot plate constantly heating to maintain the temperature. Two baths in Remover PG with frequent manual agitation each for 5 min were used to remove big pieces of Ag flakes. Then the sample was soaked in Remover PG solution for 10 min followed by a 30 sec ultrasonic bath to lift the Ag layer more efficiently. A fourth bath of 5 min was used for rinsing purposes. Finally, the sample was rinsed with IPA and DI water for several times and blow dried with nitrogen.

Fig. 4.3 (b) and (c) are two examples of the final Ag structures after the lift-off process. Both images of the Ag lines and squares showed that we have good control over the shape of Ag nanostructures. The key to achieving accurate geometry control in EBL is the electron dose. Table 4.2 summarized the effect of electron dose exposed upon the PMMA on the geometry of the final plasmonic Ag lines. The “structure” column in Table 4.2 lists the target geometries, which are also the dimensions used for the designs in GDSII editor. Instead of the absolute value of the electron dose, the dose factor is used for simplicity. The dose factor of 1.0 is 100 μAs/cm^2, which corresponds to 6.25×10^{14} electrons/cm^2 or 6.25×10^6 electrons/μm^2. All the values of gratin pitch sizes and ridge widths are the average of five measurements at different locations under SEM.

From Table 4.2, we can clearly see that the grating pitches have relative errors of less than 0.2%, while the target grating duty cycles can be accurately achieved by controlling the electron dose. As discussed in Chapter 3 with the simulation results, the duty cycle of the gratings is critical in the excitation of SPPs.

SEM images of the Ag gratings in Fig. 4.4 showed the effect of the line width on the quality of the Ag gratings lines, while the pitch was 1040 nm and the height was 50 nm for all the four gratings. With 10% duty cycle and the line width of 104 nm, the lines are not well covered with Ag though the continuity of the line was not jeopardized. This is because a Ag film consists of grains (100 ~ 300 nm) and the lift-off process does not provide a clear edge when the feature size is small, which is due to the ultrasonic bath(s) and the non-vertical wall between the exposed/developed and unexposed areas. While all the images in Fig. 4.4 showed similar Ag grains, the Ag wires have better defined rectangular shapes with only few defects shown in Fig. 4.4 (b) as the grating line width gets to 156 nm for a 15% duty cycle. For higher duty cycle, the amount of defects is further reduced as shown in Fig. 4.4 (c) and (d) for 25% and 36% duty cycles, respectively.

Table 4.2 The effect of electron dose on the grating geometries

Structure	**Dose Factor**	**Pitch (nm)**	**Duty Cycle (%)**
Pitch: 850 nm Duty cycle: 36%	0.7	851.3	33.0
	0.75	849.3	34.6
	0.8	851.2	35.9
Pitch: 850 nm Duty cycle: 45%	0.65	848.0	41.8
	0.7	849.0	44.0
	0.75	851.5	45.2
	0.8	851.5	46.5
Pitch: 1040 nm Duty cycle: 20%	0.8	1049.7	19.7
	0.9	1044.0	21.0
Pitch: 1040 nm Duty cycle: 36%	0.7	1037.5	32.7
	0.75	1034.5	34.6
	0.77	1038.0	36.6
	0.8	1041.8	37.6
Pitch: 1040 nm Duty cycle: 45%	0.7	1030.5	42.4
	0.75	1039.0	44.1
	0.8	1042.0	45.7
Pitch: 1040 nm Duty cycle: 60%	0.55	1044.0	49.4
	0.65	1044.0	56.0
	0.75	1044.0	59.7
Pitch: 1250 nm Duty cycle: 36%	0.7	1244.0	33.7
	0.75	1249.3	36.2
	0.8	1249.8	37.6
Pitch: 1250 nm Duty cycle: 45%	0.7	1248.8	43.8
	0.75	1249.8	44.9

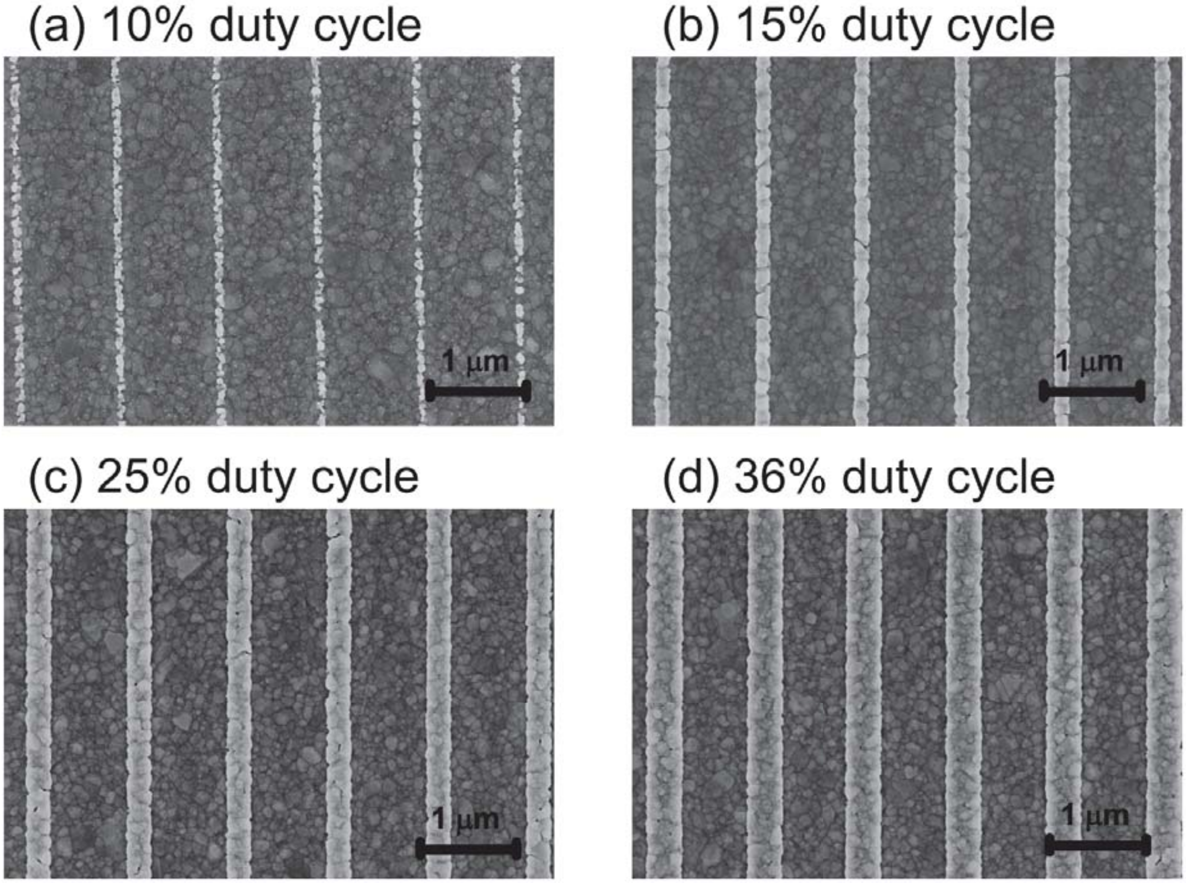

Fig. 4.4 Selective SEM images of Ag gratings with the same pitch size of 1040 nm and different duty cycles. The Ag lines have better quality with larger duty cycle, *i.e.* bigger Ag line widths.

Besides that gratings shown in Fig. 4.4, Table. 4.3 listed the accuracy of other gratings fabricated with EBL. Except for the 6.1% relative error for the grating with pitch 850 nm and duty cycle 36%, all other grating geometries showed relative error in the duty cycle less than 2%.

Table 4.3 The accuracy of duty cycles for different grating geometries

Grating pitch: 850 nm				
Target duty cycle (%)	25	36	45	65
Actual duty cycle (%)	24.8	33.8	44.5	65.2
Relative Error (%)	0.8	6.1	1.1	0.3
Grating pitch: 1040 nm				
Target duty cycle (%)	25	36	45	55
Actual duty cycle (%)	24.6	36.2	44.3	55.3
Relative Error (%)	1.6	0.6	1.6	0.5
Grating pitch: 1250 nm				
Target duty cycle (%)	36	45		
Actual duty cycle (%)	36.0	45.1		
Relative Error (%)	0.1	0.2		

4.1.2 Grating Fabrication with laser interference lithography

Interference lithography is a commonly used method to generate periodic structures. As listed in Table 4.1, laser interference lithography is suitable for fast and large area (in centimeter scale) exposures. Yet it is only capable of generating monotonically periodic features. The fundamental part of the lithography process is the generation of interference patterns from two or more coherent light waves. In my experiments, the Lloyd mirror setup is used for this purpose.

The schematic view of the Lloyd mirror setup for laser interference lithography is shown in Fig. 4.5. Figure 4.5 (a) demonstrates the generation of a clean and large area Gaussian beam from the laser beam. Figure 4.5 (b) shows the Lloyd mirror together with the sample stage for the generation of interference patterns on the photoresist film.

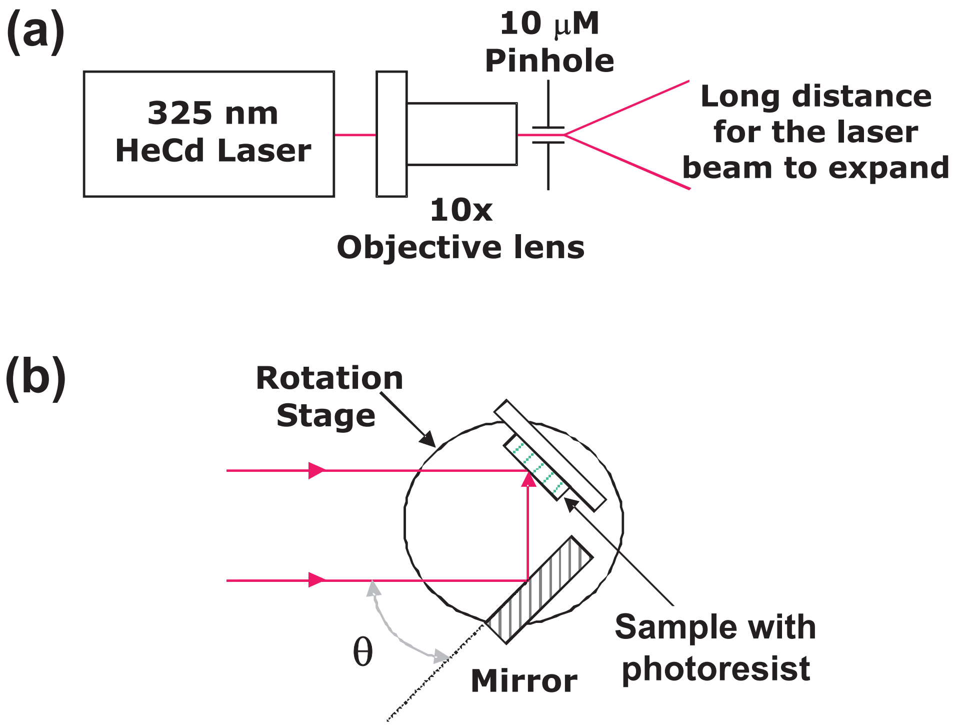

Fig. 4.5 The Lloyd mirror setup for making holographic patterning of photoresist gratings. (a) The generation of clean and large area Gaussian beam from a UV laser. (b) The Lloyd mirror setup with a mirror and the sample perpendicular to each other. Both of them are mounted on a rotation stage.

A He-Cd laser from Kimmon (Model: IK3201R-F, wavelength 325 nm, power 25.4 mW continuous wave) is used as the light source. A spatial filter consisting of a 10X objective lens and a 10 μm pinhole is used to clean up the laser beam. By removing the unwanted multiple-order energy peaks from the laser output and the spatial noises induced from dusts or mirrors used to change the light path, a clean Gaussian beam is produced. Large distance between the output of the spatial filter in Fig. 4.5 (a) and the sample stage in Fig. 4.5 (b) is needed for the Gaussian beam to expand to enable even light intensity distribution over the area of the sample. In my experiments, ~ 60 inches of distance is used and the final beam size has a diameter of ~ 12 inches. Then the sample and the Lloyd mirror are placed perpendicular to each other at the center of the final beam. Part of the final Gaussian beam will be reflected from the mirror which will then interfere with light directly shining on the sample, as shown in Fig. 4.5 (b). The bigger the mirror, the larger area the interference pattern will be. The mirror used in my experiments is 2.5 by 4 square inches, which is capable of generating interference patterns of 1.5 inch in the vertical direction and 0.2 inch ~ 1.5 inch in the horizontal direction depending on the desired feature size of the grating.

The grating fabrication process from laser interference lithography is very similar to that from e-beam lithography. Firstly, the photoresist film is spin-coated on the substrate and exposed to the interference pattern. The sample is then developed with appropriate developer according to different photoresists. Then the plasmonic grating can be obtained by deposition of a Ag film on top of the grating, followed by a lift-off process. In this thesis, however, the gratings from EBL are used for OPV tests and only photoresist gratings are made from the laser interference lithography.

The pitch of the photoresist grating is determined by the angle of the mirror, θ as in Fig. 4.5 (b), following Eq. 4.1. As a result, the smallest pitch available from a 325 nm laser is 162.5 nm.

$$\Lambda = \frac{\lambda_{HeCd}}{2 \cdot sin(\theta)} \tag{4.1}$$

A rotation stage is used beneath the mirror and sample stage to accurately control this angle. Table 4.4 gives a few examples of the changes in grating pitch with respect to different θ. Clearly, the grating pitch is very sensitive to the angle of the mirror. As a result, it is critical to accurately determine the light incident angle. From test runs, I found that there is an angle offset between the reading of the rotation stage and the actual θ value, where θ is 2.34 ~ 2.78 degrees smaller than the rotation stage reading.

Table 4.4 Dependence of the grating pitch on the mirror angle

θ (degree)	9.35	6.22	4.66	3.11
Grating pitch (μm)	1	1.5	2	3

Negative photoresist SU-8 formulation #2 (viscosity 45 cSt) from MicroChem is used. Photoresist gratings are made on silicon wafers for testing purposes. Pre-cleaned Si wafers are only further cleaned with iso-propanal (IPA) and baked at 100 °C for 10 min. Then the undiluted SU-8 is spin-coated with a two-step process. 500 rpm, 5 sec is used as the first step for even distribution of SU-8. Then spinning speed is ramped at an acceleration rate of 300 rpm/second till it reaches 2000 rpm and the sample is span for another 30 sec. The SU8 film is then baked at 100 °C for 1 min. The exposure time for the SU-8 film is 30 sec to 60 sec, depending on the desired grating duty cycle. A post-exposure bake at 100 °C for 1 min is followed. SU-8 developer from MicroChem is used for the development of unexposed SU-8. The sample is rinsed in a SU-8 developer bath for 1 min and then rinsed in 3 baths of IPA for a total time of ~ 3min followed by blowing dry with air.

With one time exposure, one dimensional grating can be obtained. With double exposure and θ of the two exposures with a 90 degree difference, two dimensional gratings can be made. The SEM images of two gratings are shown in Fig. 4.6. The high laser power makes it possible to make nanostructures with high aspect ratio and clear edge, as shown in Fig. 4.7.

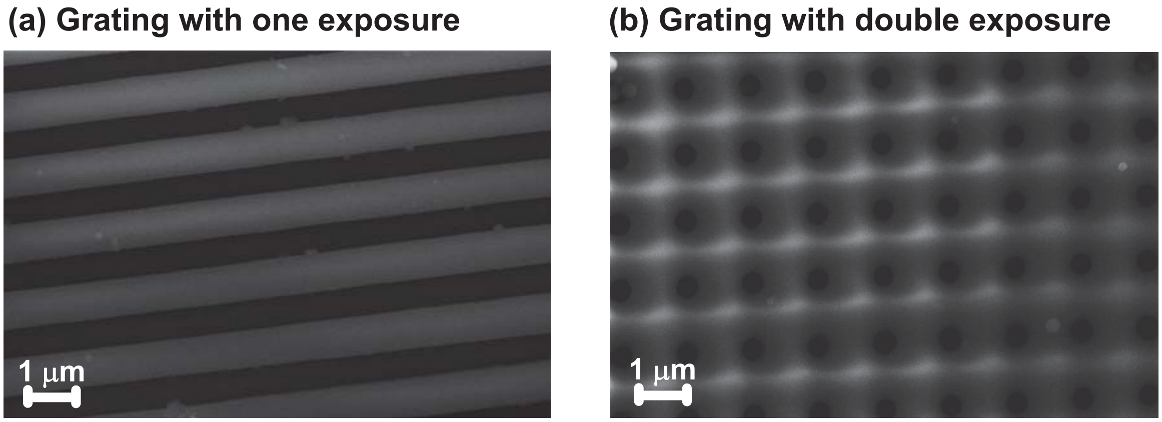

(a) Grating with one exposure

(b) Grating with double exposure

Fig. 4.6 SEM images of a (a) one dimensional grating from one time exposure and (b) a two dimensional grating from double exposure.

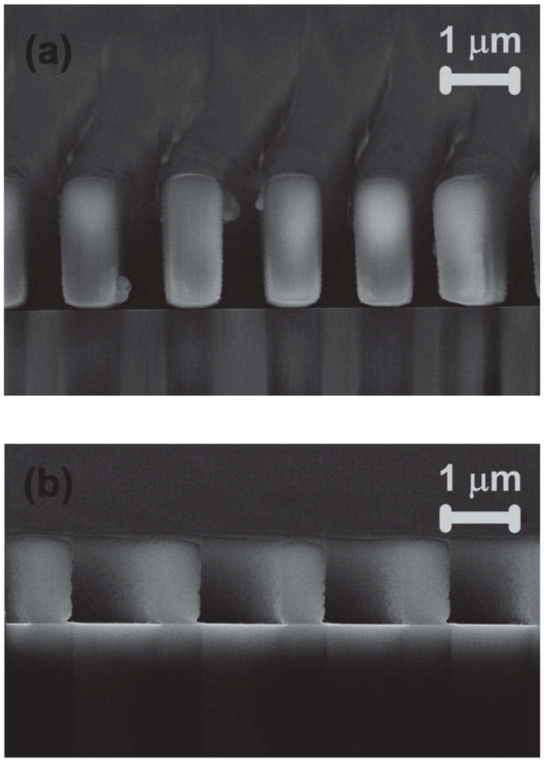

Fig. 4.7 Cross section SEM images of two gratings with different exposure times and geometries.

The grating geometries are summarized in Table 4.5 for the gratings in Fig. 4.6 and Fig. 4.7. The "20+20" exposure time of the grating in Fig. 4.6 (b) means the sample is exposed for 20 sec at one angle and then the sample is rotated for 90 degrees and exposed again for another 20 sec. Table 4.5 also shows that the grating duty cycle is very sensitive to the exposure time. With a longer exposure time, the duty cycle increases accordingly.

Table 4.5 Selective grating geometries made from laser interference lithography

Grating structure	Exposure time (sec)	Height (μm)	Pitch (μm)	Duty cycle (%)
Fig. 4.6 (b)	20 + 20	1.905	1.40	67.3
Fig. 4.6 (a) & Fig. 4.7 (a)	30	1.913	1.37	57.6
Fig. 4.7 (b)	25	1.184	1.80	36.7

4.2 Reflection measurement with microspectrometer

To demonstrate the impact of Ag gratings on light trapping in OPVs through the excitation of horizontally propagating surface plasmon polaritons (SPPs) and waveguide modes, we've fabricated gratings of different sizes and measured the light reflection from the solar cells on these gratings. Due to the 100 nm Ag bottom electrode, the light transmission is close to zero and the wavelength dependent absorption $A(\lambda_o)$ is calculated from: $A(\lambda_o) = 1 - R(\lambda_o)$, where $R(\lambda_o)$ is the light reflectance of the OPVs. We have confirmed that when Ag gratings are present on the back of the OPVs, $R(\lambda_o)$ is significantly reduced for $\lambda_o > 600$ nm, which suggests increased light absorption enabled by the plasmonic gratings.

For better control on the OPV structure to achieve fair comparisons, gratings of different geometries were fabricated on the same substrate with EBL so that they have identical OPV on top of them. The size of each grating is 800 μm × 800 μm and the reflection was measured from 400 nm to 900 nm for both TE and TM waves from a ~ 320 μm × 320 μm area.

4.2.1 Microspectrometer setup and working principle

The micro-scale reflection measurement was done with a micro-spectrometer system as show in Fig. 4.8.

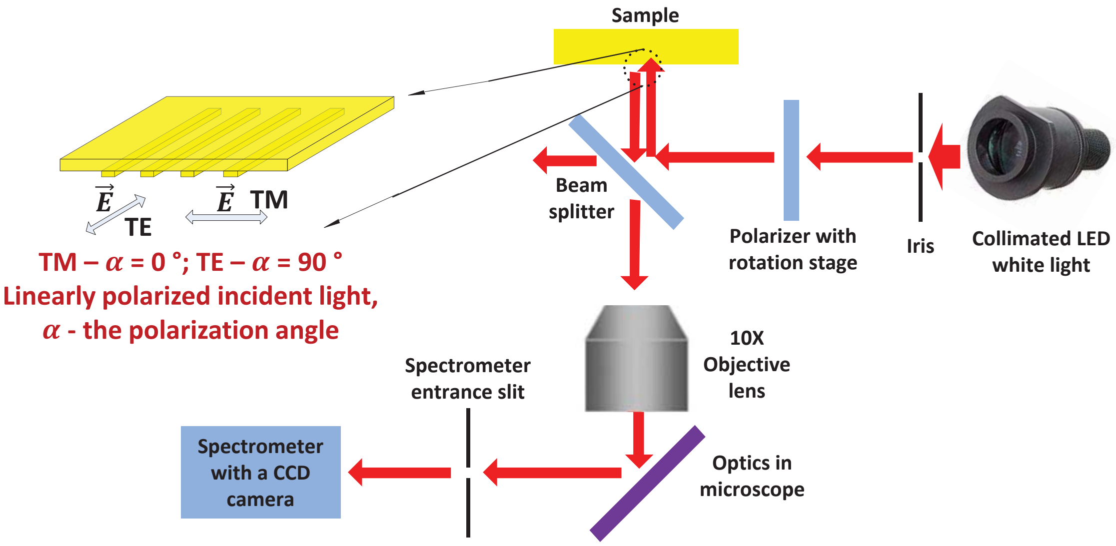

Fig. 4.8 Schematic diagrams of the micro-spectrometer with an external collimated white LED as the light source.

The main body of the micro-spectrometer consists of a Leica DMI3000 B microscope and an Acton SP-2358 spectrometer from Princeton Instruments equipped with a PIXIS 256 CCD camera with 1024×256 resolution. The spectrometer is calibrated with a dual Hg and Ne/Ar light source for 200 ~ 1000 nm with the error in the wavelength of less than 2 nm. The microscope was originally designed only for transmission (forward scattering) measurements with unpolarized light source. To expand the measurement capability of the micro-spectrometer, external white LED as the light source (Thorlabs, MCWHL2-C2) together with a beam splitter (Thorlabs, BS007) were used to enable measurement of reflection. A polarizer placed in front of the LED light source is used to generate a linearly polarized light as the incident light on the OPVs. We used a rotation stage to change the polarization angle α and to switch the incident light between TE and TM states as shown in Fig. 4.8.

The working principle of the micro-spectrometer is shown in Fig. 4.9. Fig. 4.9 (a) schematically shows a group of gratings with different geometries fabricated on the same substrate. By using a microscope with objective lens of 10X and 0.25 NA together with a 10X ocular (eyepiece) lens, only one grating (800 μm × 800 μm) is imaged in the microscope field of view as illustrated in Fig. 4.9 (b). The region of interest (ROI), *i.e.* the region to be measured, is marked by a red rectangle. To limit the measurement region to the ROI, firstly a physical slit with adjustable width is used at the entrance of the spectrometer to block unwanted area in X direction, as shown in Fig. 4.9 (c). Then according to the resolution of the CCD camera (1024×256 in this case), the visible area passing the slit is divided into N sections (N=256 here) and each section will generate a spectral response on the CCD camera. For illustration, N =12 is assumed as shown in Fig. 4.9 (d). Their assumptive spectra are shown in Fig. 4.9 (e). If #5~8 falls in the grating area, the spectral response in the corresponding area will show high signal intensity while from sections 3, 4 and 9, 10, only low signals will appear due to the fringing effects. Regions far away from the grating (1,2 and 11,12) will show no peak in their spectra. By choosing spectra 6 and 7 (marked by red arrows in Fig. 4.9 (d) and (e)), we are collecting

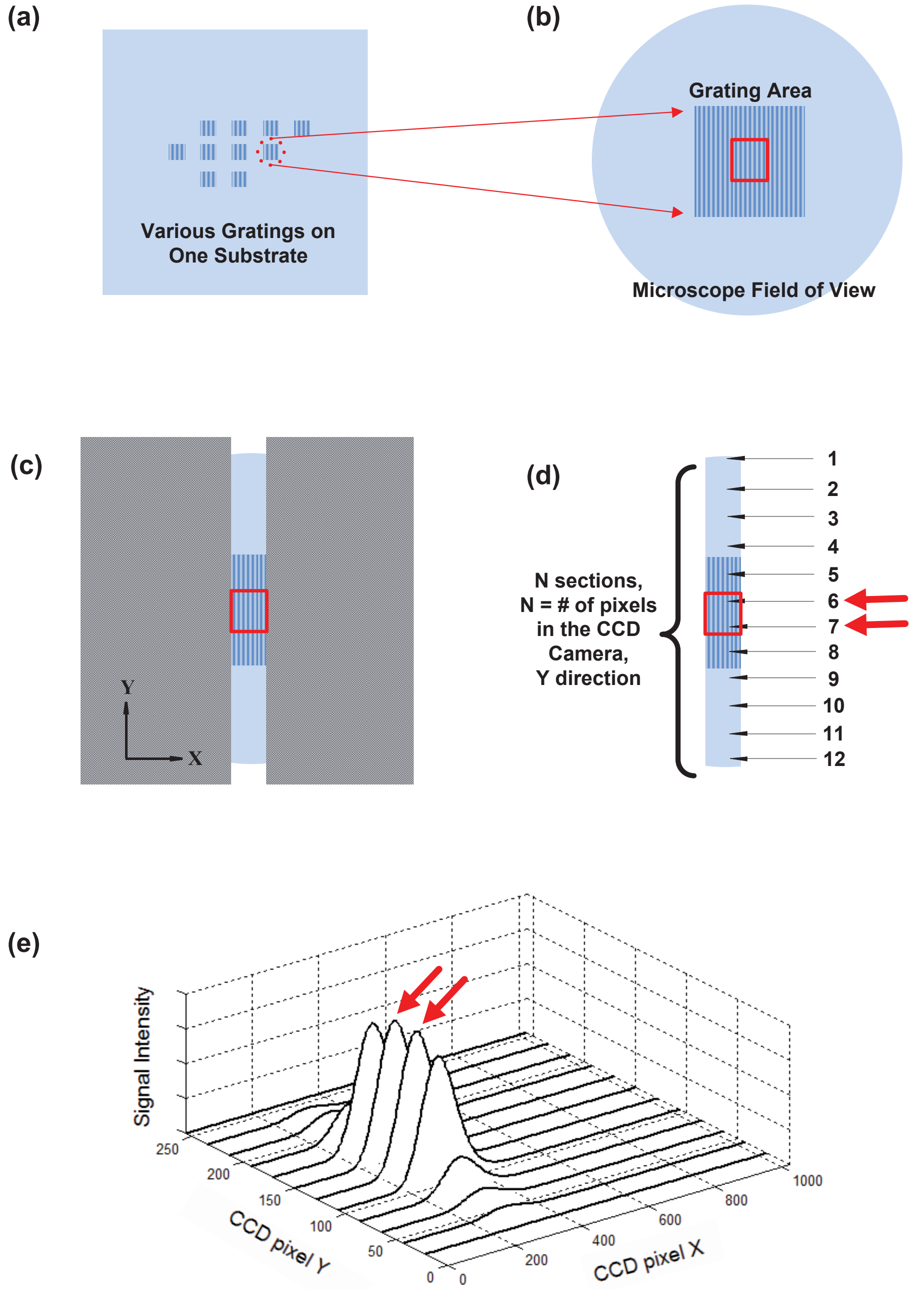

Fig. 4.9 Working principle of micro-spectromter, (a) a group of gratings on the same substrate; (b) only one grating (800 µm × 800 µm) is imaged in the microscope field of view, (c) using a physical slit to block unwanted area in X direction, the region of interest is marked with the red rectangle, (d) and (e) using a CCD camera to select signals from only the ROI area.

the signal from the ROI (red rectangle in Fig. 4.9 (d)) only and thus enabling the micro-scale measurement with ROI restricted in both X and Y direction.

4.2.2 Reflection measurement

To quantify the reflection, a flat dielectric mirror with more than 99% reflection between 400 ~ 900 nm is used as a 100% reflection reference ($Ref_{100\%}$). The signal recorded with no sample present is set as 0% reference ($Ref_{0\%}$). Then the reflection in percentage is calculated from:

$$Reflection = \left(S_{sample} - Ref_{0\%}\right)/(Ref_{100\%} - Ref_{0\%}) \tag{4.2}$$

where S_{sample} is the signal level from the sample. While measuring S_{sample} and $Ref_{100\%}$, the top surface of the sample and the flat mirror are kept at the same height throughout the measurements.

The raw data and the calculated reflection spectra are shown in Fig. 4.10 as an example. Fig. 4.10 (a) shows the reflected signal with incident TM waves collected by the CCD camera from Ref 100% (a commercial mirror), Ref 0% (no sample), a 100 nm flat Ag film (thermally evaporated) and a Ag grating sample (on a 100 nm Ag film, pitch 1040 nm, duty cycle 36%, ridge height 50 nm). The flat Ag film showed reflected signal as high as the commercial mirror, while from the grating sample the reflection was significantly reduced, especially around 600 nm at which strong plasmonic resonances are predicted to occur. By using Eq. 4.2, the reflectance is calculated for the samples of a flat Ag film and a Ag grating. The results are shown in Fig. 4.10 (b). Clearly, the Ag grating showed much lower reflection due to the excitation of SPP modes by the incident TM waves. The absorption is calculated from:

$$A(\lambda_o) = 1 - R(\lambda_o) \tag{4.3}$$

And then increase of light absorption is obtained from:

$$A_{absorption\ increase} = A_{area\ w/\ gratings} - A_{area\ w/o\ gratings} \tag{4.4}$$

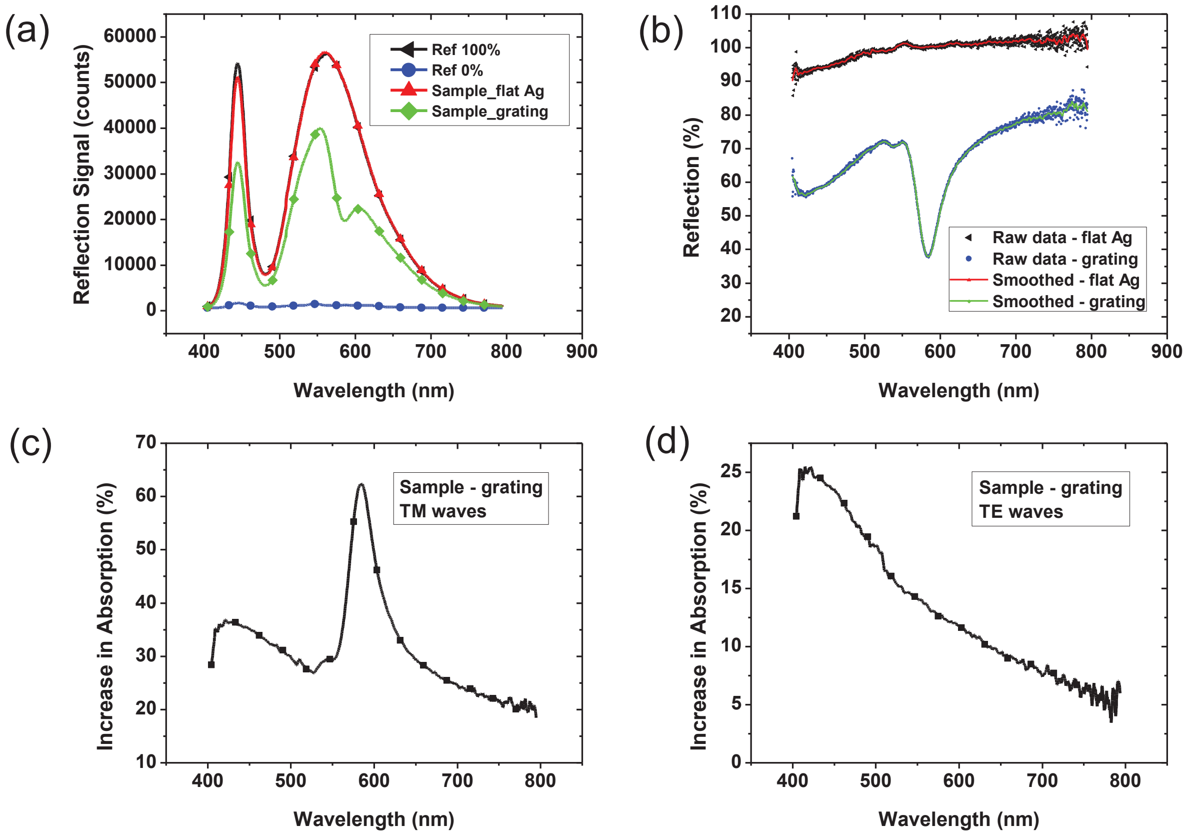

Fig. 4.10 (a) Raw data of reflected signals from the references and two samples; (b) The reflection spectra for the flat Ag and grating samples, the black and blue scattered showed the data calculated from Eq. 4.2, while the solid lines show the results after smoothing; (c) and (d) are the grating induced absorption increase for TM and TE waves, respectively.

The grating induced increases in absorption which equal the decreases in reflection are shown in Fig. 4.10 (c) and (d) for TM and TE waves, respectively. Both showed an absorption peak near 410 ~ 420 nm, which is induced by higher diffuse reflection and stronger absorption in the Ag film [29, 84]. In addition, there is another absorption enhancement peak at ~ 585 nm for TM waves due to the grating induced propagating SPP mode. In contrast, for TE waves, the increase in absorption monotonously decreases as the wavelength increases. For the study of grating induced absorption enhancement, the increase in the absorption will be presented and compared in the following sections, rather than the reflection spectra.

To verify the robustness of the reflection measurement system, the impacts of the size of the ROI, the sample position and the numerical aperture of the object lens on the results are studied. The sample used here is a OPV structure with a grating of 1040 nm pitch, 36% duty cycle and 50 nm height on the bottom, compared with a OPV without gratings. Both samples are on the same substrate for fair comparisons. The fabrication of the OPV sample will be discussed in more details in Chapter 5 and 6.

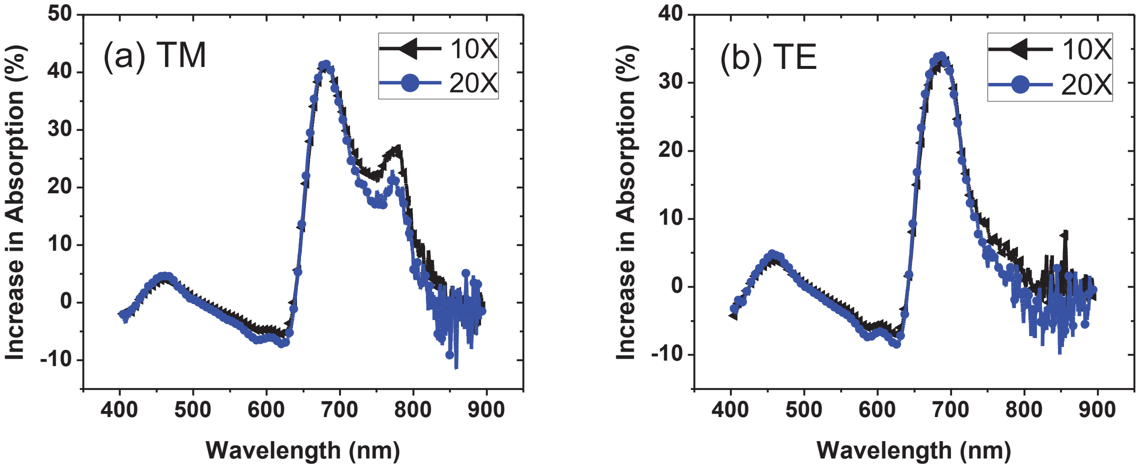

Fig. 4.11 Comparisons of light absorption enhancement results from OPVs with a grating on the bottom, for (a) TM waves and (b) TE waves. Objective lenses with different magnificent and thus different light acceptance angles are used.

Objective lens allows the light collection from a cone and the numerical aperture (NA) defines the maximum collection angle. In our setup, two different objective lenses are tested and the results are compared in Fig. 4.11. The intensity of the LED light source is adjusted accordingly to suit the different lenses. The NA are 0.25 and 0.4 for 10X and 20X objective lenses, respectively. The corresponding acceptance angles are 29.0 and 47.2 degrees, respectively. The results in Fig. 4.11 are almost identical for both TM and TE waves, which suggests that the reflection from the OPV samples is mainly within a cone with small angles to the normal direction.

The 10X objective lens is then chosen for all the measurements due to its longer focal length which allows me to focus well on the samples to be measured. Then I tested whether or not the distance between the sample and the objective lens will affect the results. The sample is firstly measured when it is at the focal point of the objective lens. Then I moved the objective lens up and down by 5 mm and the three sets of results are compared in Fig. 4.12. This 10 mm change in the sample location is much bigger than the size of the 320 μm × 320 μm ROI area. Again, the identical results in Fig. 4.12 prove that the microspectromter system is insensitive to changes in the location of the sample.

Finally, the sample is measured with different ROI sizes. For the grating size of 800 μm × 800 μm, three different measurement areas are tested: small ROI - $(160\ \mu m)^2$, medium ROI - $(320\ \mu m)^2$ and big ROI - $(640\ \mu m)^2$. The results for both TM and TE waves are shown in Fig. 4.13. For the small and medium ROIs, the results are identical. When the ROI size is comparable to the size of the grating area, the TM absorption peaks showed slight decrease enhancement due to the fringing effect. As a result, ROI of $(320\ \mu m)^2$ is used for all the rest of the measurements.

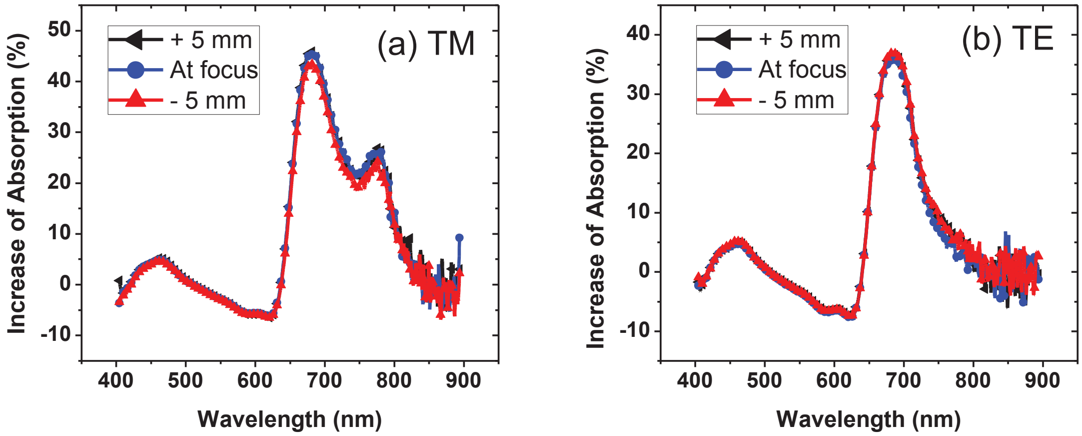

Fig. 4.12 Comparisons of light absorption enhancement results from OPVs when the distance between the sample (and the 100% reference mirror) and the objective lens is different.

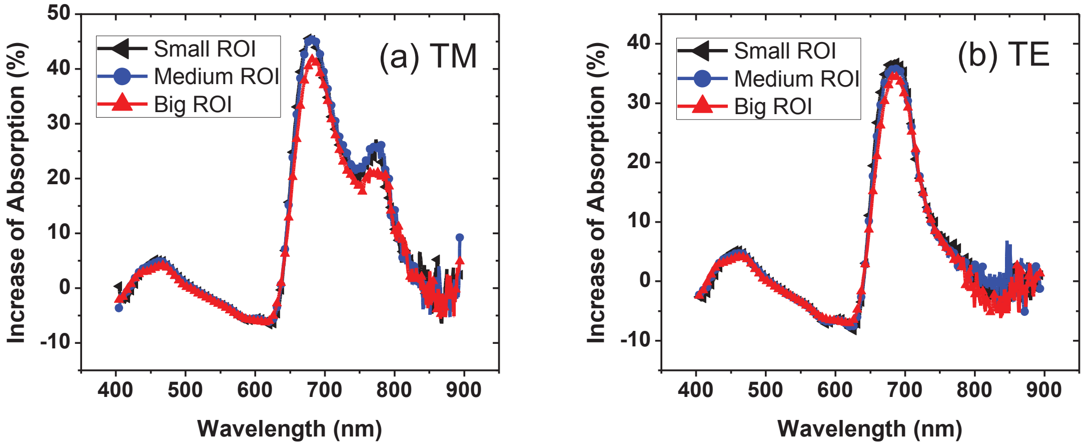

Fig. 4.13 OPVs are tested with different sizes of ROI, the grating size is (800 μm)^2. The ROI sizes are (160 μm)^2, (320 μm)^2, (640 μm)^2 for small, medium, big ROIs, respectively. Only the absorption enhancement peaks for TM waves under the big ROI showed slightly decreased peak intensity.

Chapter 5. Absorption enhancement in OPVs

From numerical simulations in Chapter 3, I showed that the grating duty cycle is a critical structural parameter, while the grating pitch and grating height also play important roles in the light trapping efficiency. With the help of the EBL and micro-spectrometer systems, I was able to fabricate various gratings on the same substrate and fairly compare the impact of the grating geometries on the light absorption enhancement.

The fabrication and geometry characterization of the Ag gratings were discussed in Section 4.1. Gratings with different geometries were fabricated by EBL while the size of each grating is 800 μm × 800 μm. Then the OPV structure on top of different gratings was made as follow. Firstly, a thin Cs_2CO_3 layer was formed by spin coating of a 0.2 wt% Cs_2CO_3 solution in 2-ethoxyethanol at 4000 rpm for 60 sec followed by annealing at 160 °C for 20 min in the ambient. The active layer was spin-coated from P3HT:PCBM (1:1 weight ratio, total of 30 mg/ml in dichlorobenzene) at 400 rpm for 60 sec, followed by annealing at 110 °C for 12 min. A 15 nm thermally evaporated MoO_3 and a 120 nm ITO (from sputtering at room temperature at 1 Å/sec) act as the top transparent electrode. More details about the material suppliers and fabrication processes are enclosed in Section 6.2.

5.1 Comparisons between simulation and experimental results

5.1.1 Characterization of gratings and OPVs

Before performing the optical characterization of the silver gratings and the OPVs, cross section SEM images were taken to reveal the OPV structure. Figure 5.1 shows the cross section structures of a bare grating and a OPV structure on a grating with the same geometry. The grating in Fig. 5.1 (a) has 1040 nm pitch, 36% duty cycle and 55 nm grating height. Fig. 5.1 (b) clearly reveal the conformity of the P3HT:PCBM and ITO layer. This is different from the assumption of a flat P3HT:PCBM surface in the simulations. However, the fluctuation in the thickness of P3HT:PCBM and ITO layers at this length-scale do not induce much diffraction as suggested by the agreement between simulation and experimental results in this section.

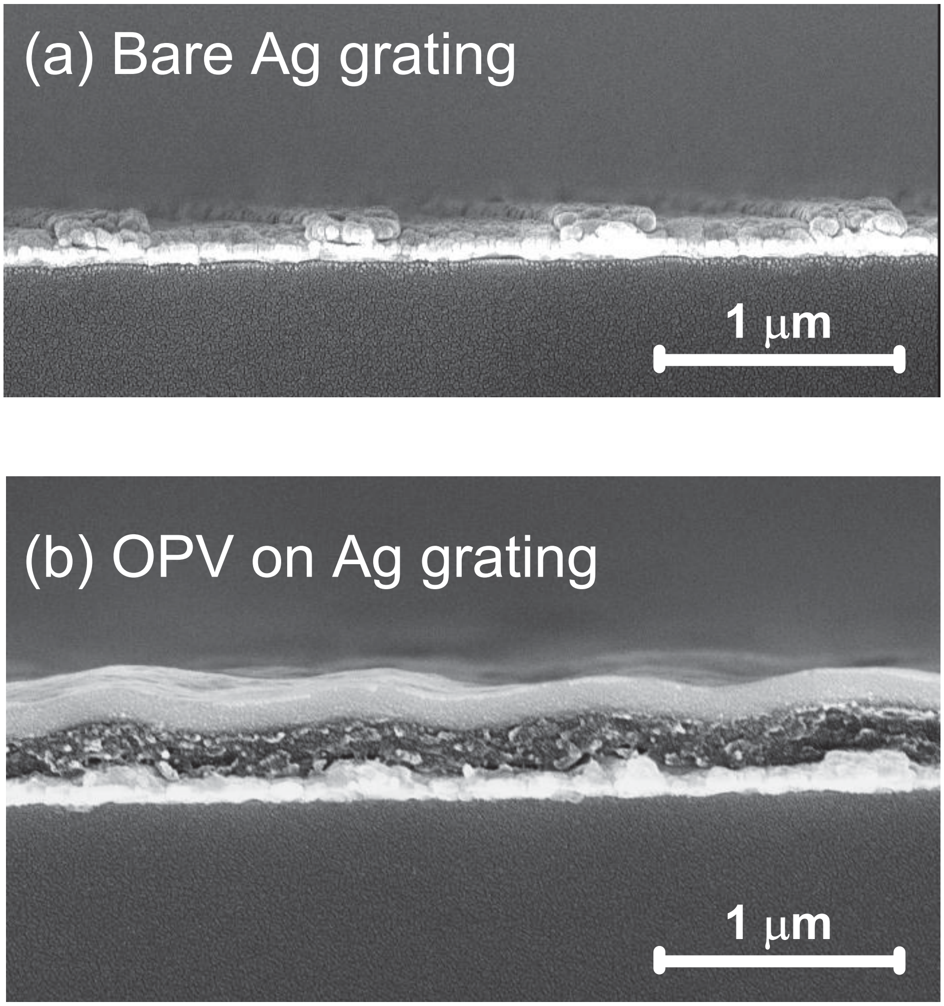

Fig. 5.1 The cross section SEM images of (a) a bare Ag grating and (b) a OPV on the Ag grating showed that with a grating height of 50 nm, conformal coating of the polymer layer and the electrode materials are achieved.

The conformal coating of the polymer layer and the electrode shown in Fig. 5.1 (b) was over the entire substrate including areas with and without gratings. SEM images with higher magnifications have more information about the thicknesses and morphology of different layers, as shown in Fig. 5.2 (a) and (b) for a bare silver grating and OPV, respectively.

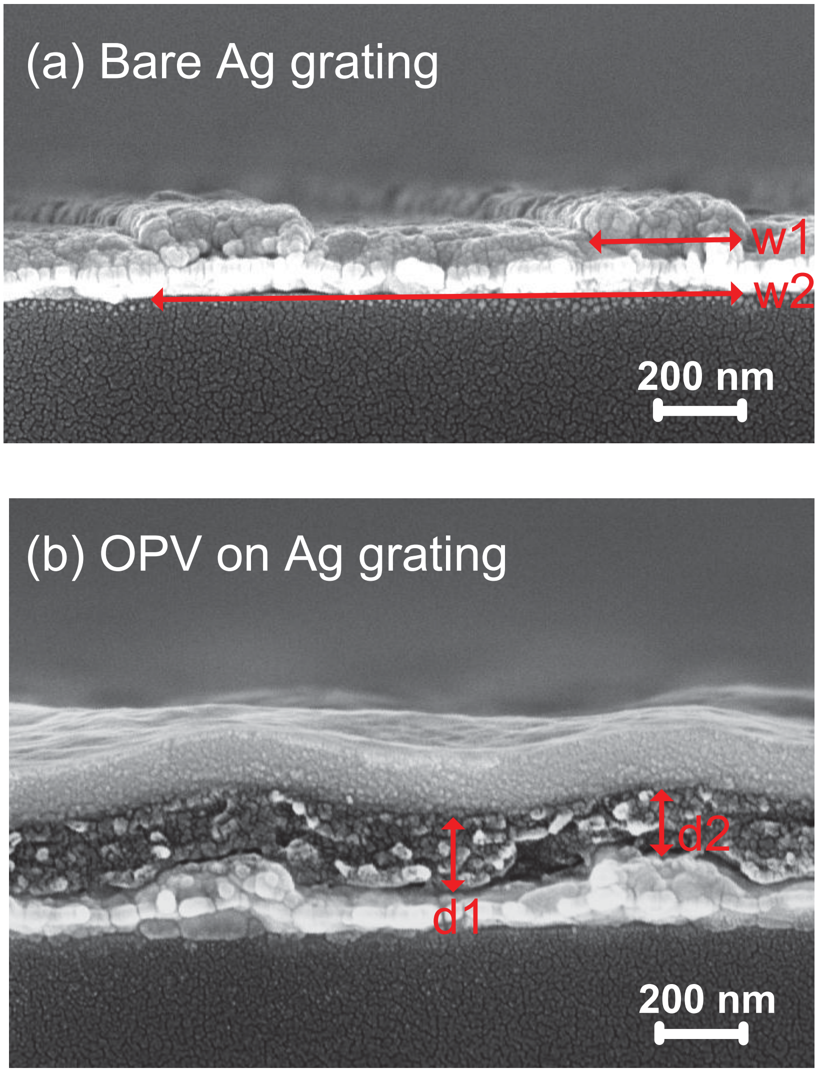

Fig. 5.2 The cross section SEM images of (a) a bare Ag grating and (b) a OPV on the Ag grating at higher magnification clearly showed the large Ag grains. These images are also used to determine the thicknesses of the P3HT:PCBM and ITO layers.

In Fig. 5.2 (a), it is clear that the Ag grating has fairly large grains, leading to non-straight edges of the grating ridges. The grainy feature in the gratings has an impact on the absorption enhancement peaks, which will be discussed more in section 5.2.2. It is a common issue that samples are slightly tilted while checking their cross section under SEM. As a result, the height of the Ag grating and film cannot be derived from Fig. 5.2 (a). By taking the ratio between $w1$ and $w2$ as marked in Fig. 5.2 (a), the grating duty cycle is confirmed to be 35.8%, which is the averaged value based on 5 measurements. This is in agreement with the SEM images of the grating top surface, suggesting that the grating profile is still pretty rectangular. In Fig. 5.2 (b), the polymer thickness is 160 ~ 200 nm on different locations. Even though this may not be the exact thickness of the P3HT:PCBM layer, it confirms the thinness of the photoactive layer. The ratio between $d2$ and $d1$ turned out to be 0.87, averaged from three measurements. This suggests the OPV structure is pretty conformal with the top surface features slightly shallower than the features of the grating substrate.

To further investigate the surface morphology of the Ag gratings and the OPVs, AFM images are taken as shown in Fig. 5.3. The surface morphology of the bare grating in Fig. 5.3 (a) clearly shows that the Ag grains have different height. The height of the grating is estimated by firstly averaging the AFM image along the grating lines and then taking the height difference between the ridge and groove areas. The averaged depth profile is also shown in Fig. 5.3 (a), with the areas used for step height estimation marked by red and green rectangles. The area in Fig. 5.3 (a) has a step height of 60.176 nm, yet the grating height is between 54 ~ 60 nm on different locations. The AFM image of the OPV surface is much rougher as shown in Fig. 5.3 (b). It also has periodically changing height profile with the same pitch as the grating. The step height of the OPV top surface is between 44 ~ 54 nm on different locations, which is smaller than that of the Ag grating. The step height ratio between the OPV and the grating is around 0.83 on average, which is in agreement with the results obtained from cross section SEM images.

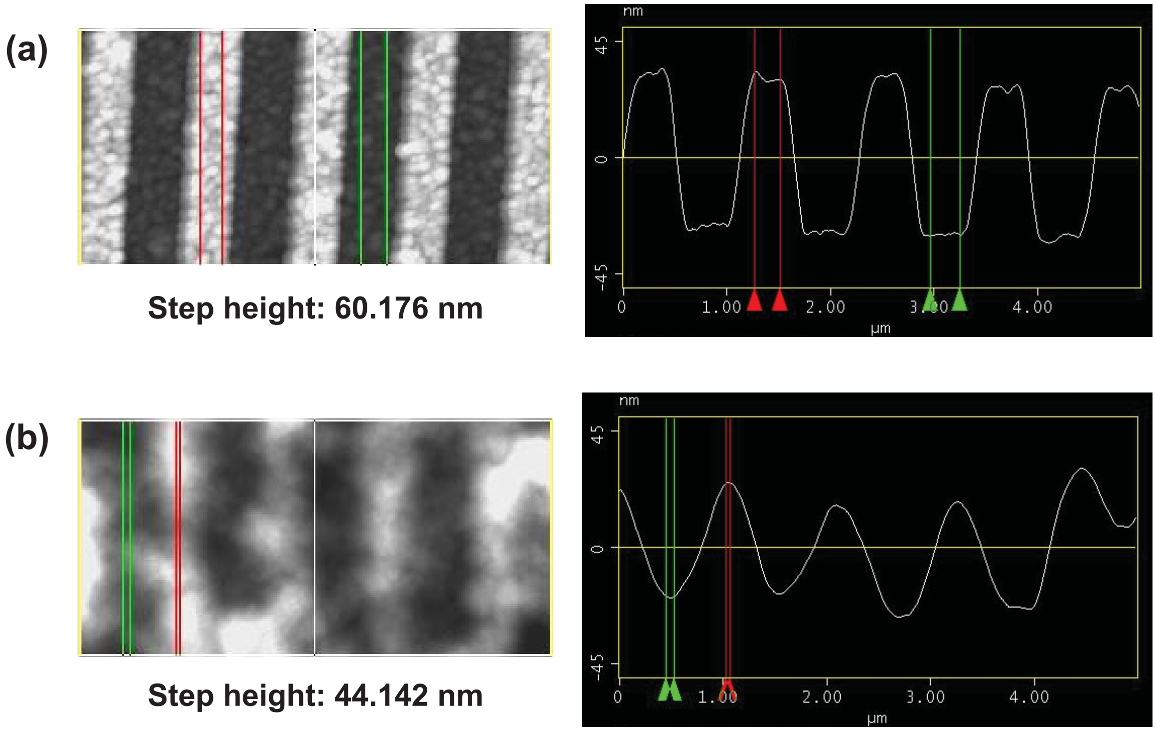

Step height: 60.176 nm

Step height: 44.142 nm

Fig. 5.3 AFM images and depth profiles of (a) a bare Ag grating and (b) a OPV on the Ag grating. The grating is estimated to be 54 ~ 60 nm on different locations, while (a) shows 60.176 nm. The grating feature with reduced height is also shown in the AFM image (b) of the OPV structure. The step height of the OPV top surface is between 40 ~ 54 nm on different locations.

5.1.2 Bare grating results comparisons

The reflection from both bare gratings and OPVs was measured over 400 ~ 900 nm spectral span for both TM and TE waves. The ROI for all the measurement is (320 µm)^2. The increase in absorption, which is derived from the decrease in reflection compared with a flat Ag film, is shown in Fig. 5.4 for gratings with a 1040 nm pitch size and different duty cycles for TE and TM waves, respectively. The increase in absorption calculated from COMSOL simulations are also superimposed for comparisons. In both TE and TM cases, all the salient features in the experimental and simulation curves are in good agreement; with some of the features marked with red arrows in Fig. 5.4.

For TM waves, the absorption peaks for duty cycles of 15%, 25% and 60% are in great agreement, with broadened peaks in experimental results. The peak broadening in can be ascribed to the grainy nature of the thermally evaporated Ag films which case loss. The experimental peak for duty cycle of 55% is broad and flat, yet the simulation shows one peak at 450 nm with large absorption increase and a tiny peak around 532 nm. Since the wavelength of the two peaks are in good agreement between experiments and simulations, the differences between the peak shapes can be ascribed to broadening of the peaks and more importantly interaction between the two peaks forming a broad one. When the duty cycle is 36% or 45%, a distinction shift in the absorption peak wavelength is observed. It is also obvious that the SPP peaks have very asymmetric shape with wider width on the long-wavelgnth side, which is very different from those at other duty cycles. Meanwhile, the wavelengths where the SPP peaks start are all in great match for duty cycles of 36% and 45%, as marked with green arrows in Fig. 5.4 (b1), (c1) and (d1). The explanation for this phenomenon is still under investigation. Strong interaction between the two resonant peaks may be one of the contributions.

The increase in absorption in TE waves is also shown in Fig. 5.4 for gratings with different duty cycles. The increased absorption is possibly due to the extra Ag volume and higher diffuse scattering. There is a consistent shift in the peak wavelength in Fig. 5.4 (a2) ~ (f2), which is due to impurities in Ag or possible differences between the refractive

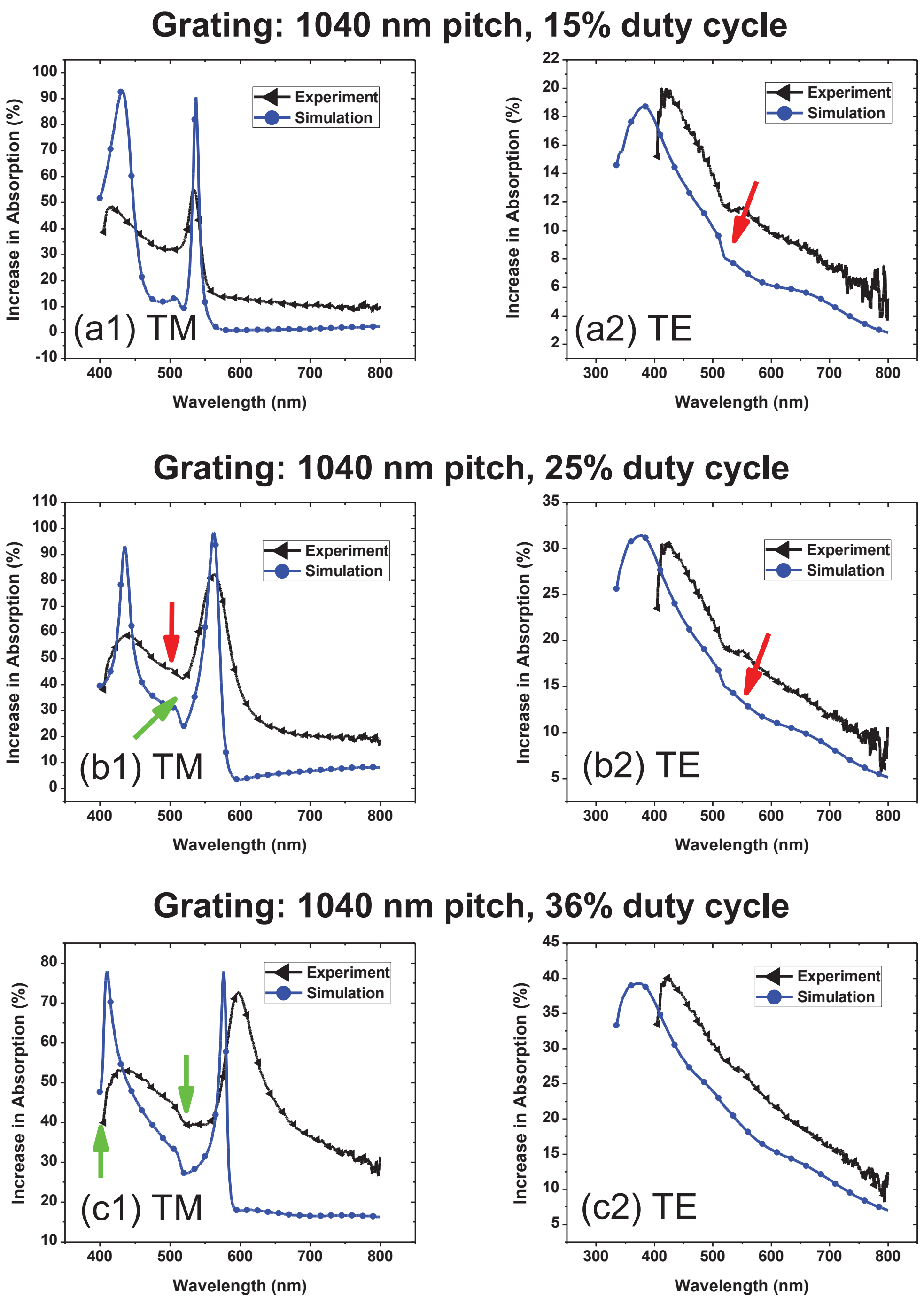

Fig. 5.4 Compared with a 100 nm flat Ag film, the absorption from bare Ag gratings is increased. The abortion peaks for different grating geometries are shown. The red arrows indicate the good agreement between COMSOL simulation and experimental results, while the green arrows mark the starting wavelengths of the SPP peaks.

Grating: 1040 nm pitch, 45% duty cycle

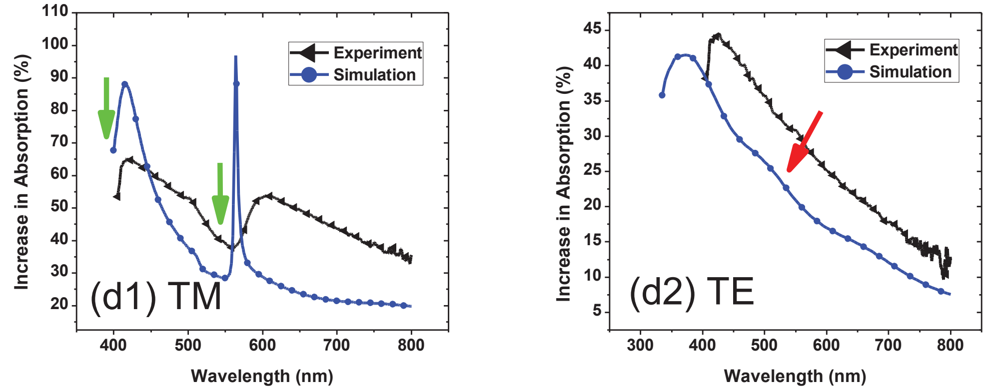

Grating: 1040 nm pitch, 55% duty cycle

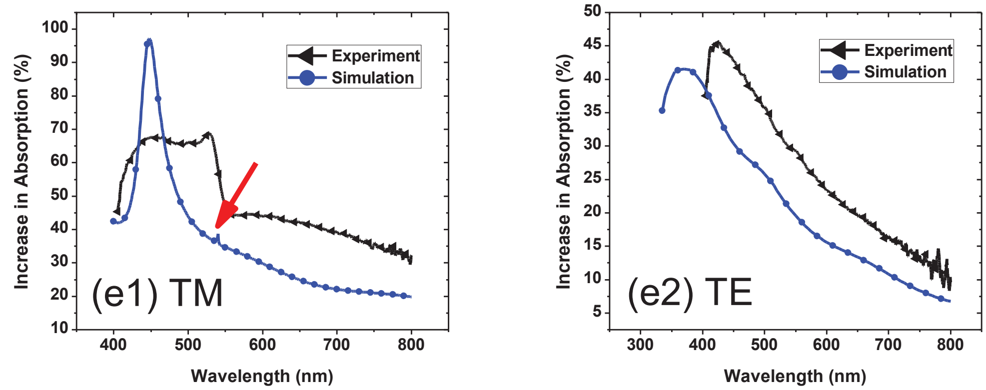

Grating: 1040 nm pitch, 60% duty cycle

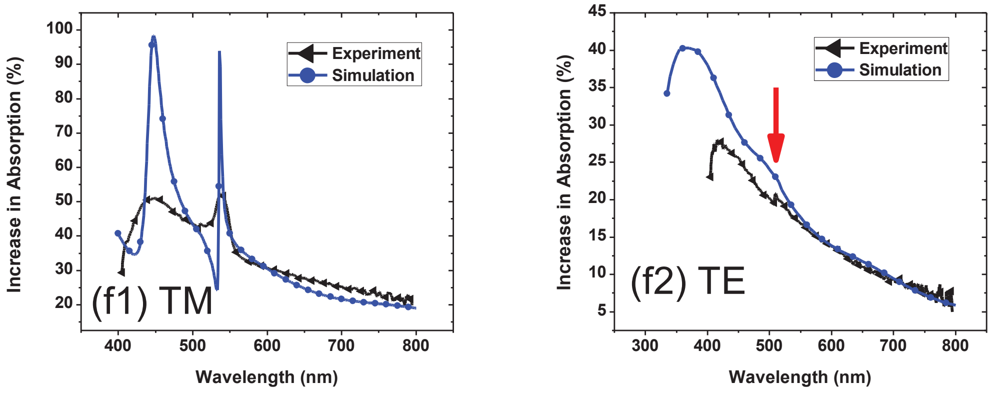

Fig. 5.4 (continued) Compared with a 100 nm flat Ag film, the absorption from bare Ag gratings is increased. The abortion peaks for different grating geometries are shown. The red arrows indicate the good agreement between COMSOL simulation and experimental results, while the green arrows mark the starting wavelengths of the SPP peaks.

indices used for the modeling and the experiment. It has been reported that the resonance wavelength of Ag islands in thin Ag films is very sensitive to the changes in film thickness and the substrate material [84, 85]. The Ag grains in the gratings may contribute to the blue-shift of the absorption peak. Despite the shift in the peak wavelength, all the salient changes in the slope of the monotonous curves are in good agreement between the experimental and simulation results, with a few examples marked with red arrows.

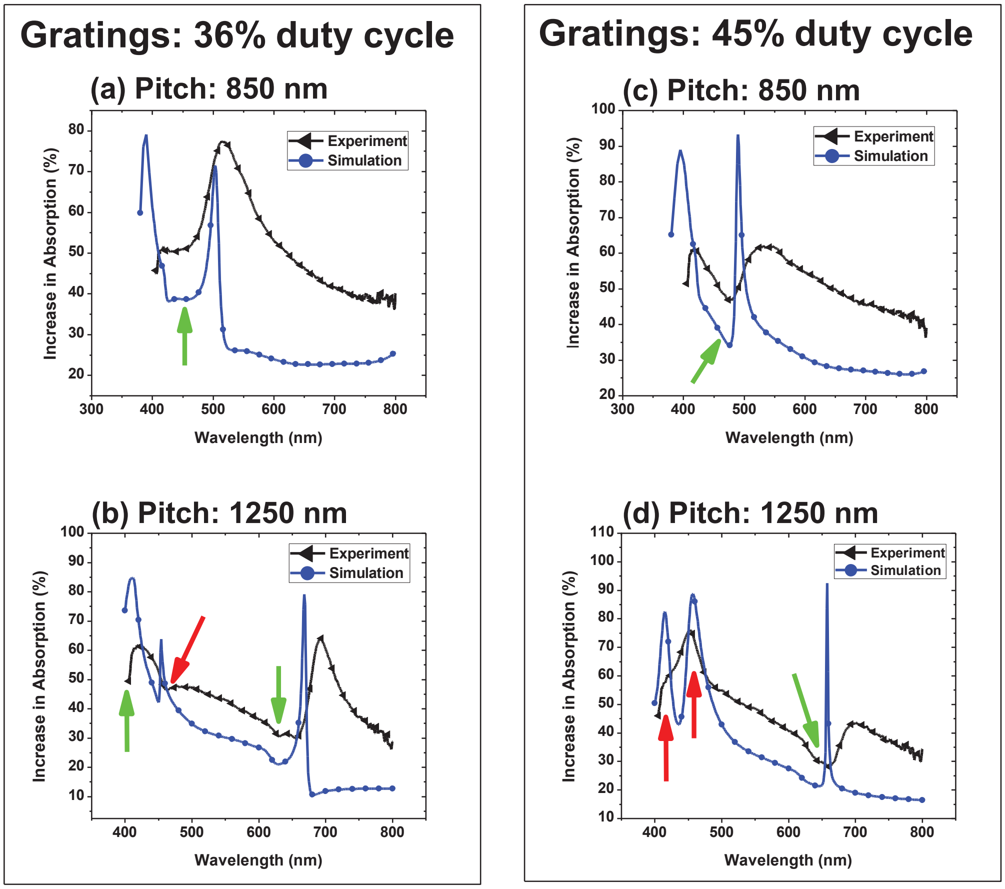

Fig. 5.5 Compared with a 100 nm flat Ag film, the absorption from bare Ag gratings is increased. The abortion peaks for different grating geometries under TM waves are shown.

The effect of the grating pitch on the increase in absorption is shown in Fig. 5.5 for duty cycles of 36% and 45% for TM waves. Similar absorption peaks are seen in both experimental and simulations results. Similar to Fig. 5.4 (c1) and (d1), the peaks at ~ 500 nm for 850 nm pitch (Fig. 5.5 (a) and (c)) and the peaks at ~ 660 nm for 1250 nm pitch (Fig. 5.5 (b) and (d)) are red-shifted. Again, the interaction between nearby SPP peaks may contribute to the asymmetrically broadening of the peaks. The fact that this phenomenon is most obvious for duty cycle of 36% ~ 45%, indicates the interaction between plasmonic modes gets stronger when the lengths of the grating ridges and grooves get comparable.

The increase in absorption in TE waves is shown in Fig. 5.6 for gratings with different pitches. Similar to Fig. 5.4 (a2) ~ (f2), there is a consistent blue-shift for the peak near 400 nm. Yet the slopes of the monotonous curves at longer wavelengths are in good agreement between simulations and experiments for all grating geometries.

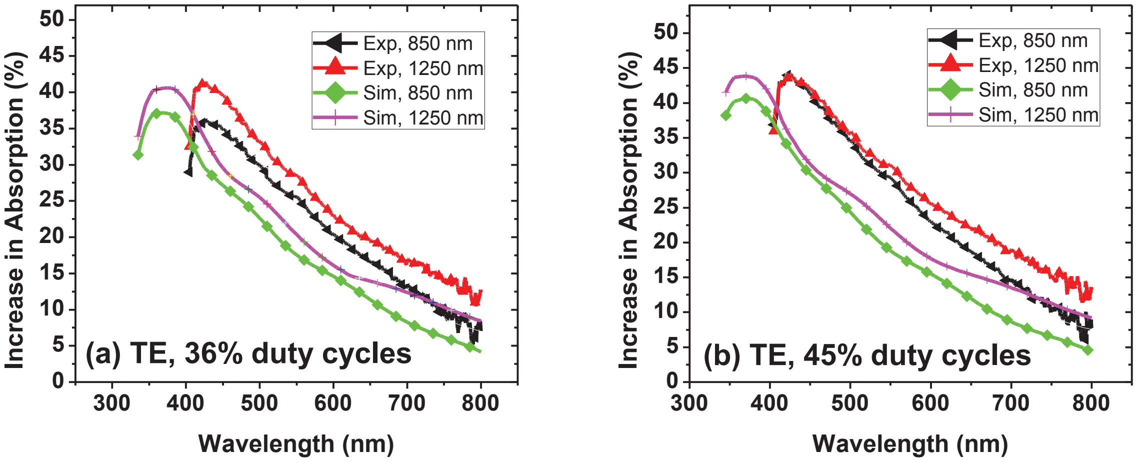

Fig. 5.6 For gratings of different pitch sizes, comparisons between simulation and experimental results for TE waves are shown for the duty cycle of 36% and 45% in (a) and (b), respectively. Even though the absorption peaks exhibit blue-shift deviation from the simulation results, the slopes of the monotonous lines at longer wavelengths are in good agreement for all grating geometries.

5.1.3 OPV results comparisons

Then the reflection was measured for OPVs on the substrate with several grating present. The increase in absorption is compared in Fig. 5.7 when the gratings have 1040 nm pitch and different duty cycles for TM and TE waves, respectively.

For TM waves, both the experimental and simulation results have multi-peak features. However, the experimental results showed smaller number of peaks. This is quite reasonable because two peaks may merge into one if both peaks are close to each other and broadened. Moreover, only when the grating duty cycle is 36% that the peak heights are comparable for experimental and simulation results. The peak heights of the experimental results are all lower than those of simulation results. This is in agreement with the simulation results in Chapter 3. It is worth noticing that the experimental results showed higher increase in absorption at wavelengths near 750 nm. This is because the experiments take the absorption increase in the whole OPV structure into consideration, while the simulation results only count for the absorption increase in the P3HT:PCBM layer. As discussed in more details in Appendix A, for wavelengths shorter than 730 nm, most of the absorption increase in the OPV structure is in the P3HT:PCBM. However, for longer wavelengths, as the absorption coefficient of P3HT:PCBM decreases dramatically, more of the absorption increase happens inside the Ag grating. So absorption peaks at shorter wavelengths are preferred.

In Fig. 5.4 and 5.6, the absorption increase for TE waves is monotonous from 430 nm and the increase is less than 20% at wavelengths longer than 650 nm. This suggests that there is little plasmonic activity for TE waves. When the OPV structure is added onto the gratings, an absorption peak is seen near 675 nm in Fig. 5.7 (a2), (b2) and (c2). This is

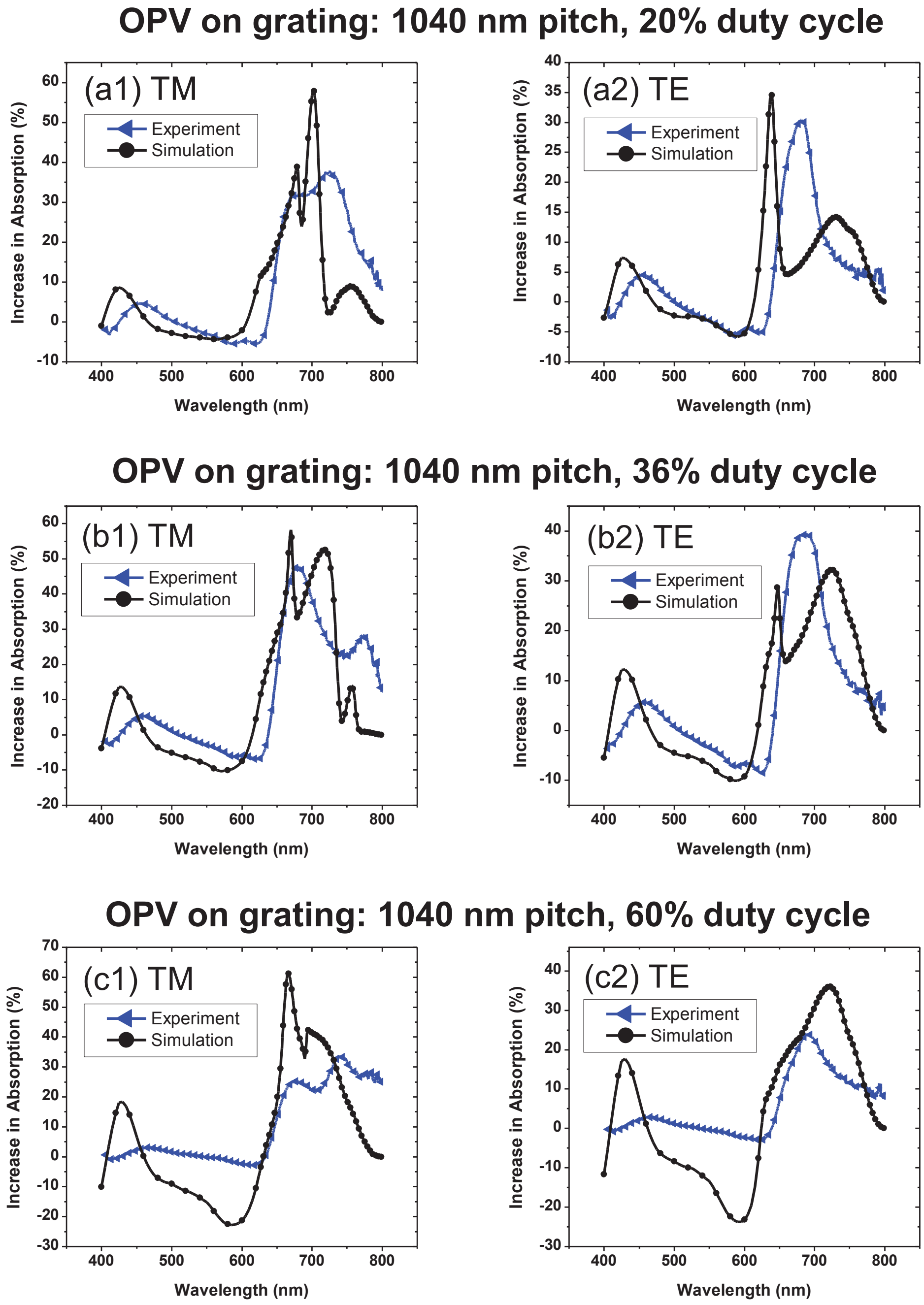

Fig. 5.7 Comparisons between experimental and simulation results for OPVs with grating of different duty cycles. The SPP absorption enhancement regions with multi-peak features are well matched for TM waves. For TE waves, simulation shows double peak while only one peak is seen from experiments due to the stringent experimental requirements needed for the guided mode resonance dip to show up.

because the incident light is coupled into waveguide modes in the OPV layers. However, simulation shows double peak for TE waves while only one peak is seen from experiments. This is because the dip between the two peaks in simulation curves is from guided mode resonance as discussed in section 3.5, which can easily be lost due to spectral broadening. Duty cycle of 36% is also the one with maximum peak height for TE waves.

It is also worth noticing that there is slight decrease in absorption at shorter wavelengths due to higher reflection when grating ridges are added. Especially for grating duty cycle of 60%, simulation results showed near 25% decrease in absorption near 600 nm. In experimental results, however, the decrease in absorption is less than 10%. This is possibly due to the stronger diffuse reflection at short wavelengths from the rough Ag surfaces.

The comparisons between experimental and simulation results for OPVs with 36% duty cycle and different pitches are shown in Fig. 5.8. Again, the SPP absorption enhancement spectral regions with multi-peak features are well matched for TM waves. For TE waves, single peak is shown in experiments rather than double peaks in the simulations. The experimental results also showed less decrease in absorption for wavelength shorter than 625 nm. This is because of local Ag clusters which will be able to act as small antennas supporting localized SPRs. This will be discussed in more details in section 5.2.2 and 5.2.3.

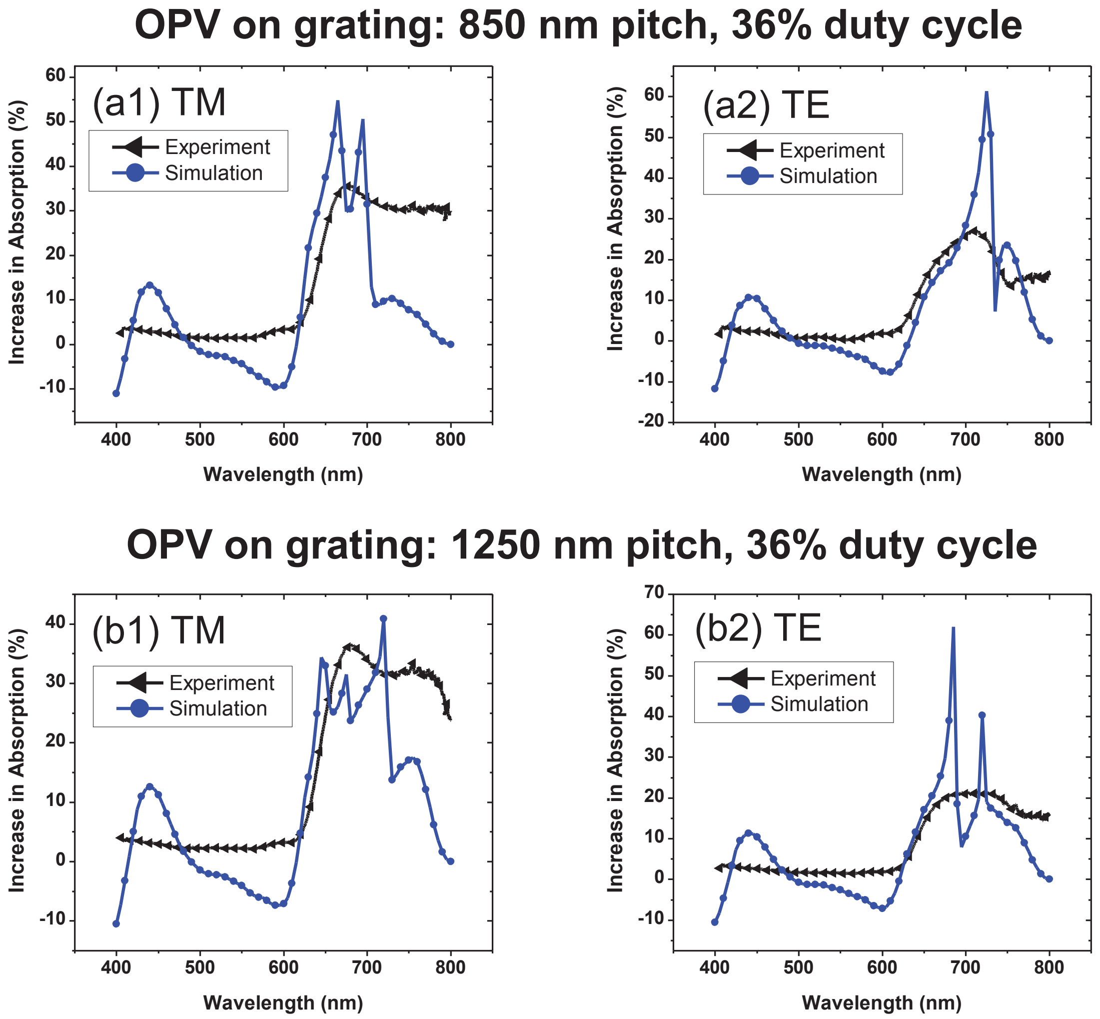

Fig. 5.8 Comparisons between experimental and simulation results for OPVs with grating of different pitches. The SPP absorption enhancement regions with multi-peak features are well matched for TM waves. For TE waves, simulation shows double peak while only one peak is seen from experiments due to the stringent experimental requirements needed for the guided mode resonance dip to show up.

5.2 Effect of the grating geometry on the absorption enhancement

As discussed in Chapter 3 that the absorption enhancement is very dependent on the grating height, duty cycle and pitch. Through optical measurements, we confirmed the impact of grating geometries on the absorption enhancement.

5.2.1 Effect of the grating height

The increase in absorption of OPVs is shown in Fig. 5.9 for gratings of height 25 nm and 55 nm, respectively. Both gratings have 1040 nm pitch and 36% duty cycle. The absorption peaks are well matched for TM waves in Fig. 5.9 (a) while the absorption enhancement for a shallower grating is greatly reduced. For TE waves, in addition to the decrease absorption enhancement from shallower gratings, there is a ~ 40 nm shift in the absorption peak. This is because when the grating height is changed, the effective index of the waveguide modes will change. Accordingly, the waveguide mode coupling wavelength is changed.

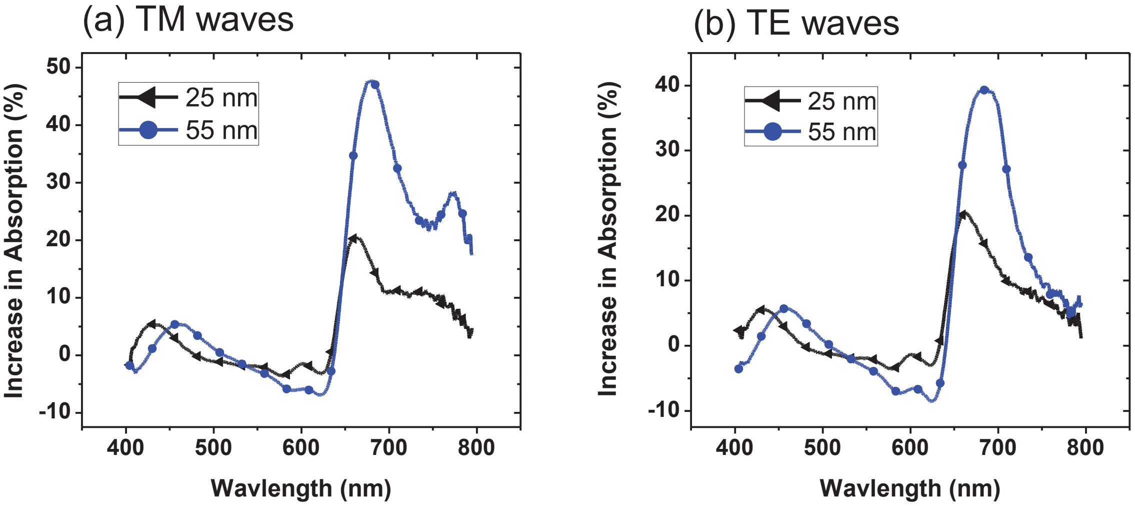

Fig. 5.9 For gratings with pitch of 1040 nm, duty cycle of 36% and different heights (25 nm and 55 nm), they showed similar features for TM waves (a) and TE waves (b), respectively. Higher grating caused larger increase in absorption.

We also tried to change the grating duty cycle when the grating height is 25 nm and the results are shown in Fig. 5.10. In contrast to the optimized 36 ~ 45% duty cycle for gratings of 55 nm height, the absorption enhancement keeps increasing as the grating duty cycle is increased. However, the 20-nm grating height limits achieving higher increase in the light absorption in general and adjusting the grating duty cycle cannot overcome the limit, as suggested by the overall low (< 25%) enhancement. This is much lower than that 60 nm-high gratings as shown in Fig. 5.9, which is 45 ~ 50%. As a result, we've chosen to use a higher grating, which is ~ 55 nm from AFM measurement.

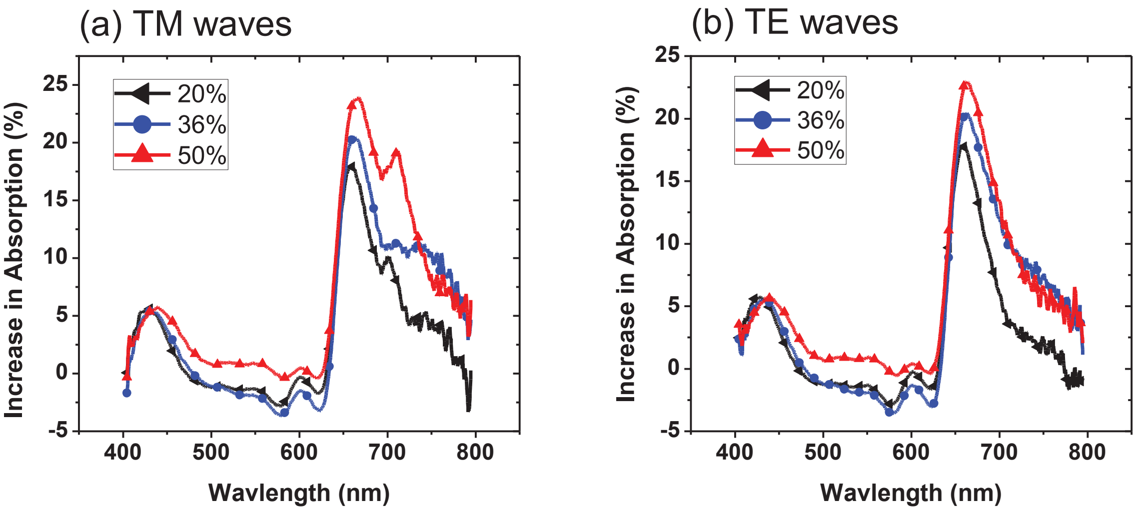

Fig. 5.10 With grating height fixed at 20 nm, the absorption increased with increasing duty cycle. However, the level of absorption increase achievable with 30 nm-high gratings was inherently limited and cannot surpass that from 60 nm-high gratings (shown in Fig. 5.9) even with adjustments in the duty cycle.

5.2.2 Effect of the grating duty cycle

As shown in Fig. 5.11, when gratings of 1040 nm pitch are added on the back of OPVs, gratings with duty cycles of 10% ~ 60% all showed higher absorption for wavelengths longer than ~ 650 nm for both TE and TM waves.

In Fig. 5.11 (a), 36% duty cycle shows higher peaks than 10% and 20% duty cycles. In Fig. 5.11 (c), even though the multi-peak feature gets more obvious when the duty cycle is 50% and 60%, 36% is more preferable for light absorption enhancement in OPVs. This is because 36% duty cycle offers higher peaks, especially at the short-wavelength side where most of the absorption increase is in the P3HT:PCBM layer and the carrier collection efficiency is higher. In Fig. 5.11 (b) and (d), the wavelengths of the enhancement peak for TE waves showed lower dependence on the grating duty cycle, which is in agreement with the simulation results in Chapter 3.

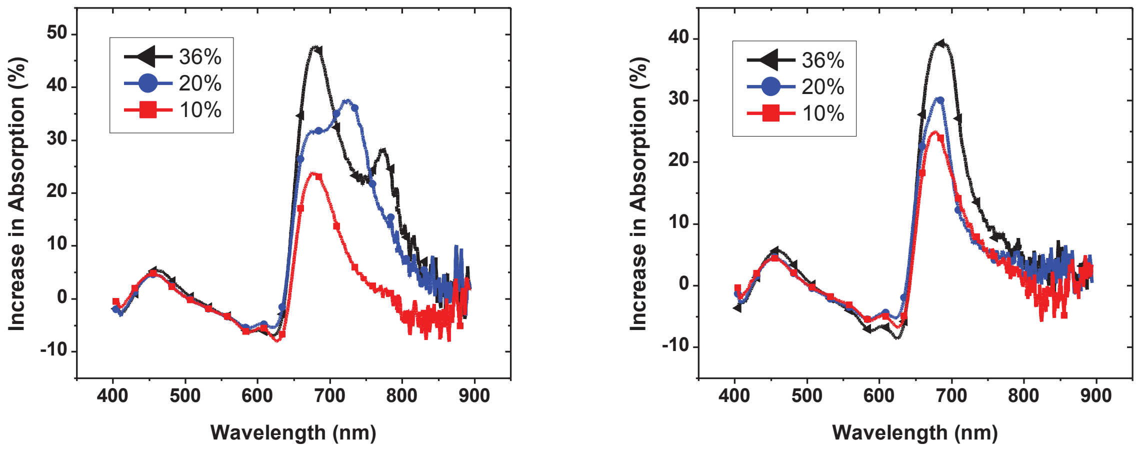
(a) TM, duty cycle 10~36%

(b) TE, duty cycle 10~36%

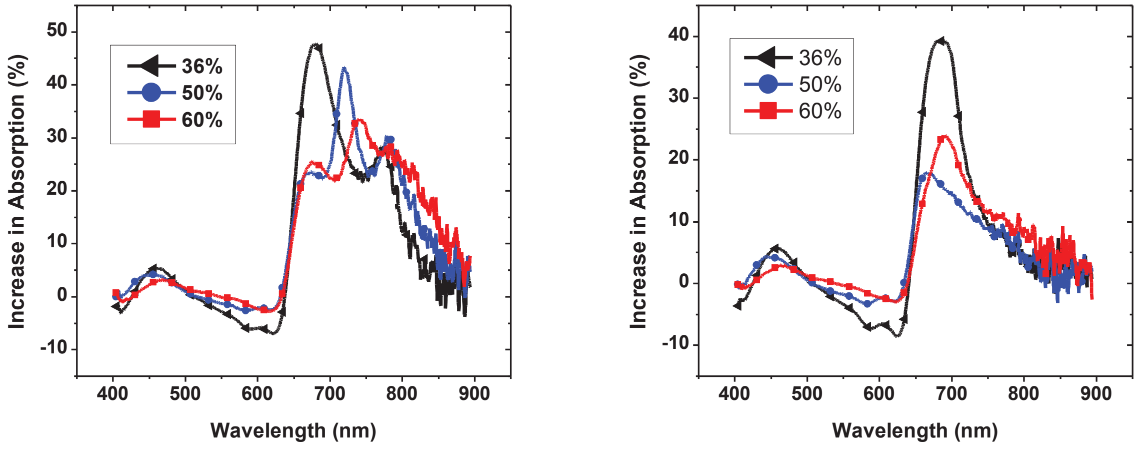
(c) TM, duty cycle 36~60%

(d) TE, duty cycle 36~60%

Fig. 5.11 The effect of the grating duty cycle on the light absorption enhancement for (a) and (c) TM waves and (b) and (d) TE waves.

More importantly, when the grating duty cycle is 36%, the absorption enhancement was most prominent for both TM and TE waves. The absorption at 675 nm increases from 35% to 82% for TM waves and 34% to 72% for TE waves, corresponding to 2.3X and 2.1X enhancements in absorption.

The simulation results in Chapter 3 suggests that the high *EF* band was achieved at the grating pitch 1040 nm and duty cycle of 35 ~ 45% for TM and the pitch 850 nm and duty cycle of 43% ~ 53% for TE waves. This is different from the simultaneous optimization of TM and TE enhancements at 36% duty cycle in Fig. 5.11. However, it is to our advantage that higher absorption enhancement is achieved. In Fig. 3.10 (a), the optimized grating duty cycle shifted to smaller value along the higher *EF* band when the grating pitch changes from 850 nm to 1040 nm. This could explain the simultaneous optimization of TM and TE enhancements at the same duty cycle.

The effect of the grating duty cycle on the light absorption increase in OPVs with gratings on the back is shown in Fig. 5.12, with data obtained from another sample rather than the one used for Fig. 5.11.

It is clear that 45% duty cycle shows the highest absorption enhancement for both TE and TM waves. For TM wave, though the SPR peaks are high for duty cycles of 25% and 55% at ~ 750 nm, 45% duty cycle is still more advantageous due to its broader enhancement spectral range and higher peak at shorter wavelengths, around which the carrier collection efficiency is higher. Compared with Fig. 5.11 (b) and (d), the absorption peaks in Fig. 5.12 (b) are much broader with several curves showing double peaks. This suggests that the incident light can be coupled to the waveguide modes at a wider spectral range. The only possible reason is that the incident light got diffracted by the gratings with

(a) TM waves

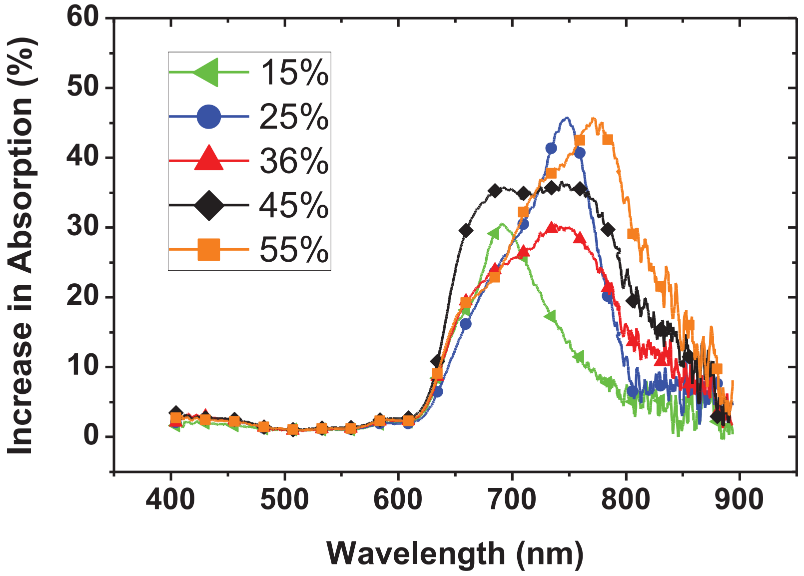

(b) TE waves

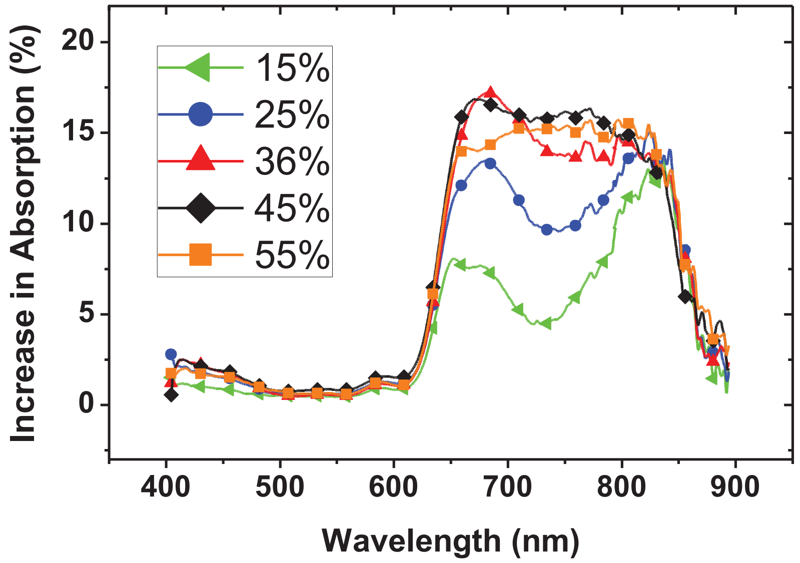

Fig. 5.12 The effect of the grating duty cycle on the light absorption enhancement for (a) TM waves and (b) TE waves. This result contrasts those in Fig. 5.11 which suggested the optimized duty cycle of 36%, 45% is the best for this sample for both TM and TE waves. This could be due to the differences between the features of the Ag grains in the two samples, as shown in Fig. 5.13.

more diffraction angle. Ag clusters as shown in Fig. 5.13 or irregularity of the grating ridges may contribute to increased diffraction.

The numerical simulation suggested two narrow regions of strong *EF* improvement for $900 < \Lambda < 1150$ nm: one at $D = 0.43$ which corresponds to the overlap between high EF_{TM} and EF_{TE} bands and the other at $D = 0.36$ along the lower edge of the high EF_{TM} as shown in Fig. 3.12. The results from two samples showed optimized grating duty cycle of 36% and 45%, respectively; both are in good agreement with the predicted region.

The comparison of the surface morphology of samples on two different substrates is shown in Fig. 5.13; with the samples on Substrate #1 correspond to the results in Fig. 5.11 and the samples on Substrate #2 Fig. 5.12.

It is obvious that Substrate #2 have bigger grain sizes and rougher surface. More importantly, many Ag clusters of 200~ 500 nm are present which can act as sources to scatter the incident light. As a result, samples on Substrate #2 have broader absorption enhancement peaks for both TE and TM waves. However, the peak values of the increase in absorption for the samples on Substrate #2 are smaller than that of samples on Substrate #1. The deposition rate and the impurities in Ag are responsible for the differences in the grain sizes [11, 86].

(a) Substrate #1

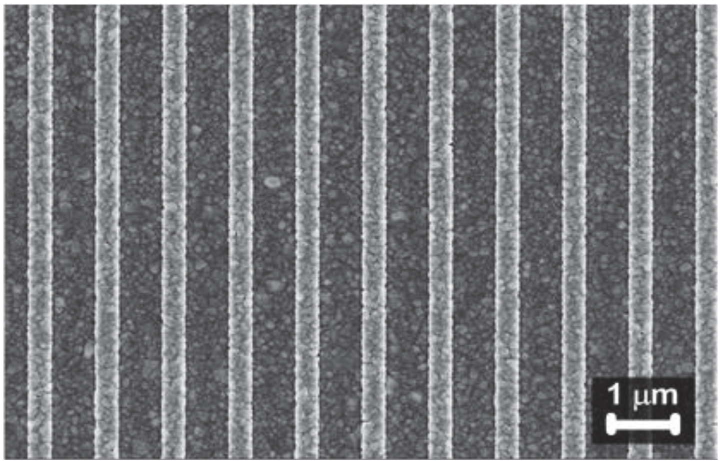

(b) Substrate #2

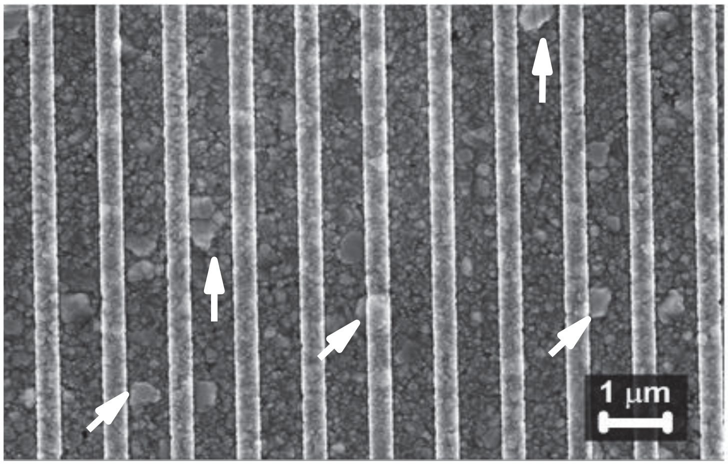

Fig. 5.13 The SEM images of gratings with pitch size of 1040 nm and duty cycle of 36%, Substrate #2 in (b) showed much larger Ag grains than Substrate #1 in (a). As marked with white arrows in (b), many Ag clusters of 200~ 500 nm are present, which contributes to the different spectra response of gratings with the same size.

As the duty cycle is the key factor to achieve higher increase in absorption, we also studied the tolerance for the duty cycle for samples on both Substrate #1 and #2. The results are shown in Fig. 5.14. For both substrates, the absorption enhancement for TE waves showed high tolerance for changes in the duty cycle. Samples on Substrate #1 show higher tolerance than those on Substrate #2 for TM waves. This may be the reason that the more grainy Substrate #2 has the optimized duty cycle at 45%, which is the overlap between high EF_{TM} and EF_{TE} bands; rather than 36%, which is the lower edge of the high EF_{TM}.

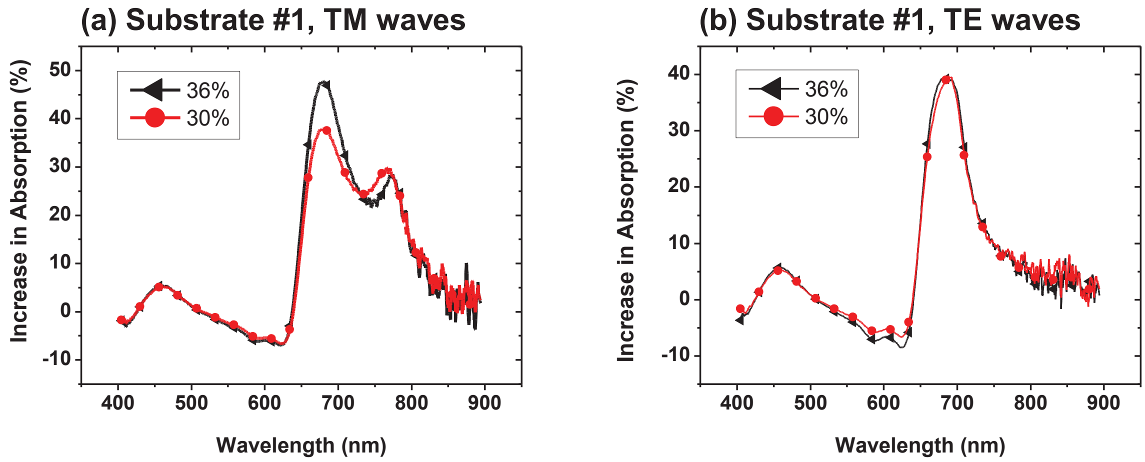

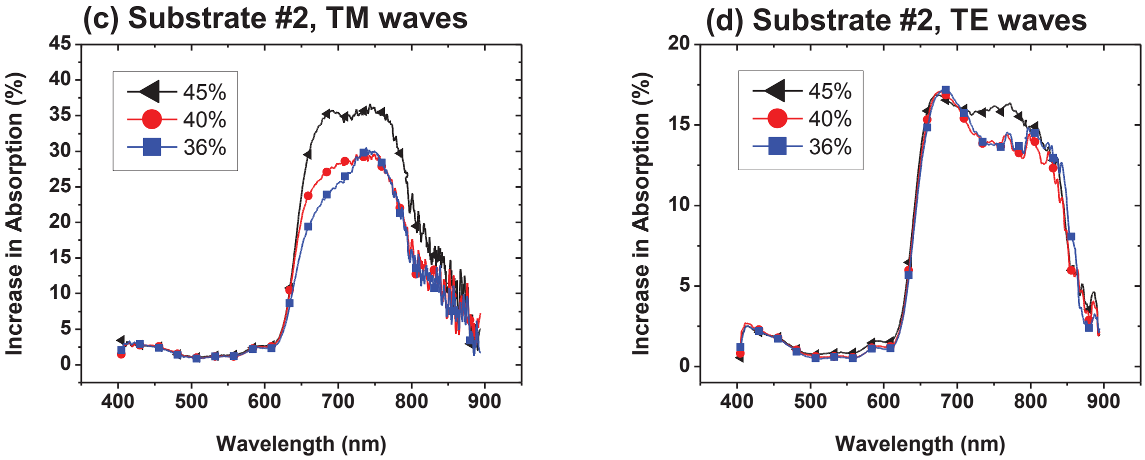

Fig. 5.14 The absorption enhancement's tolerance for the grating duty cycle. For both samples, TE waves showed higher tolerance than TM waves. Samples on Substrate #2, which has larger grains and rougher surfaces, has less tolerance than those on Substrate #1.

5.2.3 Effect of the grating pitch

To study the effect of the grating pitch on the light absorption enhancement, two sets of OPVs are tested, with grating duty cycle of 36% and 45%, respectively. All the OPV samples are on the same Substrate #2 as shown in Fig. 5.13 (b).

Figure 5.15 demonstrates the effect of the grating pitch on the increase in light absorption, when the grating pitch is fixed at 1040 nm. Under both TM- and TE- polarized light illumination, the pitch of 1040 nm is the best among 850 nm ~ 1250 nm. With TM-polarized incident light, the increase in absorption is not as sensitive to the changes in the pitch sizes as to changes in grating duty cycle. The increase in absorption shows higher dependence on the grating pitch since the absorption increase for TE waves is based on light diffraction and the resulting waveguide mode coupling.

When the grating duty cycle is 45%, the effect of the grating pitch on the increase in light absorption is shown in Fig. 5.16. Pitch size of 1040 nm has highest increase in absorption under TM wave illumination. As discussed in section 3.4, the optimized grating design for TM waves is 1040 nm pitch and 36% duty cycle. Compared with Fig. 5.15 (a), the fact that the gratings in Fig. 5.16 are not near the optimized design makes the TM response more sensitive to the changes in the grating pitch. With incident TE waves, however, 850 nm and 45% offers the best increase in absorption. This is in great agreement with the simulation results in section 3.5.

(a) TM waves, 36% duty cycle

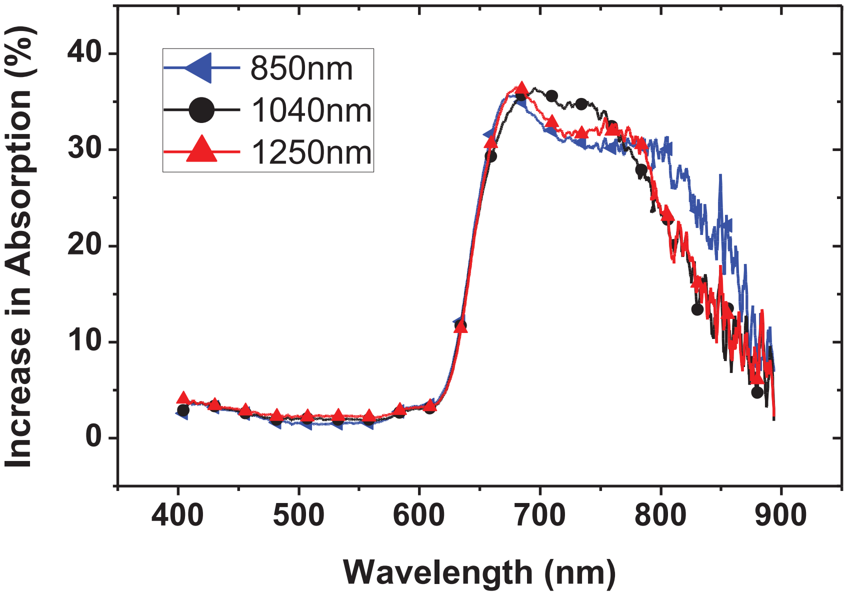

(b) TE waves, 36% duty cycle

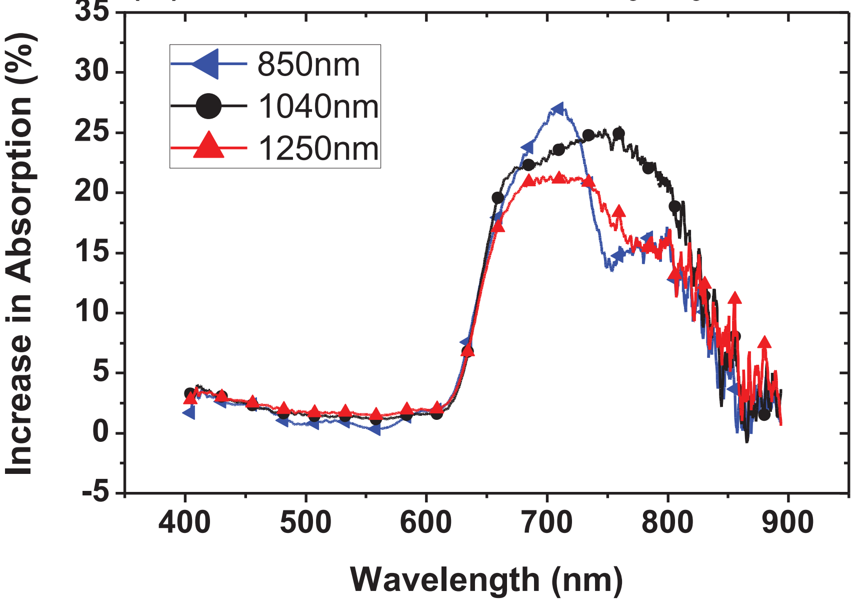

Fig. 5.15 With both (a) TM and (b) TE incident waves, 1040 nm pitch is the best among 850 nm ~ 1250 nm, when the grating duty_cycle is fixed at 36%. The light absorption enhancement for TE waves is more dependent on the changes in the grating pitches than that for TM waves.

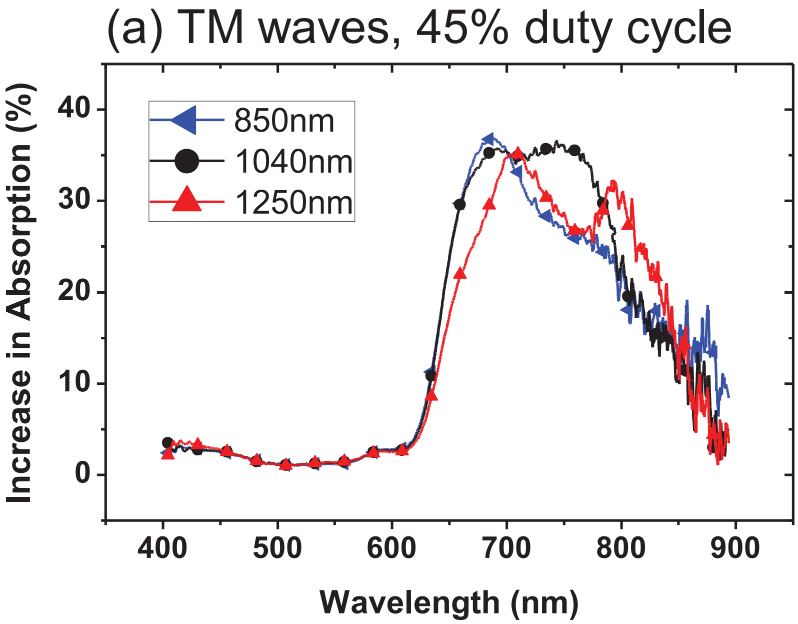

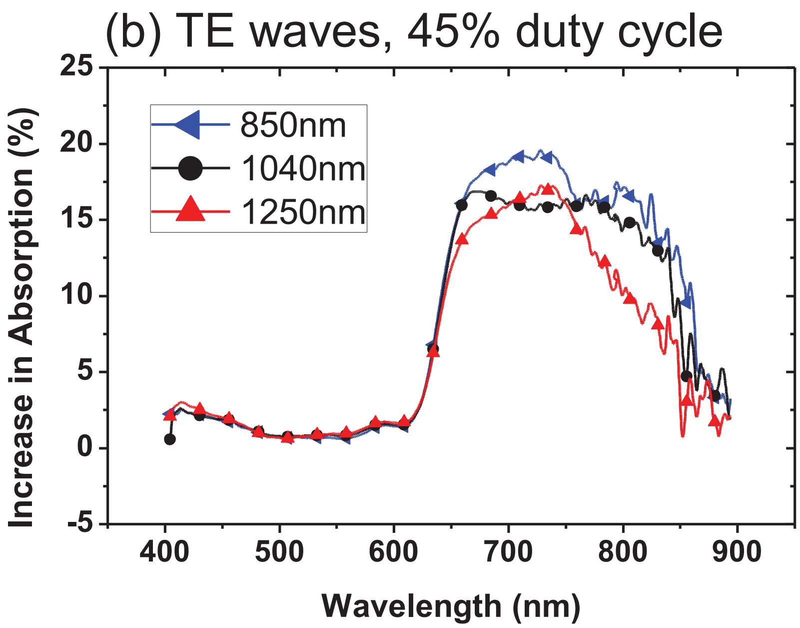

Fig. 5.16 The effect of the grating pitch on light absorption enhancement for (a) TM and (b) TE with the grating duty cycle fixed at 45%. 1040 nm pitch is the best for TM waves. With incident TE waves, 850 nm pitch and 45% duty cycles offers the highest increase in absorption, which is in agreement with the simulation results.

5.3 Polarization diverse absorption enhancement

In addition to the measurement under TE- and TM- polarized light illumination, the polarization angle was changed continuously between TE and TM to see if the absorption enhancement is truly independent on the polarization of the incident light. Two samples are tested with the results shown in Fig. 5.17 and Fig. 5.18, respectively. The results in Fig. 5.17 are from the grating design of pitch 1040 nm and duty cycle of 36% on Substrate #1, while results in Fig. 5.18 from the grating design of pitch 1040 nm and duty cycle of 45% on Substrate #2.

In Fig. 5.17 (a), the grating induced absorption increase from SPP modes is shown as a function of the polarization angle of the incident light. Clearly, there is no absorption peak for TE waves since surface plasmon resonances cannot be excited. The small peak at ~700 nm for bare gratings under TE illumination in both Fig. 5.17 (a) and 5.18 (a) is not clear, which does not show for other samples. When an OPV is made on top of the grating, light absorption enhancement can be achieved for both TM and TE waves from excitation of SPPs and waveguide modes, respectively. When the polarization angle is changed, this strong absorption enhancement is retained as shown in Fig. 5.17 (b). The increase in absorption for both bare gratings and OPVs is approximately linearly dependent on the polarization angle as:

$$\Delta Abs(\alpha) = (1-\alpha/90)\cdot\Delta Abs(TM) + \alpha/90\cdot\Delta Abs(TE) \tag{5.1}$$

Where α is the polarization angle of the incident light with $\alpha = 0$ defined as TM waves and $\alpha = 90$ defined as TE waves as shown in Fig. 4.8.

With a grating of 1040 nm pitch and 45% duty cycle underneath, the increase in absorption is measured for both the bare grating and the OPV structure on the grating. The results are shown in Fig. 5.18.

(a) Bare Ag Grating

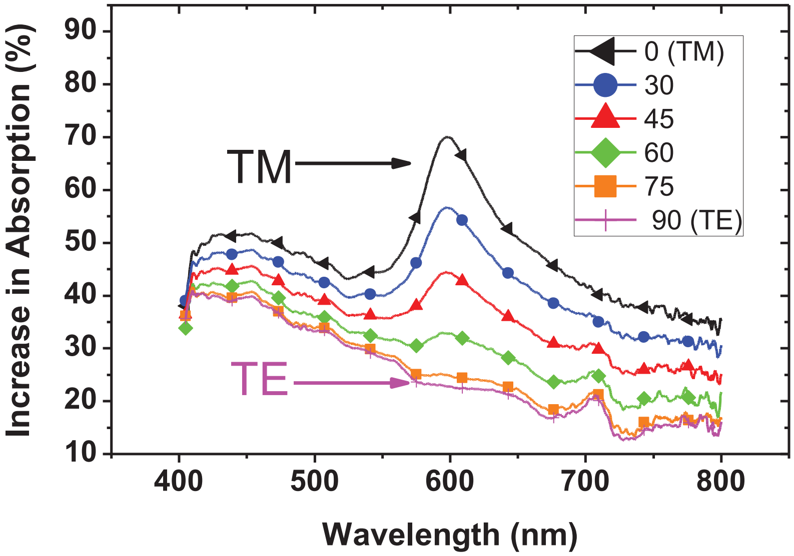

(b) OPV on Ag Grating

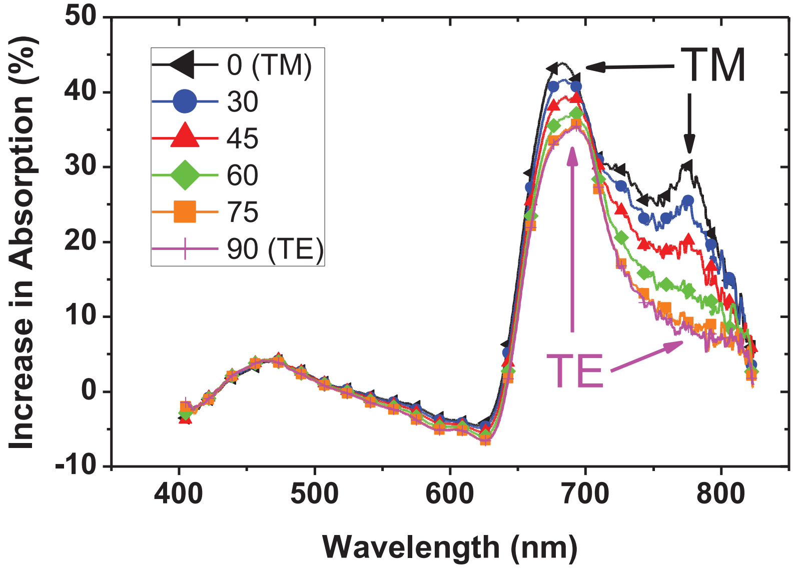

Fig. 5.17 For the grating design of pitch 1040 nm, duty cycle 36%, the effect of the polarization angle on the absorption enhancement is shown for (a) a bare Ag grating and (b) with OPV structure on top of the Ag grating. SPP-based absorption enhancement is prominent only for TM waves in (a), while comparable increase in absorption is present for all polarization angles in the OPV on Ag grating (b).

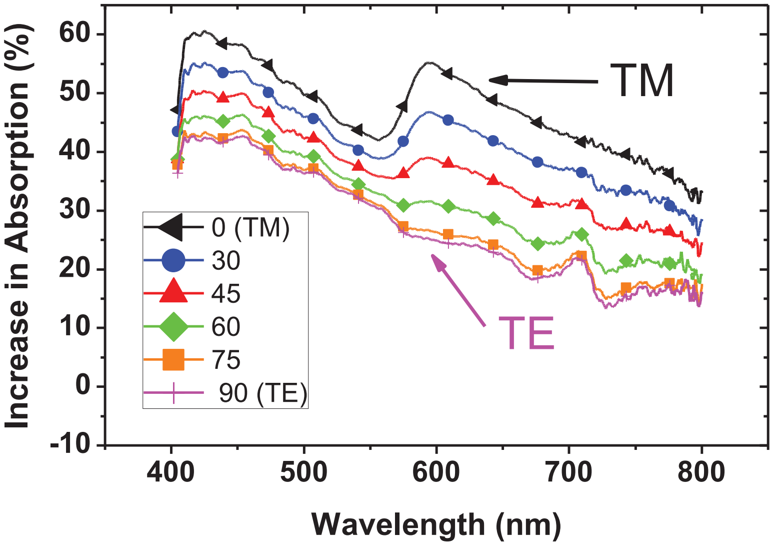

(a) Bare Ag Grating

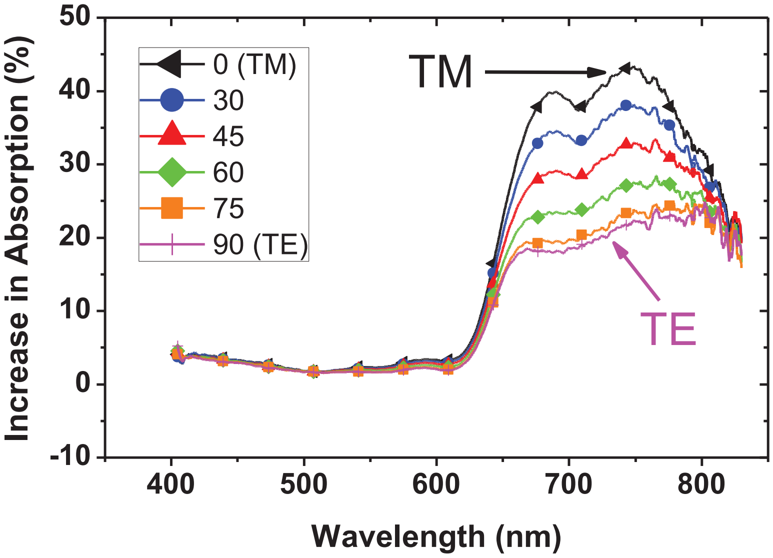

(b) OPV on Ag Grating

Fig. 5.18 For the grating design of pitch 1040 nm, duty cycle 45%, the effect of the polarization angle on the absorption enhancement is shown for (a) a bare Ag grating and (b) a OPV on the Ag grating. Plasmonic absorption peaks are prominent only for TM waves in (a). The increase in absorption is present for all polarization angles in the OPV (b), but the increase for TE waves is significantly lower that for TM waves due to large Ag grains.

Similarly, for the bare silver grating, the results in Fig. 5.18 (a) only showed SPP-based plasmonic peaks for incident light with polarization angle smaller than 45 degrees and thus with large TM components. With the OPV structure made on the gratings, absorption enhancement is present for both TE and TM waves. However, since the silver grating used for this sample has large grains and rough surface, the absorption enhancement for TE waves is significantly smaller than that for TM waves. Therefore, though the increase in absorption is present for all polarization angles in the OPV, it is quite dependent on the light polarization angle. This also suggests that better control over the grating morphology is required to achieve stable performance on the light absorption enhancement.

Chapter 6. OPV devices

In this thesis, several device architectures of P3HT:PCBM based OPVs are studied for comparison purposes. These devices will be grouped into "substrate type" and "superstrate type" depending on whether opaque or transparent substrates were used [4], as schematically shown in Fig. 6.1. In the "superstrate" design, sunlight enters through the transparent substrate, which is commonly glass or transparent plastic. On the top of this insulating substrate, we need to install a conducting electrode, which is typically made of "transparent conductive oxide" (TCO) such as ITO [4]. Followed by the photoactive layers, a thick metal layer is deposited onto the device as a back reflector and electrode. In the "substrate" design, PVs are fabricated in this order: on the substrate first a back reflector and electrode, then the photoactive layer, and finally a TCO layer on the topmost to act as an electrode as well as a window allowing light to path through [4]. And the light enters the PV device before it reaches the substrate.

P3HT:PCBM OPVs are mainly superstrate type [33], while the proposed OPV in this thesis, shown in Fig. 3.2, is a substrate type solar cell. For OPVs, terms like "traditional" and "inverted" devices are used, depending on the design of the electrodes. For a traditional device, the cathode is exposed to the air while the anode is the one next to the substrate; for an inverted device, the anode is exposed to the air side.

The materials used are: P3HT (P#200) from Rieke Metals, PCBM from nano-C. The P3HT and PCBM mixture solution is made by firstly dissolving P3HT in 1,2-dichlorobenzene and then filtering the P3HT solution with Millex PTFE filters (pore size 0.22 μm) and mixing it with PCBM powder. The mixed solution is stirred for at least 12 hours before using. The weight ratio between P3HT and PCBM is 1 and the total concentration is 30 mg/mL. PEDOT:PSS (1:6 weight ratio, 1.3 ~ 1.7% in water) was from H.C. Starck. Cs_2CO_3 (99.9%) from Alfa Aesar, MoO_3 (99.99%) from Sigma Aldrich, V_2O_5 (98+%) from Acros Organics are also used in different devices. The 20 nm Ag particle colloid (15705-20SC with 7.0×10^{10} particles/mL) used in section 6.3 is from Ted Pella, Inc.

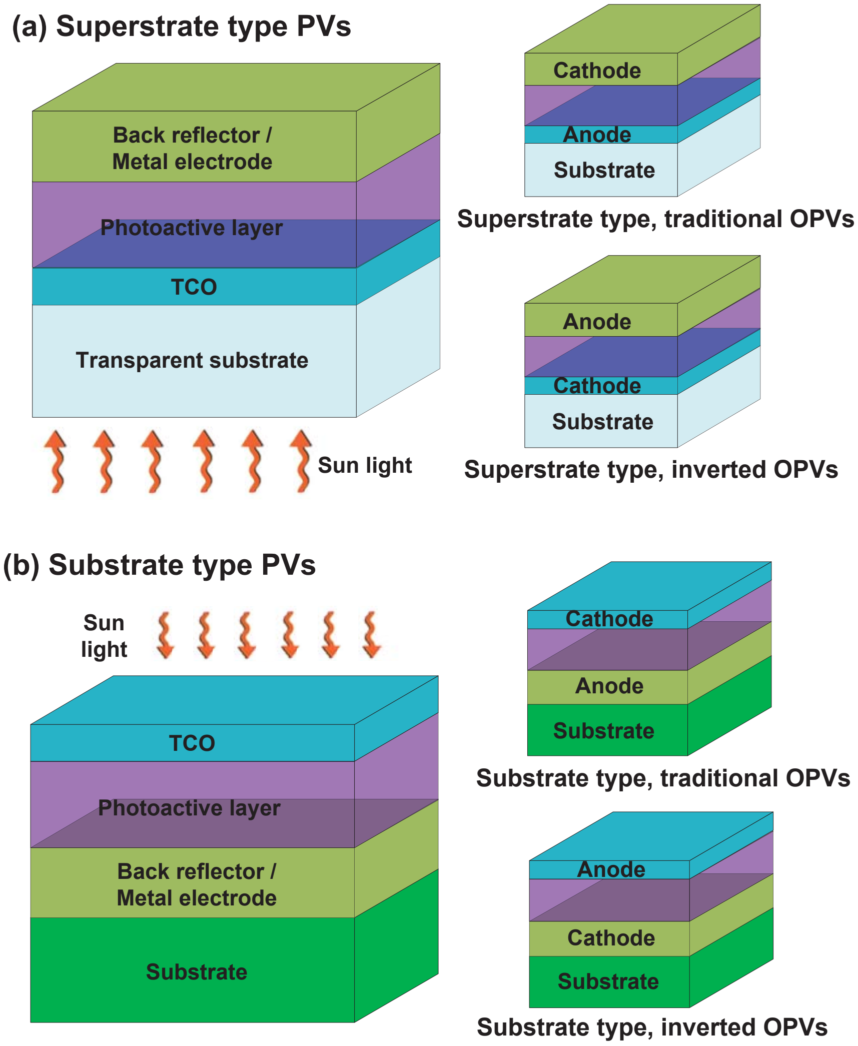

Fig. 6.1 Schematically illustration of the substrate and superstrate type solar cells with light incident from different side of the PVs. "Traditional" and "inverted" OPV devices with different designs of electrode are also shown.

6.1 Superstrate type OPVs

6.1.1 Superstrate type traditional OPVs

Both the traditional and inverted OPVs with the superstrate type design have been fabricated. The schematic structure of the traditional device and the corresponding energy diagram are shown in Fig. 6.2, with ITO/PEDOT:PSS as the anode and Ca/Al as the cathode.

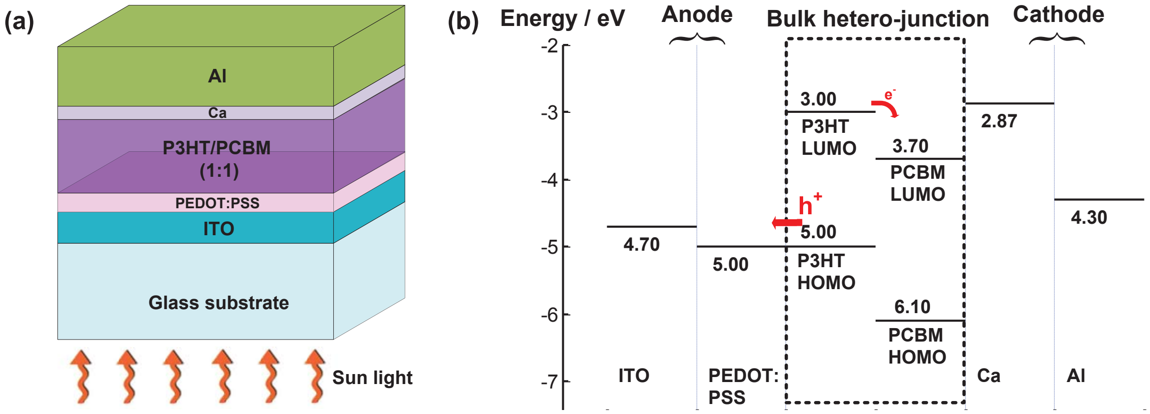

Fig. 6.2 (a) Schematic view of the superstrate type traditional OPV with (b) showing its energy band diagram. ITO/PEDOT:PSS is the anode, colleting holes from the doner P3HT; Ca/Al is the cathode, collecting electrons from acceptor PCBM.

ITO coated glass substrate is firstly cleaned in ultrasonic baths of surfactant for 15 min, water for 4 times and each 5 min, followed by iso-propanol (IPA), acetone and another IPA baths each 5 min. A 5 min air plasma treatment is applied to the substrate before the device fabrication. This solvent cleaning and plasma treatment is referred to as the standard cleaning procedure. The PEDOT:PSS layer is made by spin coating at 5000 rpm for 60 sec and then annealed at 120 °C for 30 min in ambience. Spin coating of the P3HT:PCBM layer is done in the glovebox at 400 rpm for 60 sec and then the samples are kept in covered petri dishes to allow the slow evaporation of 1,2-dichlorobenzene. After drying for 1.5 ~ 2 hours, the P3HT:PCBM film is annealed. The annealing condition has an important impact on the device performance. 25 nm Ca and 100 nm Al are thermally evaporated in a vacuum chamber ($\sim 1 \times 10^{-6}\ torr$) with evaporation rate of 0.6 Å/sec and < 3 Å/sec, respectively.

The thermal annealing condition for the P3HT:PCBM film, which affects the phase transitions of the two materials and the morphology of the blend, has been intensively investigated [49, 51, 87]. In general, the optimum temperature is below 150 °C and higher temperature degrades the device [87]. I found that starting with a high temperature and annealing the samples with the temperature ramping down increases the V_{OC} without degrading other characteristics. Instead of using constant temperature annealing (110 °C, 12 min), the polymer film is firstly annealed at 160 °C for 1 min and then the temperature of the hot plate is set at 110 °C with the total annealing time still fixed at 12 min. As a result, the polymer film will experience a decreasing temperature, which is 160 °C at the beginning and stabilizes at 110 °C in the middle of the 12 min.

The OPVs area $A = 0.11\ cm^2$ and the current density is calculated as $= I/A$. The JV characteristics of two devices are measured with an ELH bulb with the light intensity set at $100mW/cm^2$ and shown in Fig. 6.3. Table 6.1 summarizes the device characteristics.

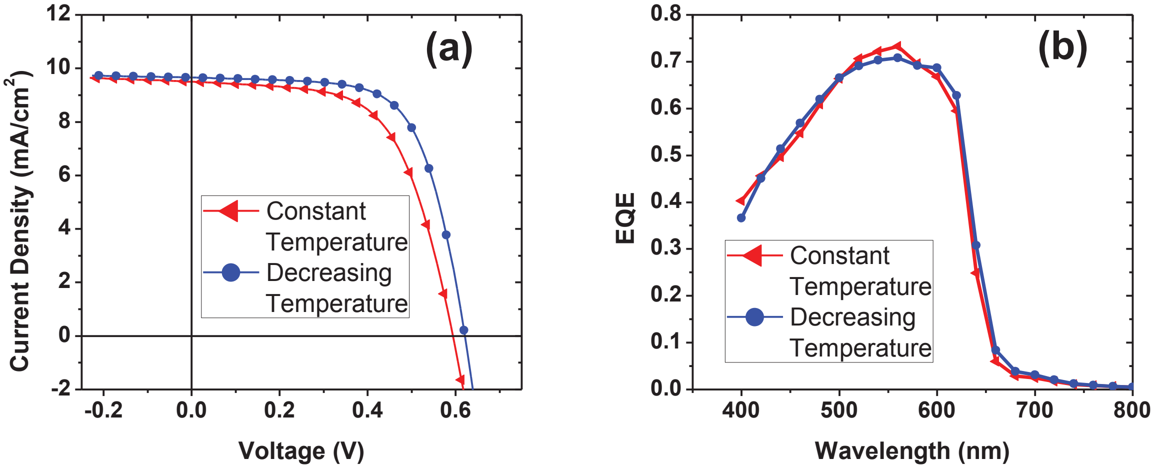

Fig. 6.3 Traditional OPVs: (a) JV curves showing a better device performance with annealing conditions changed. (b) the EQE curves are very similar for the two devices, which is in agreement with the comparable J_{sc}.

Table 6.1 Device characteristics of traditional OPVs with different annealing conditions

Device	Annealing	V_{OC} (V)	J_{SC} (mA/cm^2)	FF (%)	η (%)
(1)	110 °C	0.595	9.5	61.3	3.45
(2)	160 -> 110 °C	0.622	9.6	67.4	4.03

From the JV curves and Table 6.1, the improvement in the PCE is clearly from the higher V_{OC} and the corresponding increase in FF. The external quantum efficiency (EQE) measurement is another important characterization method for PVs. The wavelength dependent EQE is measured with monochromatic light sources. EQE evaluates how well the solar cell converts incident photons to electrons which can reach the external load. The integration of EQE over the solar spectrum also gives the photocurrent density J_{SC}, which should consistent with the results from IV measurements. The EQE of the two devices are plotted in Fig. 6.3 (b), showing very similar curves, which are in agreement with the comparable values of J_{SC} in Table. 6.1.

6.1.2 Superstrate type inverted OPVs

The schematic structure of the superstrate-type inverted OPV and the corresponding energy diagram are shown in Fig. 6.4, with ITO/Cs_2CO_3 as the cathode and MoO_3 (or V_2O_5)/Al as the anode. Both the MoO_3 and V_2O_5 can be used as a hole extraction layer thanks to their deep valence band which matches the HOMO level of P3HT well. Then band energy of MoO_3 is shown in the energy diagram. The CB and VB energy of V_2O_5 are 2.4 eV and 4.7 eV, respectively [45, 88].

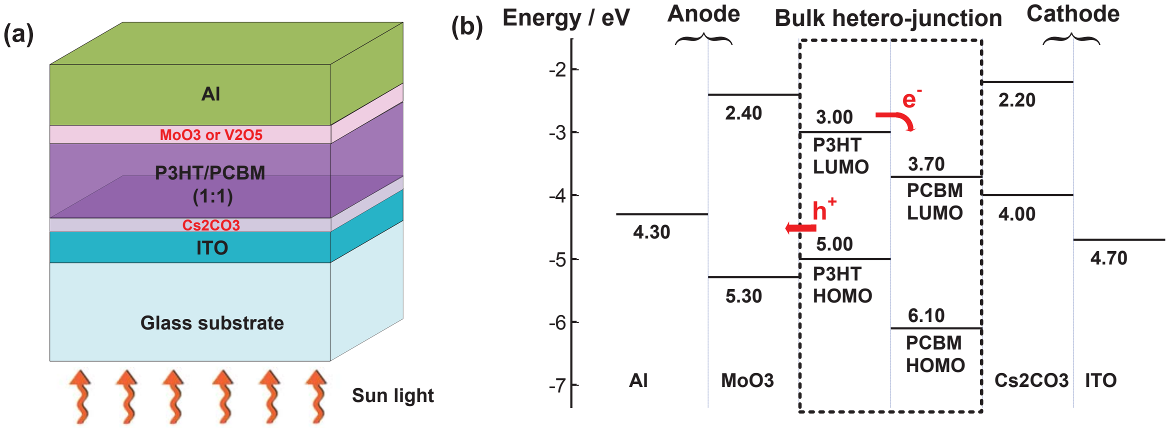

Fig. 6.4 (a) Schematic view of the superstrate type inverted OPV with (b) showing its energy band diagram. ITO/Cs_2CO_3 is used as the cathode, while both MoO_3 and V_2O_5 can be used at the anode side for efficient hole extraction.

For all the superstrate type OPVs with inverted electrodes, the devices were fabricated through the following steps: (1) standard cleaning of the ITO coated glass as described before; (2) the spin coating (from a 0.2 wt% Cs_2CO_3 solution in 2-ethoxyethanol) or the thermal evaporation (0.2~0.3 Å/sec) of a thin Cs_2CO_3 layer, followed by annealing at 160 °C for 20 min in the ambient; (3) the spin coating of the active layer P3HT:PCBM at 400 rpm for 60 sec with a 30 mg/mL P3HT:PCBM in 1,2-dichlorobenzene, followed by the annealing; (4) the thermal evaporation of the hole extraction buffer layer, *i.e.* V_2O_5 or MoO_3 with a evaporation rate of 0.3~0.5 Å/sec; (5) the evaporation of a 100 nm Al at a rate less than 3 Å/sec.

The thicknesses of the electron extraction (Cs_2CO_3) and hole extraction (V_2O_5 or MoO_3) layers impose a huge impact on the device IV characteristics and thus on the PCE. For the Cs_2CO_3 layer, devices with spin coated films and thermally evaporated films were compared. For spin coated films, the optimized spinning condition is at 4000 rpm for 60 sec. For thermally evaporated Cs_2CO_3 films, the optimized thickness is 2 nm. The optimized thicknesses for V_2O_5 and MoO_3 layers are 10 nm and 15 nm, respectively.

The IV characteristics of several inverted devices with different electrodes are listed in Table 6.2.

Table 6.2 Device characteristics of several superstrate-type inverted OPVs

Device #	**Cs_2CO_3 layer**	**Hole extraction layer**	V_{OC} (V)	J_{SC} (mA/cm^2)	FF (%)	η (%)
(a)	**Spin coating**	15 nm MoO_3	0.562	9.30	59.4	3.11
(b)	**Spin coating**	10 nm V_2O_5	0.576	9.50	55.4	3.03
(c)	**Evaporation (2 nm)**	15 nm MoO_3	0.522	8.43	50.7	2.23

It is clear that the efficiency of the inverted devices is lower than that of traditional devices, which is also reported in the literature [42, 45, 68, 88]. Yet the inverted OPVs exhibit longer lifetime. This is because inverted OPVs are PEDOT:PSS free, which is acidic and causes damage to the ITO electrode over time. The oxidation of the electrode can also be prevented by placing the low work function cathode on the substrate side.

In addition to their better stability, the inverted OPVs also allow shallower penetration depth for SPR modes. Placing metallic paticles or nanostructures right next to the photoactive layer is not advisable since metallic structures can act as recombination centers and may cause shorting of the devices. As a result, metallic particles or nanostructures are commonly added into the electrode buffer layers of the OPV structures [5, 15], the PEDOT:PSS layer for example. The PEDOT:PSS layer in the traditional devices is normally between 50 to 100 nm, which acts as a spacer layer between the plasmonic structures and the photoactive layer. My simulation results suggest that inside the P3HT:PCBM layer, the penetration depth of SPR modes is less than 150 nm. Therfore, a PEDOT:PSS layer is too thick and will prevent the locally enhanced electromagnetic field from reaching the photoactive layer. In contract, the Cs_2CO_3 in inverted devices is not a continuous film and let the SPR fields act on the photoactive layer directly.

6.2 Substrate type inverted OPVs

Due to the opaqueness of Ag gratings, the proposed OPV in Fig. 6.5 (a) is substrate type inverted OPV with the grating functioning as the back reflector. Its energy diagram is shown in Fig. 6.5 (b).

The fabrication of devices without the grating and with light incident from the top is the first step toward the realization of the proposed OPV. Instead of device Glass / ITO / Cs_2CO_3 / P3HT:PCBM / MoO_3 / Al in Fig. 6.4 (a), I made device on a planar Ag coated glass substrate: Glass / Ag / Cs_2CO_3 / P3HT:PCBM / MoO_3 (or V_2O_5) / ITO (as shown in

Fig. 6.6 (a)) with ITO as the the topmost transparent electrode.

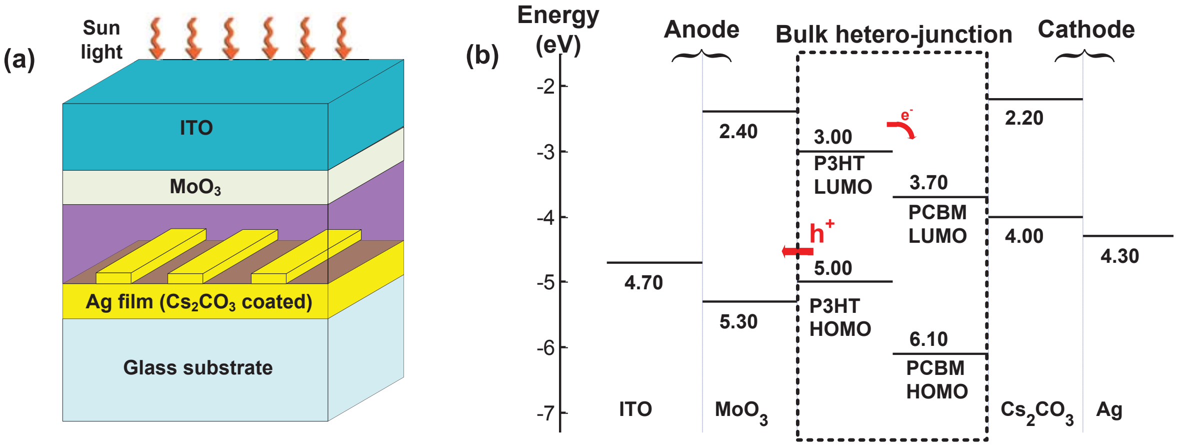

Fig. 6.5 (a) Schematic view of the substrate type inverted OPV with a Ag grating as the back reflector and light trapping scheme. (b) The energy diagram of the device.

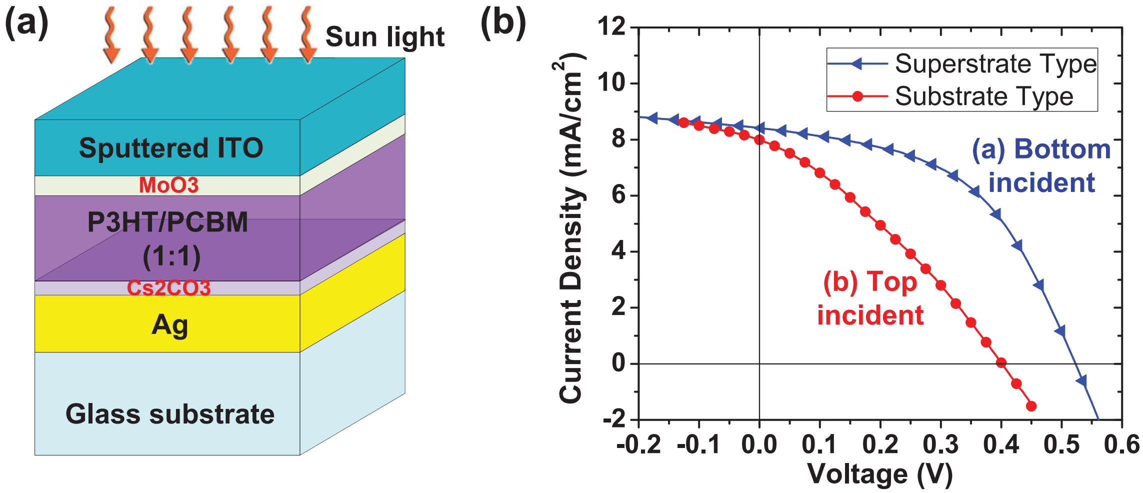

Fig. 6.6 (a) The substrate type inverted OPV on a planar Ag coated glass substrate. (b) JV curve of the best substrate type device ($\eta = 1.11\%$) is plotted (red curve). A 120 nm ITO and a 15 nm MoO_3 consist the anode, a 2 nm thermally evaporated Cs_2CO_3 layer and a 100 nm Ag layer consist the cathode. For comparisons, the JV characteristic of the superstrate type device with light incident from the bottom is also superposed (the blue line).

The glass substrate is cleaned following the standard procedure. Then a 100 nm Ag film is thermally evaporated onto the substrate with a rate starting from 0.3 Å/sec and increasing during the evaporation. The rate was kept below 4 Å/sec throughout the evaporation. The ITO layer is sputtered using 20W RF power at 2 mTorr for 20 minutes. The sputtering rate is ~ 1 Å/sec, leading to a total ITO thickness of 120 nm. The rest of the fabrication is the same as described for the superstrate type inverted OPVs.

For this structure, different combinations of electrodes from thermally evaporated or spin-coated Cs_2CO_3 and thermally evaporated V_2O_5 or MoO_3 are tested. During the IV measurement, the probe casts shadow on the device partially blocking the light incident from the top. Therefore, the effective solar cell area becomes $A = 0.08\ cm^2$ instead of $A = 0.11\ cm^2$. The best substrate type device ($\eta = 1.11\%$) was obtained with a 2 nm thermally evaporated Cs_2CO_3 layer and a 15 nm MoO_3 layer. The corresponding JV curve is plotted in Fig. 6.6 (b) in red. The JV characteristic of the superstrate type device with light incident from the bottom is also superposed for comparisons (the blue line).

Table 6.3 summarizes several substrate type devices together with a reference superstrate-type device. Device (a) and (b) have a 2 nm Cs_2CO_3 and a 15 nm MoO_3, both from thermal evaporation. Device (c) and (d) have the same structure: Glass / 100 nm Ag / Cs_2CO_3 (spin coated) / P3HT:PCBM / 10 nm V_2O_5 (evaporated)/ 120 nm ITO.

From Table 6.3, the most prominent problem of the substrate type devices is the low V_{OC} and FF. Another problem is the non-consistent PCE, as suggested by the different η for the same devices (c) and (d). The EQE plots for the four devices in Table 6.3 are shown in Fig. 6.7. Compared with device (a), device (b) suffered low EQE at 400 ~ 500 nm. Since the anode is at the light incident side, this suggests an electron collection problem. However, EQE is in general quire low for device (c) and (d). The problem is especially prominent for 475 ~ 625 nm. The low EQE, together with low V_{OC} indicate poor carrier extraction.

Table 6.3 Substrate-type inverted OPVs

Structure Type	**Device #**	V_{OC} (V)	J_{SC} (mA/cm^2)	FF (%)	η (%)
Superstrate	**(a)**	0.522	8.43	50.7	2.23
Substrate	**(b)**	0.400	8.07	32.3	1.11
	(c)	0.254	6.70	35.6	0.61
	(d)	0.376	7.41	38.9	1.08

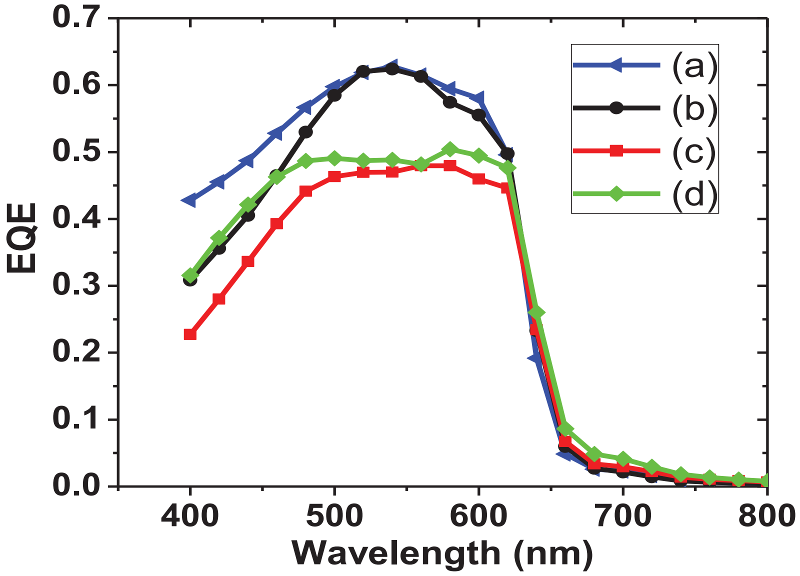

Fig. 6.7 EQE curves of the devices in Table 6.3. Device (a) is superstrate type with light incident from the bottom and Devices (d) ~ (d) are substrate type. Device (b) is the best substrate type device obtained, while device (c) and (d) suffered poor carrier collection in the absorption band of P3HT:PCBM.

To identify the causes of the carrier collection problem, two sets of testing devices were made as depicted in Fig. 6.8. The structure in Fig. 6.8 (a) is used to test the MoO_3/ITO anode and the structure in Fig. 6.8 (b) is used to test Ag as a cathode material.

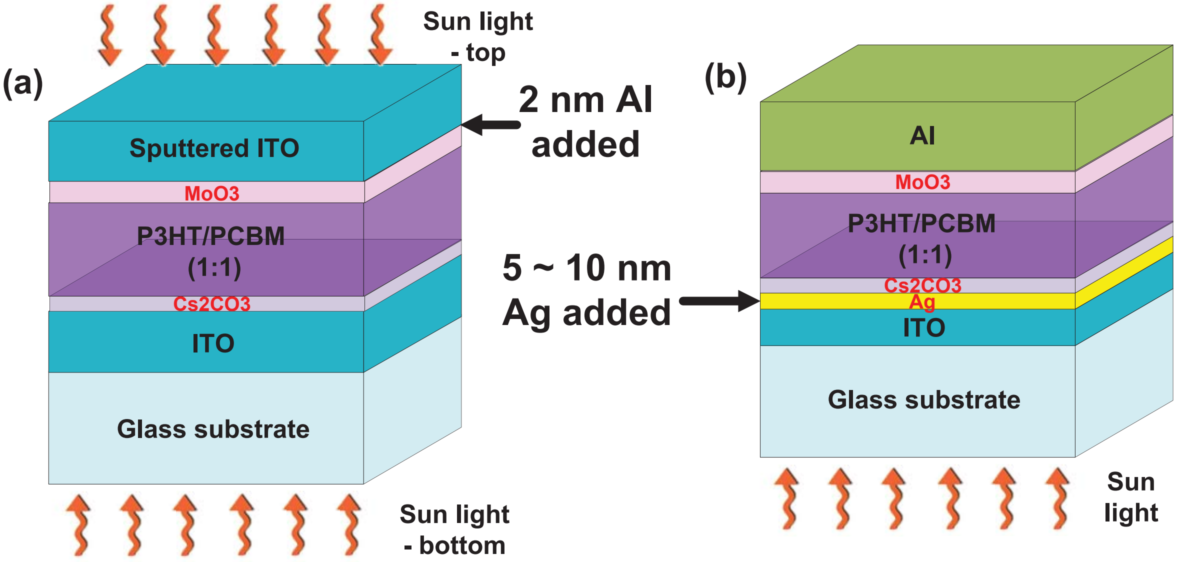

Fig. 6.8 Two types of devices for testing the problems of the substrate type device in Fig. 6.6 (a). (a) is used to test the anode. A 2 nm Al added between ITO and MoO_3 will significantly help the OPV PCE. (b) is used to test the Ag/ITO anode, adding a Ag layer between Cs_2CO_3 and ITO lowered the V_{OC}.

For the device in Fig. 6.8 (a), I started with a semitransparent device Glass / ITO / Cs_2CO_3 / P3HT:PCBM / MoO_3 / sputtered ITO for which the ITO / Cs_2CO_3 works good as a cathode. Table 6.4 summarized the JV characteristics of the semitransparent device with both top and bottom light incident. When the anode is 15 nm MoO_3 + ITO, the device suffered poor V_{OC} as well as J_{SC}. Since a thick Al layer (> 100 nm) on top of the MoO_3 works well as an anode, as suggested by the superstrate type devices in Fig. 6.4 and their device performance in Table 6.2, I tried to add a 2 nm Al between the MoO_3 and ITO. By adding the 2 nm Al, the V_{OC} increases by 1.8 times and the current increases by 2.3 times for light incidenting from both directions.

Table 6.4 Semitransparent OPVs for testing the sputtered ITO electrode

Structure	**Light incident**	V_{OC} (V)	J_{SC} (mA/cm^2)	FF (%)	η (%)
15 nm MoO_3 + ITO	bottom	0.335	2.63	31.1	0.27
	top	0.296	1.02	75.3	0.08
15 nm MoO_3 + 2 nm Al + ITO	bottom	0.613	5.78	25.3	0.90
	top	0.551	2.41	75.3	0.33

To test the Ag electrode, I started with the device in Fig. 6.8 (b): Glass / ITO / 2 nm Cs_2CO_3 / P3HT:PCBM / MoO_3 / Al. Then 5 nm and 10 nm Ag layers were added between ITO and Cs_2CO_3 in the two devices, respectively. Table 6.5 compared the JV characteristics of these three devices. As the Ag layer is added and its thickness is increased, the J_{SC} drops dramatically. This is due to the limited transmission of Ag films as well as the jeopardized carrier collection, as suggested by the lower V_{OC}.

Table 6.5. OPVs for testing the Ag electrode

Structure	V_{OC} (V)	J_{SC} (mA/cm^2)	FF (%)	η (%)
w/o Ag layer	0.522	8.43	50.7	2.23
w/ 5 nm Ag	0.423	4.146	48.7	0.85
w/ 10 nm Ag	0.433	2.378	44.9	0.46

In conclusion, to effectively increase the PCE of substrate type inverted OPVs, both the MoO_3 / ITO anode and the Ag / Cs_2CO_3 cathode need to be modified for good V_{OC} and efficient carrier extraction. For the anode, a 2 nm Al layer between the MoO_3 and ITO is enough to adjust the work function. For the cathode, most likely a ITO layer as thin as 2 nm is required. This buffer layer between ITO and Cs_2CO_3e must be very thin though; otherwise it will partially block the plasmonic effect for light absorption enhancement. However, due to the non-consistent PCE for repeated experiments, the integration of Ag gratings and OPVs has not been investigated. To improve the device repeatability, well-controlled experimental environment is needed. Another important issue is the Ag coated substrate, for which the control of grain sizes, surface morphology and surface cleaning all have great impact on the final solar cell performance.

6.3 Ag nanoparticles in superstrate-type inverted OPVs

As discussed in Section 2.4.1, a natural question on the use of nanoparticles in OPVs to enhance light absorption is whether the plasmonic effect can further benefit devices that already have high light absorption or not. To investigate this question, I tried to use Ag particles in the superstrate type inverted OPV. The structure is similar to the one shown in Fig. 6.6 (a) with Glass / ITO / Cs_2CO_3 / P3HT:PCBM / V_2O_5 / Al. The Ag particles are obtained by firstly spin coating a Ag colloid on the ITO/glass substrate and then annealed it at 120 °C for 12 min. All the other layers in this device are fabricated with the same processes as described in Section 6.2.

Using 20 nm Ag colloidal particles, three devices were made: (a) without Ag particles, (b) with dense Ag particles, for which the Ag colloid is spin-coated at 1500 rpm for 60 sec and (c) with sparse Ag particles, for which the Ag colloid is spin-coated at 3000 rpm for 60 sec. This batch of three devices showed a very interesting performance enhancement after they were kept under light illumination for a longer time, which is referred to as "light curing" later. The V_{OC}, J_{SC}, FF and PCE (η) are shown in Fig. 6.9, respectively.

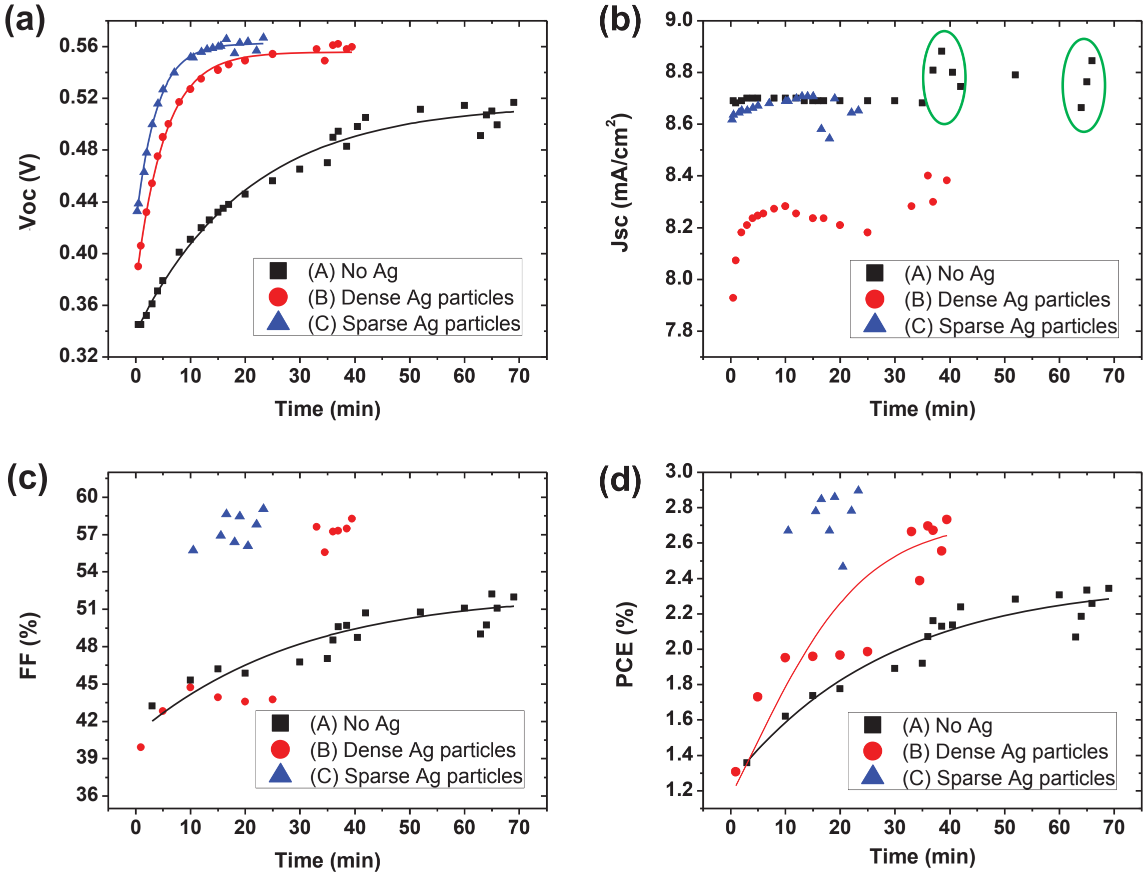

Fig. 6.9 The OPV characteristics of three devices with different concentration of Ag particles on the ITO/glass surface. The solid lines are used to guide the sight. The performance enhancement was seen after they samples were kept under light illumination. The Ag particles helped to speed up the performance enhancement process. Also, devices with Ag particles have higher final PCE.

Moreover, the Ag particles helped to speed up the performance enhancement. For device (A), the device stabilized after more than 60 min with a maximum PCE of 2.33%; device (B) stabilized after ~ 30 min of light illumination with a final PCE of 2.74%; device (C) stables after ~ 15 min with a final PCE of 2.90%. The most prominent characteristic that affects the PCE is the changes in V_{OC}, while changes in FF also plays an important role.

At the beginning of the measurement, all these devices exhibited poor performance. The free carrier generated from incident photons probably fell in the trap states in the P3HT:PCBM layer and help the bulk heterojunction to reach equilibrium. This could be the reason that the V_{OC} exhibits a stronger correlation with the illumination since the trap states at the P3HT and PCBM interfaces has strong influence on the V_{OC}. The faster light curing process for devices with Ag particles also suggests that Ag particles speed up the charge transfer processes for faster elimination of the trap sites. It is worth noticing that the relatively large variance for J_{SC} in the green oval regions in Fig. 6.9 (b) is because the plots in Fig. 6.9 contain information from six devices.

Even though the PCE of both device B and C are higher than that of device A, the dense Ag particles (device B, 1500 rpm, 60 sec spinning) lead to a decrease in J_{SC} possibly due to the shadowing effect of the Ag particles or stronger carrier recombination. With sparse Ag particles (device C, 3000 rpm, 60 sec spinning), both V_{OC} and FF are increased while J_{SC} is only slightly lowered. I confirmed with spectroscopic measurement that the sparse Ag particles do not affect the light transmission, as shown in Fig. 6.10 (a). Fig. 6.10 (b) compares the JV curves of device A and C after different light exposure time. It confirms that after 10 min, the JV curve of device C is similar to the stabilized one at 24 min. However, the JV curve for device A without Ag particles changes slower as suggested by the 20 min and 63 min curves. The EQE of stabilized device A and C are within +/- 5% difference for all the wavelengths between 400 ~ 800 nm and are not shown here. This is in agreement with the similar J_{SC} for the two devices.

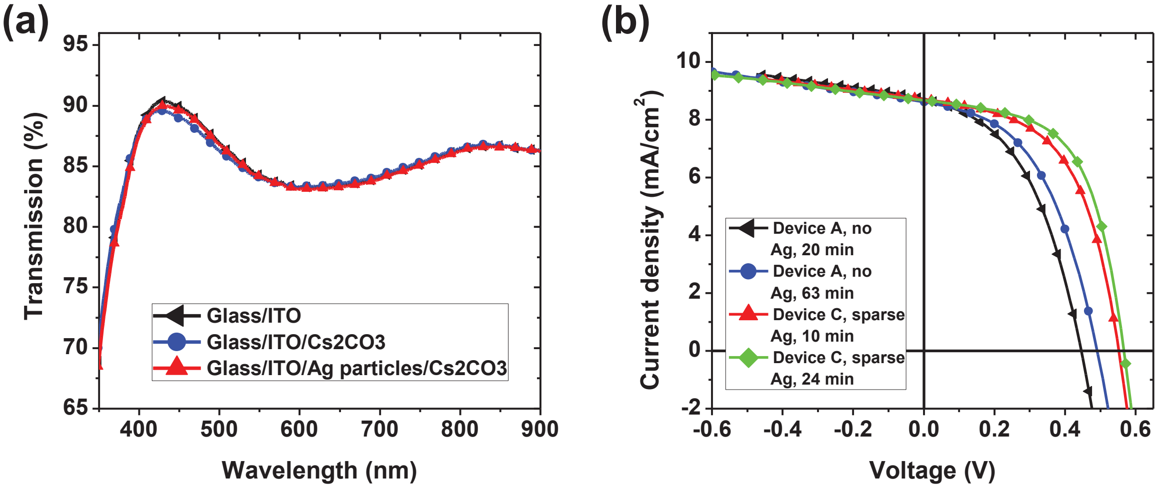

Fig. 6.10 (a) Transmission spectra measurement on ITO coated glass substrate showed that 3000 rpm, 60 sec spinning of colloidal Ag particles does not induce shadowing effect. (b) JV curves of device A (without Ag particles) and device C (with sparse Ag particles) under different times of light illumination. Device C showed fast "light curing" and higher final PCE.

Despite that the light curing phenomena has been repeated for four runs over two weeks, later devices do not have such significant characteristics change over light illumination time. As listed in Table 6.6, adding sparsely distributed Ag particle onto the ITO coated glass substarte does not help the V_{OC} or PCE (η). The changes in the working environment may be responsible.

Table 6.6 OPVs with a thick P3HT:PCBM layer, the effect of Ag particles on ITO coated glass

Ag particles	V_{OC} (V)	J_{SC} (mA/cm^2)	FF (%)	η (%)
w/o Ag	0.574	8.182	72.0	2.68
4500 rpm	0.581	8.555	71.1	2.60
3000 rpm	0.577	8.138	72.5	2.63
1500 rpm	0.577	6.391	94.8	1.86

However, the light curing effect suggests that Ag particles still have potential to improve solar cell efficiency, not necessarily through enhanced light absorption, as seen in Fig. 6.10 (b). It has been seen in the simulation that the SPPs have penetration depth of less than 150 nm, yet the P3HT:PCBM thickness is ~ 200 nm for all the devices so far. Decreased polymer thickness will make any plasmonic effect more significant. So several devices were made with 30 mg/mL P3HT:PCBM solution spin-coated at 700 rpm for 60 sec instead of 400 rpm. Their JV curves are shown in Fig. 6.11.

In Fig. 6.11, at strong reverse bias (-1.2 V), the current density for all four devices are the same (8.83 mA/cm^2). This means the photoactive layer is capable of absorbing and converting the same amount of photons into electrons. However, the different levels of J_{SC} indicate that the devices have different carrier collection efficiencies. The comparisons of the four devices are summarized in Table. 6.7.

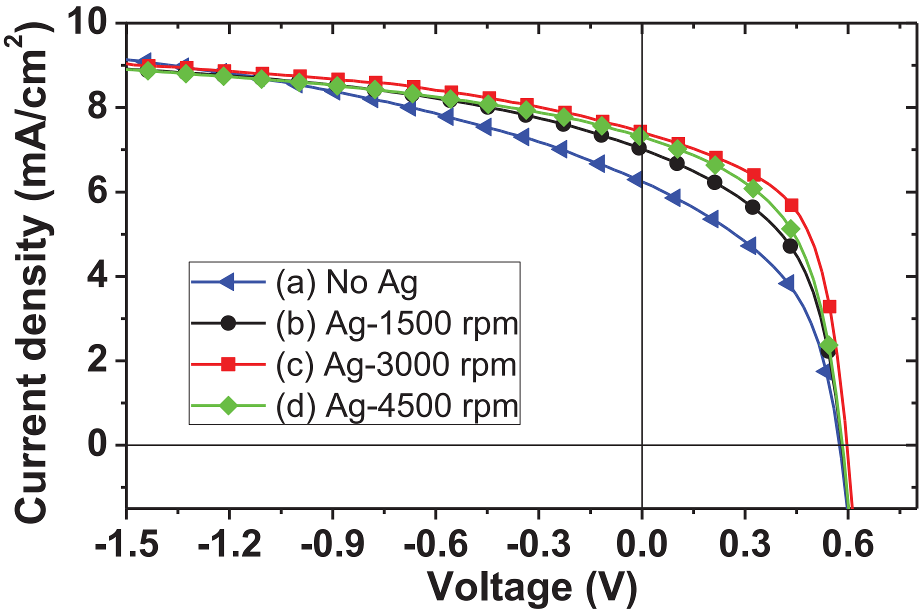

Fig. 6.11 With thinner P3HT:PCBM films, OPV with Ag particles on ITO showed higher carrier extraction. The comparable current density at strong reverse bias suggests the OPVs are capable of efficiently absorbing light. It is the carrier collection that limits the PCE.

Table 6.7 OPVs with a thin P3HT:PCBM layer, the effect of Ag particles on JV characteristics and carrier collection

Ag particles	V_{OC} (V)	J_{SC} (mA/cm^2)	FF (%)	η (%)	J_{SC} **ratio (%)**	
					0V/ -1.2V	V_m**/0V**
(a) w/o Ag	0.575	6.227	46.5	1.7	70.5	65.0
(b) 1500 rpm	0.583	6.991	51.3	2.1	79.2	67.5
(c) 3000 rpm	0.597	7.418	58.7	2.6	84.0	73.4
(d) 4500 rpm	0.583	7.300	53.3	2.3	82.7	70.3

With a thinner P3HT:PCBM film, the PCE is lower than that with a thicker active film. Yet, the low J_{SC} is not due to insufficient light absorption. The four devices have the same maximum current with the help of a reverse bias for better carrier collection, *i.e.* $J_{reverse\ bias} = 8.83\ mA/cm^2$at -1.2 V. This means the low J_{SC} and η is due to poor carrier extraction and collection. This is further confirmed by the ratio $J_{0V}/J_{-1.2V}$ in Table 6.7. At 0V, device (a) can extract 70.5% of all the electrons from the absorbed photons, while device (c) with Ag particles is capable of extracting 61.7%. The higher FF and J_{V_m}/J_{-0V} ratios confirm that devices with Ag particles have higher carrier extraction efficiency at positive bias as well. V_m and J_{V_m} correspond to the voltage and current density at which the PV output power is maximized.

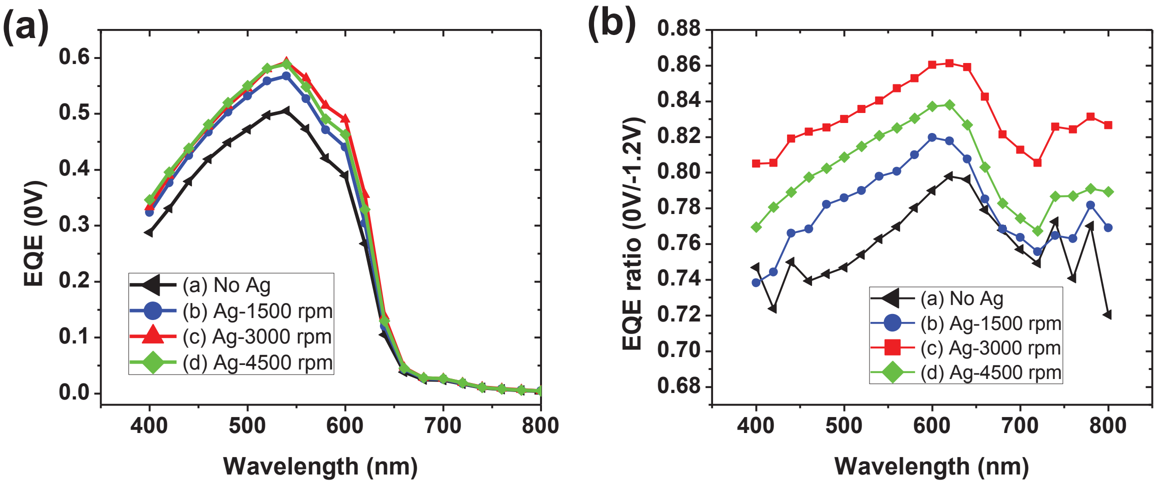

Fig. 6.12 (a) Devices in Table 6.7 showed higher EQE when Ag particles are added on the ITO/glass substrate. (b) The higher EQE ratios indicate better carrier extraction and collection efficiency in devices with Ag particles. All three devices with Ag particles have higher EQE ratios. Only device (c) has significantly higher EQE ratio for all the spectral span of 400 ~ 800 nm.

The EQE curves at 0V of the devices in Fig. 6.11 and Table 6.7 are plotted in Fig. 6.12 (a). The EQE was also measured at -1.2 V and the ratio $EQE_{0V}/EQE_{-1.2V}$ is plotted in Fig. 6.12 (b). QE ratio helps evaluating the wavelength-dependent carrier collection efficiency. Compared with device (a) without Ag particles, all the other three devices have higher QE ratio and thus higher carrier collection efficiency. Yet when there is too many (black line) or too few (green line) Ag particles, significantly higher QE ratio is only in the short wavelength range (< 650 nm). With the spin-coating speed of 3000 rpm for the Ag colloid, device (b) showed significantly higher QE ratio for all the wavelengths between 400 ~ 800 nm.

There are several possible reasons for the enhanced carrier collection efficiency.

(1) The strong local electromagnetic field that helps dissociation of the electron-hole pairs and transfer the free carrier as suggested by Wu *et al.* [15]. By using a much thinner Cs_2CO_3 as the buffer layer and a thinner P3HT:PCBM film, the plasmonic effect leads to a higher enhancement in the $J_{0V}/J_{-1.2V}$ ratio than devices with PEDOT:PSS as the buffer layer [15].

(2) The Ag particles causes changes in the morphology of Cs_2CO_3 as well as the P3HT:PCBM layers. The Cs_2CO_3 is ultra-thin and not a continuous film. Intuitively, it will be very sensitive to changes on the substrate. And the P3HT:PCBM morphology will respond differently to the changes in the Cs_2CO_3 layer as well.

To confirm possible morphology change in the Cs_2CO_3 and the P3HT:PCBM layers. SEM images were taken for (a) a Cs_2CO_3 layer, (b) a Cs_2CO_3 layer spin-coated on Ag particles, (c) P3HT:PCBM film on a Cs_2CO_3 layer and (d) the film of P3HT:PCBM /

Cs_2CO_3 / Ag particles. All these films are prepared on commercial ITO coated glass substrates and the images are shown in Fig. 6.13.

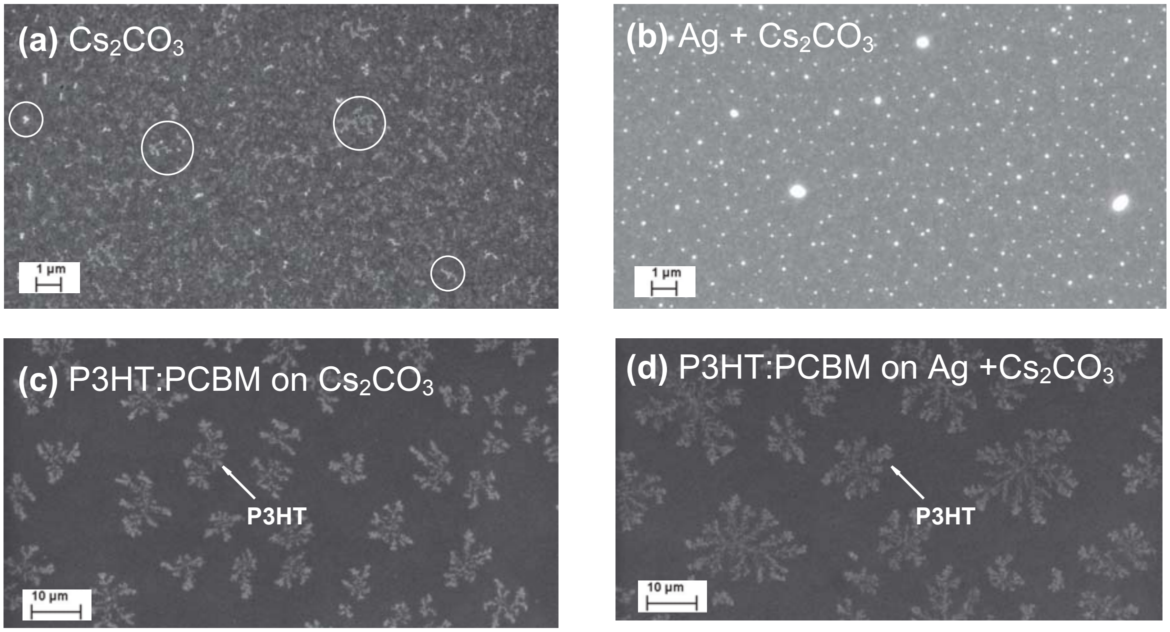

Fig. 6.13 SEM images of (a) a Cs_2CO_3 film, (b) a Cs_2CO_3 film on Ag particles, (c) P3HT:PCBM film with Cs_2CO_3 underneath and (d) P3HT:PCBM film with Cs_2CO_3 and Ag particles underneath. All these films are prepared on ITO coated glass.

In Fig. 6.13 (a), the Cs_2CO_3 is not quiet visible because it is not a continuous film and that ITO has large grains. For better visibility, the white circles mark a few spots of the randomly distributed Cs_2CO_3. However, when Cs_2CO_3 is spin-coated on Ag particles, the Cs_2CO_3 aggregates into dots, possibly around the Ag particles, as shown in Fig. 6.13 (b).

The P3HT:PCBM films under SEM clearly showed two different phases. Considering the structural differences between P3HT and PCBM, it is most probable that the white snowflake-shaped phase in Fig. 6.13 (c) and (d) is P3HT. The SEM images are the P3HT:PCBM near the anode (V_2O_5/Al) side. When there is more P3HT phase aggregating near the anode side, the carrier collection efficiency will be enhanced. This is in agreement with the JV and QE characteristics. Moreover, the snowflake-shaped P3HT-rich phases form longer chains, as shown in Fig. 6.13 (d), when there are Ag particles underneath the film. This may benefit the hole transport in P3HT as well.

In conclusion, introducing metallic particles into OPVs can be beneficial, even without light absorption enhancement. The strong localized electromagnetic fields and the changes in P3HT:PCBM morphology may have contributed to the improved carrier collection in the investigated inverted devices. Detailed analysis of both electrical and material tests will be helpful to further reveal plasmonics' potential in improving solar cell efficiency.

Chapter 7. Conclusions and future perspectives

In this thesis, the utilization of plasmonic gratings in OPVs has been demonstrated through both numerical simulations and experiments. Through numerical simulation, I found that with a grating with pitch near 1 μm and careful choice of the grating duty cycle, the OPV light absorption can be greatly enhanced for both TM and TE waves. Under TM-polarized light illumination, the grating will help exciting multiple SPP modes. The resulting strong local field enhancement and longer light path length lead to an increase in light absorption. Under TE-polarized light illumination, incident light will be diffracted and coupled to waveguide modes inside the OPV layers. As a result, light trapping independent of the incident light polarization can be achieved even though the grating is periodic in only one direction. The grating duty cycle turns out to be the most important parameter in achieving the optimization of the light absorption enhancement. When the grating pitch is kept between 950 nm and 1200 nm, high *EF* (enhancement factor in light absorption) bands are found for TM waves when the duty cycle is between 35% ~ 45%, and for TE waves when the duty cycle is between 43% ~ 53%. For unpolarized light, the absorption enhancement has two high *EF* regions, one at 36% which is the lower edge of the TM band and the other at 43% which is the overlap between the TM and TE band.

With the help of the EBL and micro-spectrometer systems, I was able to fabricate various gratings on the same substrate and fairly compare the effect of grating geometries on the light absorption enhancement. I showed that a higher grating offers stronger enhancement in light absorption for both TE and TM waves. Two samples were then made with gratings of different pitches and duty cycles. For the study of the effect grating duty cycle with the grating pitch fixed at 1040 nm, one sample showed optimum results when the duty cycle is 36%, while the other sample showed optimum results with a duty cycle of 45%. These results are in good agreement with predictions from the simulations. In addition, I found that the grain sizes of the Ag grating plays an important role in the light absorption enhancement. With larger grain sizes, which may act as small antennas, both the plasmonic absorption peaks under TM waves and the waveguide-mode-assisted peaks under TE waves are broadened. The broadening is beneficial for TM waves since similar increase in absorption can be achieved over a wider spectral range. However, broadened peaks under TE illumination have lower increase in absorption. It was showed experimentally that comparable light absorption increase was achieved for all polarization angles.

Both the commonly adapted superstrate type OPVs and the proposed substrate type OPVs were made for comparisons. The highest efficiencies are: 4.03% for superstrate type traditional OPVs, 3.11% for superstrate type inverted OPVs, and 1.11% for substrate type inverted OPVs, respectively. The structure of the 1.11% substrate type OPV is Glass / 100 nm Ag / 2 nm Cs_2CO_3 / ~ 180 nm P3HT:PCBM / 15 nm MoO_3 / 120 nm ITO. Despite the fact that the device is made on a planar Ag film, it has the same architecture as the proposed plasmonic OPV with Ag gratings on the back. While inconsistent PCEs and high device failure rate hindered further integration of Ag gratings and OPV structure, I coud show that that putting a 2 nm Al between the 15 nm MoO_3 and 120 nm ITO increases both the V_{OC} and J_{SC}, which may lead to better substrate type devices.

To improve the device repeatability, well-controlled experimental environment is needed. Another important issue is the Ag coated substrate, for which the control of grain sizes, surface morphology and surface cleaning all have great impact on the final solar cell performance.

Plasmonic nanoparticles, which support localized surface plasmon resonances, have also been investigated in the superstrate type inverted OPVs. Compared with tranditional OPVs, inverted devices have thinner buffer layer between the substrate and photoactive layer. This will allow the plasmonic effect to act directly on the photoactive layer. In addition, the thickness of the polymer layer is reduced to show the plasmonic effect better. Ag particles are added on ITO/glass in the structure of Glass / ITO / Cs_2CO_3 / P3HT:PCBM / V_2O_5 / Al. I found that the improved device performance from the addition of Ag particles is due to improvement in the carrier extraction, rather the increased light absorption. The higher carrier collection efficiency may due to the strong local electromagnetic field from L-SPRs or the morphology change of the P3HT:PCBM layer. This study opens up more opportunities of plasmonic effect in solar cell applications.

An important issue in plasmonic solar cells is the ease of fabrication. Cheap, fast and high throughput fabrication methods are needed for wide application of plasmonic nanostructure. In this sense, the approach based on nanoparticles is more attractive. The utilization of plamsonic nanoparticles, however, should not be restricted to Ag or Au nano spheres. As discussed in this thesis, the shape of plamonic particles plays a more important role in their optical characteristics than the sizes of nanoparticles. So the changes in the nanoparticles will offer more tunability in their spectral responses to suit different solar cell designs. It has more importance in tandem OPVs in which different junctions are designs for specific spectral ranges. With better understanding of plasmonic effect in solar cells and better design, plasmonics will be of great help in further advancing the OPV research. Easier and faster fabrication methods may be needed to realize wider application of plasmonic OPVs as clean and renewable energy source.

Appendix A. Simulation-predicted absorption increase in OPVs

In Chapter 3, only the absorption increase in the P3HT:PCBM photoactive layer is taken into consideration while defining the photocurrent enhancement factor (EF). However, the increase in absorption inside the P3HT:PCBM layer and the Ag grating cannot be separated in the reflection measurement in Chapter 5. I tried to estimate how much of the absorption increase in the whole OPV structure is actually inside the P3HT:PCBM layer with COMSOL multiphysics® simulations.

With TM-polarized incident light, Figure A.1 (a) shows the increase in absorption in the OPV with a Ag grating of 1040 nm pitch, 36% duty cycle and 55 nm height, compared with a OPV structure on a 100 nm flat Ag film. Clearly, there is significant increase in absorption that is inside the P3HT:PCBM polymer layer (black curve in Fig. A.1 (a)). Yet, the absorption increase in the whole OPV structure is much higher (red curve), since the SPPs propagate along the interface between the P3HT:PCBM and Ag grating, both of which are lossy materials with complex dielectric constants in the simulations. Considering that only the absorption inside the photoactive layer contributes to the photocurrent, the "effectiveness ratio" of the absorption enhancement is defined as the percentage of the absorption increase in the P3HT:PCBM layer out of the increase in the whole OPV structure. The effectiveness ratio for TM waves is plotted in Fig. A.1 (b).

For wavelengths shorter than 730 nm, more than 50% of the total increase absorption in the OPV device is inside the P3HT:PCBM layer. As the wavelength increases, due to the very low absorption of P3HT:PCBM at longer wavelengths, more of the absorption increase is inside the Ag grating.

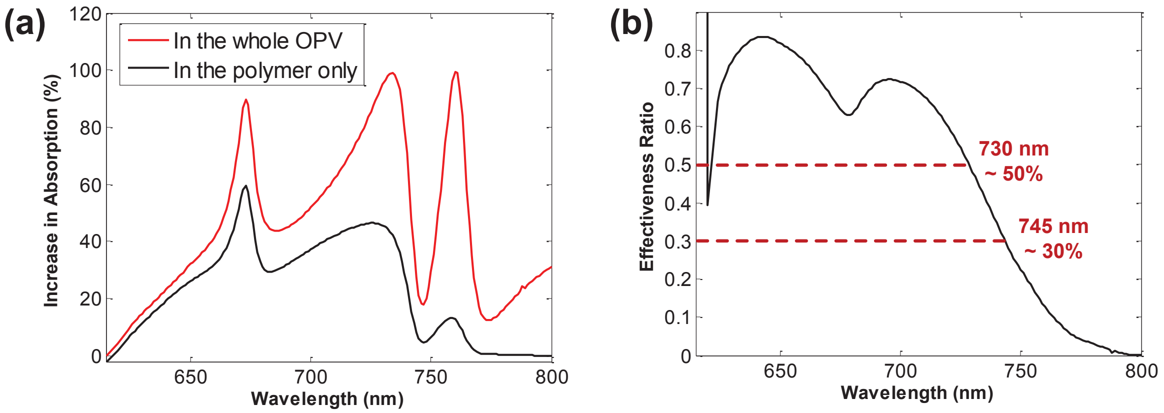

Fig. A.1 For TM waves (a) the absorption increase in the whole OPV structure and the P3HT:PCBM polymer film; (b) the effectiveness ratio of the increase in absorption, which is the ratio between the black and red curves in (a). The effectiveness ratio evaluates how much of the total absorption increase is actually inside the P3HT:PCBM layer.

Similarly, with TE-polarized incident light, the absorption increase in the whole OPV structure is higher than the increase in the P3HT:PCBM layer, as shown in Fig. A.2 (a). The grating has 850 nm pitch, 45% duty cycle and 55 nm height, which is the optimized design for TE waves.

The effectiveness ratio of the absorption increase for TE waves is shown in Fig. A.2 (b). For wavelengths shorter than 730 nm, 70% ~ 85% of the absorption increase is from the P3HT:PCBM layer. Beyond 730 nm, the absorption increase from the P3HT:PCBM layer drops, to ~ 50% at 740 nm and ~ 30% at 760 nm. The overall value of the effectiveness ratio for TE waves (Fig. A.2 (b)) is higher than that for TM waves (Fig. A.1 (b)). This is because the waveguide modes excited by TE incident waves are guided by the whole OPV structure with only a small portion of the mode energy in the Ag grating. In contrast, the SPPs excited by TM waves propagate along the P3HT:PCBM/Ag grating interface, which have larger portion of energy in the lossy Ag grating.

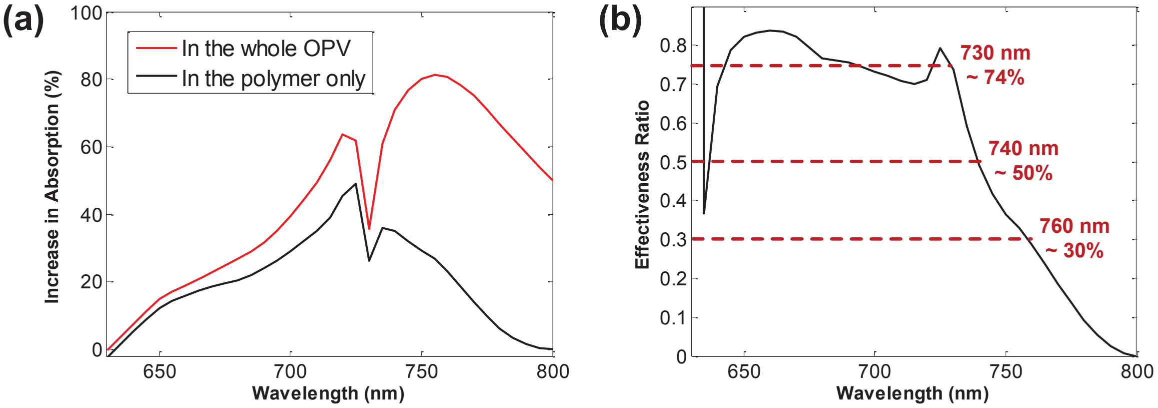

Fig. A.2 For TE waves (a) the absorption increase in the whole OPV structure and the P3HT:PCBM polymer film; (b) the effectiveness ratio of the increase in absorption, which evaluates how much of the total absorption increase is actually inside the P3HT:PCBM layer.

For both TE and TM waves, more of the absorption increase is inside the photoactive layer at short wavelengths. More importantly, these simulation results suggest that most of the increase in absorption evaluated from the reflection measurements happens inside the P3HT:PCBM layer which will contribute to the photocurrent.

Appendix B. Comparisons between OPVs with Al and Ag gratings

In this thesis, silver (Ag) gratings are used for enhancing the light absorption in OPVs. Silver is chosen instead of aluminum (Al), which is a commonly used electrode material in PVs, because Al supports stronger plasmonic resonances than Al [26].

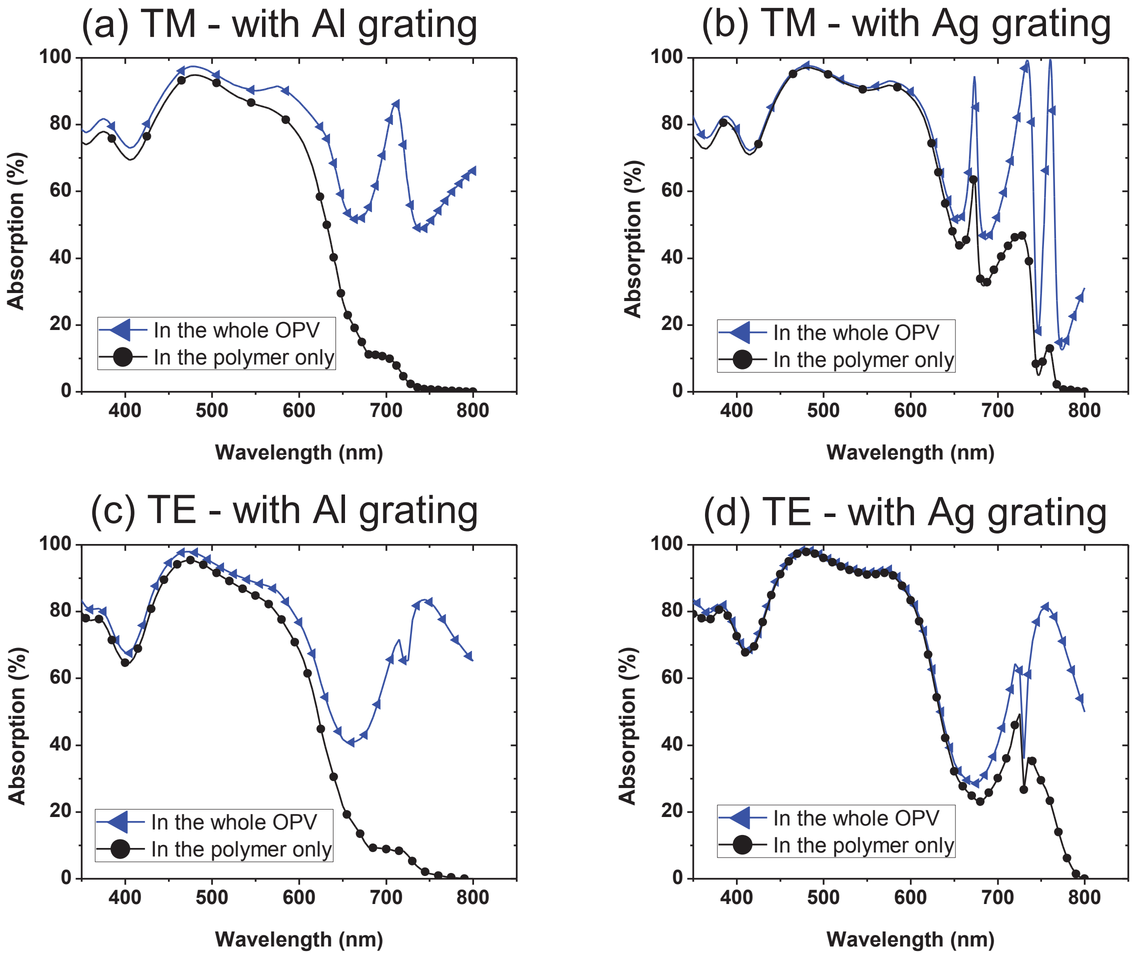

Fig. B.1 Absorption in the whole OPV structure and in the P3HT:PCBM film only for OPVs with Ag and Al gratings, respectively. With Al gratings, for both TM (a) and TE (c), the absorption spectra for OPV structures showed absorption peaks. However, the absorption increase is in the Al grating, rather than in the P3HT:PCBM film. With Ag gratings, the P3HT:PCBM absorption spectra have multiple peaks, indicating absorption enhancement in the photoactive layer.

Figure B.1 compared the absorption spectra in the whole OPV structure and in the P3HT:PCBM film only for OPVs with Ag and Al gratings, respectively. For TM waves, both Al and Ag gratings have 1040 nm pitch, 36% duty cycle and 55 nm height; for TE waves, both gratings have 850 nm pitch, 45% duty cycle and 55 nm height.

For OPVs with Ag gratings, as we discussed in Appendix A, there are significant absorption inside both the P3HT:PCBM and the Ag grating. But before 730 nm, most of the absorption enhancement is inside the P3HT:PCBM film. This is also confirmed in Fig. B.1 (b) and (d). However, when the Ag gratings are replaced with Al gratings of the same geometries, there is little increase in absorption in the P3HT:PCBM film even though there is successful SPP modes and waveguide modes excitation in the OPV structure, as suggested by Fig. B.1 (a) and (c). This is because aluminum is much lossier than silver. Even with further structural optimization of the Al gratings, energy loss inside the Al grating is inevitable. As a result, plasmonic materials with lower losses are more suitable for solar cell applications.

Bibliography

1. Solar electricity / edited by Tomas Markvart with Klaus Bogus ... [et al.] (Chichester ; New York : Wiley, Chichester ; New York, 1994).
2. E. P. I. A. (EPIA), "Global Market Outlook for Photovoltaics until 2015, http://www.epia.org/publications/photovoltaic-publications-global-market-outlook/global-market-outlook-for-photovoltaics-until-2015.html," (May 2010), Accessed Mar 16, 2012.
3. N. R. E. L. (NREL), "2010 Solar Technologies Market Report," (Novermber 2011).
4. A. Luque, and S. Hegedus, Handbook of photovoltaic science and engineering (Wiley, Hoboken, NJ, 2003).
5. H. A. Atwater, and A. Polman, "Plasmonics for improved photovoltaic devices," Nature Materials 9, 205-213 (2010).
6. V. E. Ferry, M. A. Verschuuren, H. Li, R. E. I. Schropp, H. A. Atwater, and A. Polman, "Improved red-response in thin film a-Si:H solar cells with soft-imprinted plasmonic back reflectors," Applied Physics Letters 95, 3 (2009).
7. O. Inganas, F. Zhang, K. Tvingstedt, L. M. Andersson, S. Hellstrom, and M. R. Andersson, "Polymer Photovoltaics with Alternating Copolymer/Fullerene Blends and Novel Device Architectures," Advanced Materials 22, E100-E116 (2010).
8. K. Tvingstedt, N. K. Persson, O. Inganas, A. Rahachou, and I. V. Zozoulenko, "Surface plasmon increase absorption in polymer photovoltaic cells," Applied Physics Letters 91 (2007).

9. N. C. Panoiu, and R. M. Osgood, "Enhanced optical absorption for photovoltaics via excitation of waveguide and plasmon-polariton modes," Optics Letters 32, 2825-2827 (2007).
10. H. Stiebig, N. Senoussaoui, T. Brammer, and J. Muller, "The application of grating couplers in thin-film silicon solar cells," Solar Energy Materials and Solar Cells 90, 3031-3040 (2006).
11. L. L. Yin, V. K. Vlasko-Vlasov, J. Pearson, J. M. Hiller, J. Hua, U. Welp, D. E. Brown, and C. W. Kimball, "Subwavelength focusing and guiding of surface plasmons," Nano Letters 5, 1399-1402 (2005).
12. W. L. Barnes, A. Dereux, and T. W. Ebbesen, "Surface plasmon subwavelength optics," Nature 424, 824-830 (2003).
13. M. Moskovits, "Surface-enhanced spectroscopy," Reviews of Modern Physics 57, 783-826 (1985).
14. K. Kneipp, H. Kneipp, I. Itzkan, R. R. Dasari, and M. S. Feld, "Surface-enhanced Raman scattering: A new tool for biomedical spectroscopy," Current Science 77, 915-924 (1999).
15. J.-L. Wu, F.-C. Chen, Y.-S. Hsiao, F.-C. Chien, P. Chen, C.-H. Kuo, M. H. Huang, and C.-S. Hsu, "Surface Plasmonic Effects of Metallic Nanoparticles on the Performance of Polymer Bulk Heterojunction Solar Cells," Acs Nano 5, 959-967 (2011).
16. F. C. Chen, J. L. Wu, C. L. Lee, Y. Hong, C. H. Kuo, and M. H. Huang, "Plasmonic-enhanced polymer photovoltaic devices incorporating solution-processable metal nanoparticles," Applied Physics Letters 95 (2009).

17. K. A. Diest, "Active Metal-Insulator-Metal Plasmonic Devices," in Materials Science (California Institute of Technology, Pasadena, California, 2010).
18. G. Mie, "Articles on the optical characteristics of turbid tubes, especially colloidal metal solutions," Annalen Der Physik 25, 377-445 (1908).
19. R. H. Ritchie, E. T. Arakawa, J. J. Cowan, and R. N. Hamm, "Surface-plasmon resonance effect in grating diffraction," Physical Review Letters 21, 1530-& (1968).
20. A. Otto, "Excitation of nonradiative surface plasma waves in silver by method of frustrated total reflection," Zeitschrift Fur Physik 216, 398-& (1968).
21. Kretschmann.E, and H. Raether, "Radiative decay of non radiative surface plasmons excited by light," Zeitschrift Fur Naturforschung Part a-Astrophysik Physik Und Physikalische Chemie A 23, 2135-& (1968).
22. C. Sonnichsen, "Plasmons in metal nanostructures," in Physics Department (Ludwig-Maximilians-University, Munich, Germany, 2001).
23. W. A. Murray, and W. L. Barnes, "Plasmonic materials," Advanced Materials 19, 3771-3782 (2007).
24. J. Homola, "Surface plasmon resonance sensors for detection of chemical and biological species," Chemical Reviews 108, 462-493 (2008).
25. N. C. Lindquist, W. A. Luhman, S. H. Oh, and R. J. Holmes, "Plasmonic nanocavity arrays for enhanced efficiency in organic photovoltaic cells," Applied Physics Letters 93 (2008).
26. J. R. Sambles, G. W. Bradbery, and F. Z. Yang, "Optical-excitation of surface-plasmons - an introduction," Contemporary Physics 32, 173-183 (1991).

27. P. B. Johnson, and R. W. Christy, "Optical-constants of noble-metals," Physical Review B 6, 4370-4379 (1972).

28. S. Eustis, and M. A. El-Sayed, "Why gold nanoparticles are more precious than pretty gold: Noble metal surface plasmon resonance and its enhancement of the radiative and nonradiative properties of nanocrystals of different shapes," Chemical Society Reviews 35, 209-217 (2006).

29. J. A. Dionne, L. A. Sweatlock, H. A. Atwater, and A. Polman, "Planar metal plasmon waveguides: frequency-dependent dispersion, propagation, localization, and loss beyond the free electron model," Physical Review B 72 (2005).

30. H. T. Miyazaki, and Y. Kurokawa, "Squeezing visible light waves into a 3-nm-thick and 55-nm-long plasmon cavity," Physical Review Letters 96 (2006).

31. NREL, "Reference solar spectral irradiance: air mass 1.5. http://rredc.nrel.gov/solar/spectra/am1.5/."

32. NREL, "Best research-cell efficiencies. http://www.nrel.gov/ncpv/," (Feb 2012).

33. T. Kietzke, "Recent advanced in organic solar cells," Advances in OptoElectronics 2007, 15 (2007).

34. C. W. Tang, and A. C. Albrecht, "Chlorophyll-a photovoltaic cells," Nature 254, 507-509 (1975).

35. C. W. Tang, "2-layer organic photovoltaic cell," Applied Physics Letters 48, 183-185 (1986).

36. N. S. Sariciftci, L. Smilowitz, A. J. Heeger, and F. Wudl, "Photoinduced electron-transfer from a conducting polymer to buckminsterfullerene," Science 258, 1474-1476 (1992).

37. N. S. Sariciftci, D. Braun, C. Zhang, V. I. Srdanov, A. J. Heeger, G. Stucky, and F. Wudl, "Semiconducting polymer-buckminsterfullerene heterojunctions - diodes, photodiodes, and photovoltaic cells," Applied Physics Letters 62, 585-587 (1993).
38. S. E. Shaheen, C. J. Brabec, N. S. Sariciftci, F. Padinger, T. Fromherz, and J. C. Hummelen, "2.5% efficient organic plastic solar cells," Applied Physics Letters 78, 841-843 (2001).
39. G. Yu, J. Gao, J. C. Hummelen, F. Wudl, and A. J. Heeger, "Polymer photovoltaic cells - enhanced efficiencies via a network of internal donor-acceptor heterojunctions," Science 270, 1789-1791 (1995).
40. G. Yu, and A. J. Heeger, "Charge separation and photovoltaic conversion in polymer composites with internal donor-acceptor heterojunctions," Journal of Applied Physics 78, 4510-4515 (1995).
41. L. Dou, J. You, J. Yang, C.-C. Chen, Y. He, S. Murase, T. Moriarty, K. Emery, G. Li, and Y. Yang, "Tandem polymer solar cells featuring a spectrally matched low-bandgap polymer," Nat Photon 6, 180-185 (2012).
42. G. Li, R. Zhu, and Y. Yang, "Polymer solar cells," Nat Photon 6, 153-161 (2012).
43. J. G. Xue, S. Uchida, B. P. Rand, and S. R. Forrest, "4.2% efficient organic photovoltaic cells with low series resistances," Applied Physics Letters 84, 3013-3015 (2004).
44. Y. Sun, G. C. Welch, W. L. Leong, C. J. Takacs, G. C. Bazan, and A. J. Heeger, "Solution-processed small-molecule solar cells with 6.7% efficiency," Nat Mater 11, 44-48 (2012).

45. G. Li, C. W. Chu, V. Shrotriya, J. Huang, and Y. Yang, "Efficient inverted polymer solar cells," Applied Physics Letters 88, 3 (2006).
46. J. William J. Potscavage, "Physics and engineering of organic solar cells," in Electrical Engineering(Georgia Institute of Technology, Atlanta, GA, USA, 2011), p. 157.
47. H. Hoppe, and N. S. Sariciftci, "Organic solar cells: An overview," Journal of Materials Research 19, 1924-1945 (2004).
48. G. Chidichimo, and L. Filippelli, "Organic Solar Cells: Problems and Perspectives," International Journal of Photoenergy (2010).
49. S. S. van Bavel, E. Sourty, G. de With, and J. Loos, "Three-Dimensional Nanoscale Organization of Bulk Heterojunction Polymer Solar Cells," Nano Letters 9, 507-513 (2009).
50. G. Li, V. Shrotriya, J. S. Huang, Y. Yao, T. Moriarty, K. Emery, and Y. Yang, "High-efficiency solution processable polymer photovoltaic cells by self-organization of polymer blends," Nature Materials 4, 864-868 (2005).
51. M. Reyes-Reyes, K. Kim, and D. L. Carroll, "High-efficiency photovoltaic devices based on annealed poly(3-hexylthiophene) and 1-(3-methoxycarbonyl)-propyl-1-phenyl-(6,6)C-61 blends," Applied Physics Letters 87 (2005).
52. W. L. Ma, C. Y. Yang, X. Gong, K. Lee, and A. J. Heeger, "Thermally stable, efficient polymer solar cells with nanoscale control of the interpenetrating network morphology," Advanced Functional Materials 15, 1617-1622 (2005).
53. "Introduction to organic electronic and optoelectronic materials and devices. (Brief article) (Book review)," SciTech Book News.

54. X. Yang, and J. Loos, "Toward high-performance polymer solar cells: The importance of morphology control," Macromolecules 40, 1353-1362 (2007).
55. W. L. Bai, Q. Q. Gan, F. Bartoli, J. Zhang, L. K. Cai, Y. D. Huang, and G. F. Song, "Design of plasmonic back structures for efficiency enhancement of thin-film amorphous Si solar cells," Optics Letters 34, 3725-3727 (2009).
56. S. Pillai, K. R. Catchpole, T. Trupke, and M. A. Green, "Surface plasmon enhanced silicon solar cells," Journal of Applied Physics 101, 8 (2007).
57. D. Derkacs, S. H. Lim, P. Matheu, W. Mar, and E. T. Yu, "Improved performance of amorphous silicon solar cells via scattering from surface plasmon polaritons in nearby metallic nanoparticles," Applied Physics Letters 89, 3 (2006).
58. A. J. Morfa, K. L. Rowlen, T. H. Reilly, M. J. Romero, and J. van de Lagemaat, "Plasmon-enhanced solar energy conversion in organic bulk heterojunction photovoltaics," Applied Physics Letters 92, 3 (2008).
59. C. Rockstuhl, S. Fahr, and F. Lederer, "Absorption enhancement in solar cells by localized plasmon polaritons," Journal of Applied Physics 104 (2008).
60. O. El Daif, E. Drouard, G. Gomard, A. Kaminski, A. Fave, M. Lemiti, S. Ahn, S. Kim, P. R. I. Cabarrocas, H. Jeon, and C. Seassal, "Absorbing one-dimensional planar photonic crystal for amorphous silicon solar cell," Optics Express 18, A293-A299 (2010).
61. R. Dewan, and D. Knipp, "Light trapping in thin-film silicon solar cells with integrated diffraction grating," Journal of Applied Physics 106 (2009).

62. R. A. Pala, J. White, E. Barnard, J. Liu, and M. L. Brongersma, "Design of Plasmonic Thin-Film Solar Cells with Broadband Absorption Enhancements," Advanced Materials 21, 3504-+ (2009).

63. B. Curtin, R. Biswas, and V. Dalal, "Photonic crystal based back reflectors for light management and enhanced absorption in amorphous silicon solar cells," Applied Physics Letters 95, 3 (2009).

64. W. Wang, S. M. Wu, K. Reinhardt, Y. L. Lu, and S. C. Chen, "Broadband Light Absorption Enhancement in Thin-Film Silicon Solar Cells," Nano Letters 10, 2012-2018 (2010).

65. F. J. Haug, T. Soderstrom, O. Cubero, V. Terrazzoni-Daudrix, and C. Ballif, "Plasmonic absorption in textured silver back reflectors of thin film solar cells," Journal of Applied Physics 104 (2008).

66. W. E. I. Sha, W. C. H. Choy, and W. C. Chew, "A comprehensive study for the plasmonic thin-film solar cell with periodic structure," Optics Express 18, 5993-6007 (2010).

67. J. S. Huang, Z. Xu, and Y. Yang, "Low-work-function surface formed by solution-processed and thermally deposited nanoscale layers of cesium carbonate," Advanced Functional Materials 17, 1966-1973 (2007).

68. L. M. Chen, Z. R. Hong, G. Li, and Y. Yang, "Recent Progress in Polymer Solar Cells: Manipulation of Polymer: Fullerene Morphology and the Formation of Efficient Inverted Polymer Solar Cells," Advanced Materials 21, 1434-1449 (2009).

69. F. C. Chen, J. L. Wu, C. L. Lee, W. C. Huang, H. M. P. Chen, and W. C. Chen, "Flexible Polymer Photovoltaic Devices Prepared With Inverted Structures on Metal Foils," Ieee Electron Device Letters 30, 727-729 (2009).
70. A. J. Moule, and K. Meerholz, "Interference method for the determination of the complex refractive index of thin polymer layers," Applied Physics Letters 91 (2007).
71. M. R. Tubbs, "MoO_3 layers - optical-properties, color-centers, and holographic recording," Physica Status Solidi a-Applied Research 21, 253-260 (1974).
72. "http://refractiveindex.info/," http://refractiveindex.info/.
73. R. Kroon, M. Lenes, J. C. Hummelen, P. W. M. Blom, and B. De Boer, "Small bandgap polymers for organic solar cells (polymer material development in the last 5 years)," Polymer Reviews 48, 531-582 (2008).
74. J. Dorfmuller, R. Vogelgesang, R. T. Weitz, C. Rockstuhl, C. Etrich, T. Pertsch, F. Lederer, and K. Kern, "Fabry-Perot Resonances in One-Dimensional Plasmonic Nanostructures," Nano Letters 9, 2372-2377 (2009).
75. G. Della Valle, T. Sondergaard, and S. I. Bozhevolnyi, "Plasmon-polariton nano-strip resonators: from visible to infra-red," Optics Express 16, 6867-6876 (2008).
76. P. Zilio, D. Sammito, G. Zacco, and F. Romanato, "Absorption profile modulation by means of 1D digital plasmonic gratings," Optics Express 18, 19558-19565 (2010).
77. Y. C. Lee, C. F. Huang, J. Y. Chang, and M. L. Wu, "Enhanced light trapping based on guided mode resonance effect for thin-film silicon solar cells with two filling-factor gratings," Optics Express 16, 7969-7975 (2008).

78. A. Naqavi, K. Soederstroem, F.-J. Haug, V. Paeder, T. Scharf, H. P. Herzig, and C. Ballif, "Understanding of photocurrent enhancement in real thin film solar cells: towards optimal one-dimensional gratings," Optics Express 19, 128-140 (2011).

79. S. S. Wang, and R. Magnusson, "Theory and applications of guided-mode resonance filters," Applied Optics 32, 2606-2613 (1993).

80. D. Rosenblatt, A. Sharon, and A. A. Friesem, "Resonant grating waveguide structures," Ieee Journal of Quantum Electronics 33, 2038-2059 (1997).

81. C. Y. Wei, S. J. Liu, D. G. Deng, J. Shen, J. D. Shao, and Z. X. Fan, "Electric field enhancement in guided-mode resonance filters," Optics Letters 31, 1223-1225 (2006).

82. Microfluidics and microfabrication / Suman Chakraborty, editor (New York : Springer, New York, 2010).

83. M. Huff, "MEMS fabrication," Sensor Review 22, 16 (2002).

84. G. Xu, M. Tazawa, P. Jin, and S. Nakao, "Surface plasmon resonance of sputtered Ag films: substrate and mass thickness dependence," Applied Physics a-Materials Science & Processing 80, 1535-1540 (2005).

85. M. D. Malinsky, K. L. Kelly, G. C. Schatz, and R. P. Van Duyne, "Nanosphere lithography: Effect of substrate on the localized surface plasmon resonance spectrum of silver nanoparticles," Journal of Physical Chemistry B 105, 2343-2350 (2001).

86. M. Adamik, P. B. Barna, and I. Tomov, "Correlation between texture and average grain size in polycrystalline Ag thin films," Thin Solid Films 359, 33-38 (2000).

87. A. J. Pearson, T. Wang, R. A. L. Jones, D. G. Lidzey, P. A. Staniec, P. E. Hopkinson, and A. M. Donald, "Rationalizing Phase Transitions with Thermal Annealing

Temperatures for P3HT:PCBM Organic Photovoltaic Devices," Macromolecules 45, 1499-1508 (2012).

88. J.-S. Huang, C.-Y. Chou, M.-Y. Liu, K.-H. Tsai, W.-H. Lin, and C.-F. Lin, "Solution-processed vanadium oxide as an anode interlayer for inverted polymer solar cells hybridized with ZnO nanorods," Organic Electronics 10, 1060-1065 (2009).